Magnetization manipulation induced by spin current and ultrafast laser

Jiaqi Wei

To cite this version:

Jiaqi Wei. Magnetization manipulation induced by spin current and ultrafast laser. Physics [physics]. Université de Lorraine; Beihang university (Pékin), 2021. English. NNT : 2021LORR0121 . tel-03378777

HAL Id: tel-03378777
https://hal.univ-lorraine.fr/tel-03378777v1

Submitted on 14 Oct 2021

C2MP

Institute Jean Lamour

Beihang University

Thèse

Présentée et soutenue publiquement pour l’obtention du titre de

DOCTEUR DE l’UNIVERSITE DE LORRAINE

Mention : .Physique

par Jiaqi WEI

Sous la direction de Stéphane MANGIN (FRANCE)

Weisheng ZHAO (CHINE)

Manipulation de l’aimantation par un courant de spin et par pulse laser ultra-rapid

15/06/2021

Membres du jury :

Directeur(s) de thèse :	**Stéphane MANGIN**	**Professeur, Université de Lorraine, Nancy, FRANCE**
	Weisheng ZHAO	**Professeur, Beihang University, Beijing, CHINE**
CoDirecteur(s) de thèse :	**Francois MONTAIGNE**	**Professeur, Université de Lorraine, Nancy, FRANCE**
Président de jury :	**Bert KOOPMAN**	**Professeur, Eindhoven University of Technology, Eindhoven, PAS-BAS**
Rapporteurs :	**Liliana BUDA-PREJBEANU**	**Professeure, Spintec, Grenoble, FRANCE**
	Weiwei LIN	**Professeur, Southeast University, Nanjing, CHINE**
Examinateurs :	**Na LEI**	**Professeure, Beihang University, Beijing, CHINE**
	Bert KOOPMAN	**Professeur, Eindhoven University of Technology, Eindhoven, PAS-BAS**

Magnetization manipulation induced by spin current and ultrafast laser

Author:

Jiaqi Wei

Weisheng ZHAO Professor, Beihang University, Director

Stéphane MANGIN Professor, University of Lorraine, Director

François MONTAIGNE Professor, University of Lorraine, Co-Director

ACKNOWLEDGMENT

First and foremost, it has been a great honor and privilege to do my PhD research under the supervision of Weisheng Zhao, Stéphane Mangin, and Francois Montaigne. They give me the opportunity to work on a meaningful project in both Beihang University and University of Lorraine, two of the world’s leading research groups in ultrafast spintronics.

I am thankful to Michel Hehn who is in charge of the magneto-sputtering machine. All my samples for the research in AOS were prepared by him, which takes a lot of time.

It is my pleasure to thank Dr. Boyu and Dr. Yassine for supporting me from the very beginning. For scientific research, the first step is always the hardest. With their help, I quickly obtained the fundamental skills that are needed in research of ultrafast magnetization dynamics

I would also like to thank Dr. Bin and Prof. Zhongmin, from Suzhou Institue of Nano-Tech and Nano-Bionics (SINANO), Chinese Academy of Sciences. They were responsible for the design and the fabrication of spin transfer torque nano-oscillators. In particular, I gratefully appreciate Bin for performing together the measurements. He is really hard working and never gives up before getting satisfying results. I have been lucky to collaborate with him and sharing experiences during my stay in SINANO.

I am pleased to express my appreciation to Thibaud Fache and Thai Ha Pham for the usual prompt help and for creating a welcoming atmosphere in the IJL office. I am also grateful to George. Kichin, for providing helpful advices on the measurement of AOS.

Over these years, I have benefitted from the knowledge and expertise of friendly cleanroom staff. I am grateful to Dr. Carlos Rojas-Sanchez, cleanroom manager, for accommodating our needs. In addition, I appreciate Laurent Badie, Gwladys

Lengaigne as well as Stefan MC Murtry, for training me to use different equipment in MINALOR.

I have been lucky to have some of the nicest people as my lab mates and friends. In particular, Zhiqiang Cao, thanks for inspiring me with your thoughts, creativity and talents. Moreover, we also have common interests, the basketball, which give me a good relax outside of work.

I would like to appreciate my colleagues in IJ. Jean-Loïs Bello and Quentin Remy, thank you for your precious friendship. It was always delightful to see your faces in the office in IJL. Daniel Lacour, thanks for being a caring, thoughtful and calm support. Wei Zhang, I appreciate your work on the magnetic simulations, even after I moved back to my country. Gregory Malinowski and Jon Gorchon, I appreciate your time and patience in teaching me precise optical alignment. I am also, grateful to Yong Xu for his help in daily life, like paperwork conerning bank account, renting house and insurance. In addition, I am grateful to Xiaofei Fan, Anni Cao, and Daoqian Zhu, who give me a lot of help from Beihang University.

I also want to thank my girlfriend Runan HUAN for being with me in Nancy. After obtaining her master's degree in English from Beihang University, she came to ICN Business School for further study. She was involved in every paper I published, helping check my paper carefully on English writing and giving suggestions on modifications accordingly. Apart from this, we visited many countries in Europe together on holidays, and took a lot of extraordinary photos, which released my pressure a lot from daily intense work. During our stay in Nancy, we also encountered many difficulties in life, while we supported each other and overcame them eventually. With her company and support, I was able to concentrate on my Ph.D. research missions better.

Many thanks to China Scholarship Council (CSC) for its funding support during my stay in France.

I would not be able to reach my goals without the constant encouragement and support of my parents, Biao Wei and Zhenmei Li. I cannot appreciate them enough for their love and devotion. Thank you for always believing in me and supporting my decisions.

Jiaqi Wei

11 April 2021, Beijing

Abstract

Magnetization manipulation is one of the most actively researched topics in the field of spintronics. Different ways of manipulation can trigger magnetization dynamics on different time scales. Among these dynamics, magnetization precession and ultrafast demagnetization have attracted substantial interests. The frequency of magnetization precession is normally in the GHz range corresponding to a period of hundreds of ps, which is the basic mechanism of spin torque nano-oscillators (STNO), a new type of microwave devices which show advantages over conventional voltage-controlled oscillator (VCO) in terms of size, energy consumption and tunable frequency. Ultrafast demagnetization was first observed in Ni which takes places in hundreds of femtoseconds. Triggered by this, All-Optical Switching (AOS) was then demonstrated which is much faster than any torque induced switching, promising for application in the high-speed magnetic memory.

Although many studies on these two phenomena have been reported, several issues need to be addressed before they move toward application. STNOs are supposed to be used for amplitude shift keying (ASK) or frequency shift keying (FSK), but the optimal conditions for these two types of microwave modulation are still not well explored. As for AOS, the influence of the laser parameters such as fluence and pulse duration and the material properties such as the composition and the thickness has not been systematically investigated.

In this thesis, these two types of magnetization manipulation are studied in detail. Concerning magnetization precession, we demonstrate that a stronger magnetic field allows a wider frequency tuning range while a smaller magnetic field results in a wider amplitude tuning range. Thus, these two scenarios are applicable to FSK and ASK, respectively, providing guidelines for STNO in microwave modulation. In the second study, we demonstrate that AOS depends strongly on pulse characteristic. This was shown by building a magnetization state diagram for GdFeCo and Co/Pt which are two typical materials showing All-Optical Helicity-Independent Switching

(AO-HIS) and All-Optical Helicity-Dependent Switching (AO-HDS), respectively. These results allow a better understanding of the fundamental mechanism behind laser-induced magnetization dynamics.

Résumé

La manipulation de l'aimantation est un des sujets de recherche les plus étudiés dans le domaine de l'électronique de spin. Différentes méthodes de manipulations peuvent exciter les propriétés dynamiques de l'aimantation à différentes échelles de temps. Parmi les phénomènes dynamiques, la précession de l'aimantation et la désaimantation ultrarapide ont suscité un intérêt particulier. La fréquence de précession de l'aimantation est de l'ordre du GHz et correspond à une période de centaines de picosecondes. Cette précession est le mécanisme à l'œuvre dans les nano-oscillateurs à transfert de spin (NOTS), un nouveau type de dispositif microonde présentant des avantages sur le oscillateur commandé en tension (OCT) conventionnel en terme de taille, de consommation d'énergie et d'adaptabilité de la fréquence. La désaimantation ultrarapide a été observé pour la première fois dans du nickel en quelques centaines de femtosecondes. Le renversement tout optique (RTO), nécessitant la désaimantation ultrarapide, a ensuite été démontré expérimentalement. Le RTO est bien plus rapide que tout autre retournement de l'aimantation par couple et est donc prometteur pour construire des mémoires magnétiques ultrarapides.

Bien que de nombreuses études sur ces deux phénomènes existent, plusieurs problèmes se doivent d'être résolus avant de pouvoir passer à l'étape de production industrielle. Les NOTS sont censés être utilisés pour la modulation par déplacement d'amplitude (MDA) ou la modulation par déplacement de fréquence (MDF), mais les conditions optimales pour ces deux types de modulation microondes n'ont pas encore été assez investiguées. Quant au RTO, l'influence des paramètres du laser tels que la fluence ou la durée de l'impulsion et des propriétés du matériau tels que le composition et l'épaisseur n'a pas fait l'objet d'études systématique.

Dans ce manuscrit, ces deux types de manipulation de l'aimantation sont étudiés en détail. En ce qui concerne la précession de l'aimantation, nous démontrons qu'un champ magnétique accru permet d'obtenir une plus large plage de fréquence possible alors qu'un champ magnétique plus faible résulte en une plage d'amplitude possible

élargie. Ainsi ces deux scenario sont applicables au MDF et MDA, respectivement, et posent les bases d'une utilisation des NOTS en modulation microonde. Dans la deuxième étude, nous démontrons que le RTO dépends fortement des caractéristiques de l'impulsion laser. Pour cela nous avons construit un diagramme d'état pour le GdFeCo et le Co/Pt, deux matériaux typiques respectivement du retournement tout optique indépendant de l'hélicité (RTO-IH) et du retournement tout optique dépendant de l'hélicité (RTO-DH). Ces résultats permettent une meilleur compréhension du mécanisme fondamental régissant la dynamique de l'aimantation induite par exposition à un laser.

General Introduction

Wireless Sensor Networks (WSNs) are main building blocks of the IoT which have drawn much attention in the industry and research community. WSNs are interconnected sensor nodes that communicate wirelessly to collect data about the surrounding environment [1-3]. Even though significant advances have been made recent years, two major problems need to be addressed with the extensive use of WSNs.

First, the number of connected IoT devices is forecasted to grow to 41.6 billion by 2025, which will generate 79.4 zettabytes (ZB) of data [4]. Thus a high-speed storage method is in urgent demand. Second, in many cases, a large number of sensor nodes are required in WSNs. The information transmission between these nodes is implemented by wireless communication. As a consequence, the communication module usually accounts for most of the power consumption of the entire system. Now it is pressing to develop new types of microwave devices with smaller size and lower power consumption.

Spintronics is expected to tackle the above problems. The main purpose of magnetization manipulation is to stimulate different magnetization dynamics, such as demagnetization, precession or switching. Steady magnetization precession can be achieved using spin current through Spin Transfer Torque and Spin Orbit Torque. The frequency of precession is normally in the GHz range (corresponding to a period of hundreds of ps), which has been shown to induce microwave generation in magnetic tunnel junction or spin valves, namely spin transfer torque nano-oscillators (STNOs). STNOs are prospective successors of transistor-based emitters and receivers of radio-frequency signals. In comparison to the conventional electronic oscillators, STNOs offer the advantage of being tunable over a wide range of frequencies, the smaller lateral size (up to 50 times) and the lower power consumption [5-7].

Magnetization switching is already used for memory devices. In hard disk drive

(HDD), the main device for mass data storage nowadays, the digital information is stored by setting the magnetization of storage medium either “up” or “down”. In order to increase the storage density, the volume of each bit has to shrink. As a consequence, materials with high perpendicular magnetic anisotropy K_u have to be found as storage medium so as to maintain their thermal stability. Therefore those materials exhibit high switching filed. On the other hand, the maximum achievable recording field generated by the hard disk head is around 1 Tesla limited by the size of main pole tip. Consequently, this writing method reaches a limit. In this context, Stanciu *et al.*’s discovery in 2007 showing that a single femtosecond laser pulse can fully reverse the magnetization of a GdFeCo thin film, has a great potential application [8]. This phenomenon namely all-optical switching (AOS) not only removes the need for applied magnetic field but also drives writing time towards the picosecond timescale.

Despite intensive research, the real applications of STNOs and AOS have a long way to go. In conventional wireless communication system, STNOs are expected to be used as a local oscillator to generate carrier signal which is then mixed with another RF signal by using an RF mixer to obtain the intermodulation signal. However, the power of STNOs is too weak to drive the RF mixer. Recently, U. Ebels’s group in Spintec proposed to implement the frequency shift keying (FSK) in STNOs by digital modulation of the current [9], which do not require an RF mixer. Their work shows the feasibility of using STNOs in wireless communication while the optimal conditions for STNOs to be used in FSK scheme are still not clear. There are also some issues needed to be addressed in AOS. To date, two different types of AOS have been identified. The first one is all-optical helicity-independent switching (AO-HIS) in which case one single laser pulse is sufficient to reverse the magnetization. AO-HIS occurs for a very limited number of materials such as Gd-based ferrimagnetic materials [10-12]. The second type is all-optical helicity-dependent switching (AO-HDS) which requires multiple pulses to achieve complete magnetization reversal. However AO-HDS is commonly observed in various types of magnetic materials (Ferrimagnets, ferromagnets, alloys, multilayers, epitaxial, amorphous) [13-15]. For AO-HIS, it has been demonstrated that the switching fluence window rapidly decreases with the increase of the pulse duration. Thus a femtosecond laser pulse is preferred to excite AO-HIS. However, the semiconductor laser sources so far are only capable to generate laser pulses with picosecond temporal width where the switching window is very narrow or even vanishes. For AO-HDS, the magnetization reversal is generally considered to be achieved via domain nucleation and propagation, which is a cumulative process. Thus hundreds of laser pulses are required in this case, which hinders its practical application.

In this thesis, I will first present the magnetization dynamics in planar and perpendicular STNOs under different currents and magnetic fields using spectrum analyzer, in order to find the optimal conditions for microwave generation. Based on these results, I propose a new modulation approach, memristor-controlled STNOs (MSN), which shows encouraging potential to be used for wireless communication. Then I turn to the study of AOS effect in both ferri- and ferro-magnets, involving ultrafast magnetization dynamics. I constructed magnetization state diagrams for GdFeCo and CoPt which allow to quickly visualizing the laser pulses conditions (fluence and pulse duration) required for AOS. These results provide crucial guidelines to engineer energy efficient all optical magnetization switching.

This thesis is divided into six chapters. First, an introduction and a state-of-the-art for both STNOs and AOS are presented. In the second chapter, the experimental methods used to fabricate and characterize the studied samples are introduced in detailed. In the third and fourth chapters, I present the results of the studies on magnetization dynamics in planar and perpendicular STNOs, respectively. In addition, a novel strategy is proposed for modulation of microwave signals. Finally in fifth and sixth chapters, I describe my study of the magnetization state diagrams obtained for materials showing AO-HIS and AO-HDS. I finish with a conclusion and some perspectives.

Introduction générale

Les réseaux de capteurs sans fil (RCS) sont les principaux composants de l'internet des objets (IdO) et ont suscité une grande attention dans l'industrie et dans la communauté académique. Les RCS sont des nœuds interconnectés qui communiquent sans fil pour collecter les données liées au milieu environnant [1-3]. Bien que des avancées significatives aient été faites au cours des dernières années, deux problèmes subsistants doivent être résolus pour permettre une utilisation extensive des RCS.

Il est estimé qu'en 2025 l'IdO représentera de 41.6 milliards d'appareils connectés, générant 79.4 zettabytes (ZB) de données [4]. Une méthode de stockage d'information ultrarapide est donc un besoin urgent. De plus les RCS nécessitent un grand nombre de nœuds. L'information est transmise entre ces nœuds par communication sans fil. Tout cela a comme conséquence que la communication est responsable de la grande majorité de la consommation d'énergie du système. Il est aujourd'hui pressant de développer de nouveaux types de dispositifs microondes. Des plus petits dispositifs, des moins énergivores.

L'électronique de spin répond à ces problématiques. L'excitation de l'aimantation peut engendrer plusieurs réponses dynamiques tels que la désaimantation, la précession ou le retournement. Une précession stable peut être obtenue en utilisant un courant de spin par le couple de transfert de spin ou le couple de spin orbite. La fréquence de précession étant couramment de l'ordre de quelques GHz (cela correspond à une période de centaines de picosecondes), il a été montré qu'elle peut générer des microondes dans les jonction à tunnel magnétiques ou les valves de spin, constituant ainsi un nano-oscillateurs à transfert de spin (NOTS). Les NOTS sont des successeurs potentiels aux émetteurs et récepteurs de signaux radio fréquence à base de transistors. En comparaison des oscillateurs électroniques conventionnels, les NOTS ont l'avantage d'être opérationnels sur une grande plage de fréquence, avoir de plus petites tailles latérales (jusqu'à 50 fois) et une plus faible consommation en énergie [5-7].

Le retournement de l’aimantation est déjà à l’œuvre dans les dispositifs de stockage d’information. Dans un disque dur, le principal support de stockage de masse, l’information est écrite en fixant l’aimantation du matériau soit « vers le haut », soit « vers le bas ». Pour augmenter la densité de stockage, il faut réduire le volume de chaque bit. Il faut donc chercher des matériaux à grande anisotropie perpendiculaire magnétique K_u comme support de stockage pour maintenir la stabilité de l’information malgré l’activation thermique. Malheureusement de tels matériaux ont aussi un fort champ coercitif. Comme le champ magnétique maximum généré par la tête d’un disque dur est environ de 1 Tesla (à cause de la taille de la pointe), il y a une limite à supérieure à l’anisotropie magnétique perpendiculaire que l’on peut utiliser. Dans ce contexte, la découverte de Stanciu *et al.* en 2007 qu’une impulsion de laser femtoseconde peut retourner l’aimantation d’un alliage de GdFeCo pourrait conduire à un changement de paradigme [8]. Ce phénomène nommé retournement tout optique (RTO), non seulement contourne la nécessité d’un champ magnétique, mais aussi réduit le temps d’écriture jusqu’à la picoseconde.

En dépit d’efforts de recherche intensifs, les applications pratiques des NTOS et du RTO semblent encore lointaines. Dans les systèmes de communication sans fil, les NOTS sont utilisés en tant qu’oscillateurs locaux pour générer un courant qui est ensuite modulé par un signal RF grâce à un mélangeur RF pour obtenir un signal total intermodulé. Cependant la puissance des NOTS est trop faible pour faire fonctionner un mélangeur RF. Récemment, le groupe de U. Ebel à Spintec a proposé d’implémenter la modulation par déplacement de fréquence (MDF) dans les NOTS en effectuant une modulation numérique du courant, permettant donc de se passer d’un mélangeur RF [9]. Leur travail démontre la faisabilité d’une utilisation des NOTS pour la communication sans fil mais les conditions optimales de la MDF pour les NOTS restent à déterminer. Le RTO a aussi quelques problèmes. A ce jour, deux différents types de RTO ont été identifiés. Le premier est le retournement tout optique indépendant de l’hélicité (RTO-IH) où une seule impulsion laser suffit à renverser l’aimantation. Le RTO-IH n’est faisable que pour un nombre très limité de matériaux tels que les alliages ferrimagnétiques à base de Gd [10-12]. Le deuxième type, le retournement tout optique dépendent de l'hélicité (RTO-DH), nécessite plusieurs impulsions pour obtenir le renversement de l'aimantation. Cependant le RTO-DH est communément observé dans un large gamme de matériaux (ferrimagnétiques, ferromagnétiques, alliages, empilements, cristallisés, amorphes) [13-15]. En ce qui concerne le RTO-DH, il a été démontré que la fluence seuil de renversement diminue rapidement lorsque l'on augmente la durée de l'impulsion. Il est donc préférable d'utiliser un laser femtoseconde pour obtenir le RTO-IH. Cependant les source laser semi-conductrices sont à ce jour seulement capable de générer des impulsions durant au minimum quelques picosecondes. Dans le cas du RTO-DH, le consensus est que le retournement de l'aimantation se fait en une étape de nucléation de domaines magnétiques suivie d'une étape de propagation. Des centaines d'impulsions laser sont nécessaires dans ce cas, éloignant ainsi une perspective d'application.

Dans ce manuscrit, je présenterai la dynamique de l'aimantation dans des NOTS parallèles et perpendiculaire sous différents courants et champs magnétiques en utilisant un analyseur spectral pour trouver les conditions optimales pour la génération de microondes. A partir de ces résultats, je proposerai une nouvelle approche de modulation, à savoir les NOTS contrôlés par memristor, qui montre un potentiel encourageant pour la communication sans fil. Ensuite j'entamerai une étude du RTO dans les ferri- et ferromagnétiques en incluant la dynamique de l'aimantation ultrarapide. J'ai construit des diagrammes d'états pour le GdFeCo et le Co/Pt qui permettent une visualisation rapide des condition de l'impulsion (fluence et durée) nécessaires au RTO. Ces résultats sont des guides précieux dans la minimisation de l'énergie nécessaire au RTO.

Ce manuscrit est divisé en six chapitres. En premier lieu je présente une introduction et un état de l'art pour à la fois les NOTS et l'AOS. Dans le second chapitre, les méthodes expérimentales utilisées pour fabriquer et caractériser les échantillons sont présentées en détail. Dans les troisième et quatrième chapitres, je présente les résultats des études de la dynamique de l'aimantation respectivement dans les NOTS planaires et perpendiculaires. De plus, une nouvelle stratégie est proposée pour la modulation de signal microonde. Finalement dans les cinquième et sixième chapitres, je présente mon étude des diagrammes d'état de l'aimantation obtenue pour des matériaux où se produisent les RTO-IH et le RTO-DH. Je clos ce manuscrit par une conclusion et quelques perspectives.

1 Fundamentals

1.1 Spin transfer torque nano-oscillators (STNOs)

STNOs are a new type of microwave devices which make use of magnetoresistance (MR) effect and spin transfer torque (STT) effect. In this section, I will introduce these two effects in detail. Furthermore, depending on the magnetic configuration and physical structure, STNOs can be divided into several categories, which will also be illustrated in this section.

1.1.1 Magnetoresistance effect

AMR

Magnetoresistance (MR) effects are very important phenomena in spintronics, which are widely used in various sensors and memory devices. The first discovered magnetoresistance effect is anisotropic magnetoresistance (AMR). In 1857, Thomson found that the resistance of Fe and Ni changes with the direction of their magnetization direction [16]. In 1975, McGuire *et al.* found similar phenomena in transition metals such as Fe, Co, Ni and their alloys, which proves that AMR is a general effect [17]. AMR is commonly described to be caused by spin-orbit interactions, which results in anisotropic mixing of the conduction bands of majority and minority electrons [3]. In this case, the resistivity of materials can be expressed as:

$$\rho(\theta) = \rho_{\perp} + (\rho_{\parallel} - \rho_{\perp}) \cos^2(\theta) \tag{1.1}$$

Here θ is the angle between the magnetic moment and the injected current in the material. $\rho_{\parallel}$ and $\rho_{\perp}$ are the resistivities of the material when θ=0° and 90°, respectively [18]. Though AMR ratio defined as $(\rho(\theta) - \rho_{\perp})/\rho_{\perp}$ is very low (3%-5%), it still attracted much attention of industry. From 1992 to 1998, the read heads for the hard disk was based on AMR effects, which marks the beginning of rapid growth of memory density as shown in Figure 1-1.

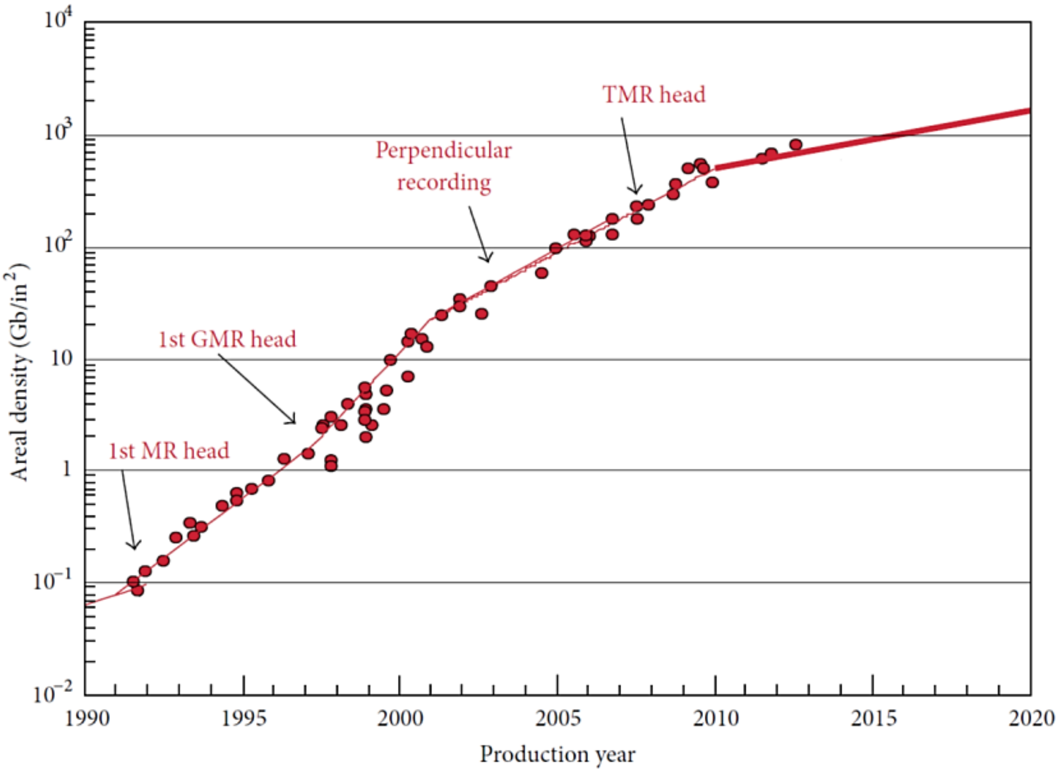

Figure 1-1 Evolution of area density of HDD as a function of the production year with the development of magnetic recording technology. Figures extracted from [19].

GMR

As can be seen from the figure 1-1, the read head based on the AMR effect was later replaced by GMR (Giant magnetoresistance) head. The GMR effect is observed in ferromagnetic/nonmagnetic/ferromagnetic (FM/NM/FM) multilayer film systems. In 1988, P. Grünberg *et al.* discovered that Fe/Cr/Fe multilayers exhibits antiferromagnetic coupling if the thickness of Cr is around a certain value [20]. Later, they found that the resistance of such stacks differs when the two magnetic layers are arranged in a parallel or an antiparallel allignement [21]. In most cases, the resistance of these samples in magnetic parallel configuration is larger than that in magnetic antiparallel configuration. Compared with AMR effect in single Fe layer, Fe/Cr /Fe multilayers exhibit much larger magnetoresistance ratio. Meanwhile, Fert *et al.* found similar effects in Fe/Cr superlattice grown by molecular beam epitaxy (MBE) method[22]. Later, this effect was found to be present in a large variety of materials such as Co/Au/Co、Co/Cu/Co、Fe/Au/Fe、$[Co/Ru]_n$ and $[Co/Cr]_n$ multilayers [23-31].

In such cases, the resistance of the multilayer films is determined by the angle β between magnetization of the two ferromagnetic layers, which is expressed by formula 1.2:

$$\mathrm{R}(\beta) = R_P + \frac{1}{2}(R_{AP} - R_P)(1 - \cos(\beta)) \tag{1.2}$$

Here, $\mathrm{R}(\beta)$ is the resistance of the film at a given angle β, R_P and R_{AP} represent the resistance when the magnetization of the two ferromagnetic layers are parallel and antiparallel, respectively. The GMR ratio effect is commonly defined as:

$$\mathrm{GMR} = \frac{R_{AP} - R_P}{R_P} \times 100\% \tag{1.3}$$

The measurement of the GMR effect in the multilayer films was first performed using a four-point probe technique for which the injected current flows in the direction parallel to the film surface, which is also called the current-in-plane model (CIP). Based on CIP measurements, Grünberg *et al.* obtained 3% GMR ratio in Fe/Cr/Fe film at room temperature and Fert *et al.* achieved 50% GMR ratio in Fe/Cr superlattice film at 4.2 K [22,23].

Soon afterwards, current-perpendicular-to-plane (CPP) geometry was used as proposed by Pratt *et al.* in 1991 [28]. With this geometry, they obtained a very high MR ratio for Ag/Co multilayer film, which is about 10 times larger than that measured using CIP model. Based on CPP geometry, Dieny *et al.* then demonstrated a Spin valve (SV) structure which indeed promotes the application of CPP-GMR[32]. Different from the initial CPP geometry, an antiferromagnetic layer is added next to one of the ferromagnetic layer in SV. Through exchange coupling, this antiferromagnetic layer can make the magnetization of one FM layer fixed while the other FM layer can be easily reversed by an external magnetic field, similar to the structure of a valve. Based on this, IBM launched the commercial CPP-GMR head in 1998.

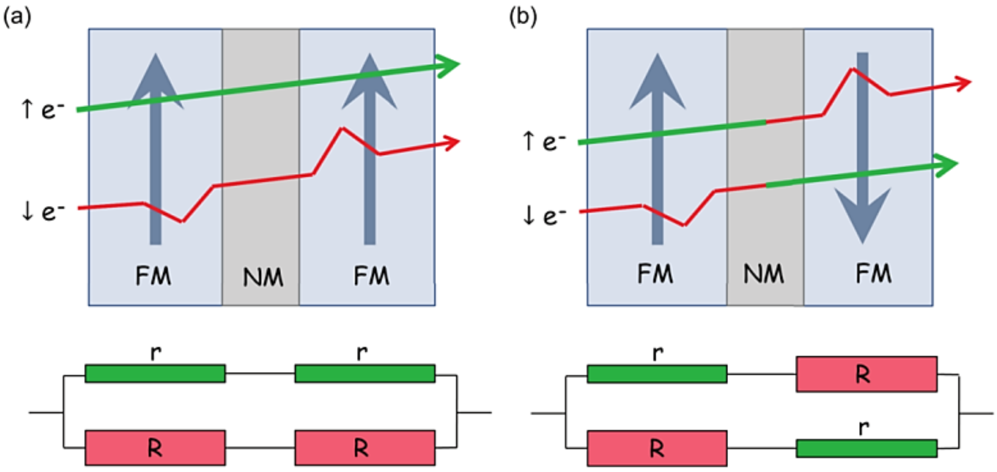

Figure 1-2 Two-current model in FM/NM/FM multilayers. (a) and (b) are schematic circuits when the two FM layers are arranged in parallel and antiparallel. The interfaces of the multilayers are considered as variable resistors depending on the spin direction of the electrons. Figures extracted from [33].

In 1993, Valet and Fert first presented the theoretical study of CPP-GMR[34]. They proposed a model in which the majority and minority electrons flow via different paths. As shown in Figure 1-2, in these two paths, the interfaces of the stack are considered as variable resistors which depend on the spin direction of electrons. Note that this model works only if the thickness of the nonmagnetic layer is smaller than the spin diffusion length.

TMR

In parallel with the evolution of the GMR, another similar structure named magnetic tunnel junction (MTJ) also attracted interests of researchers. Different from the "spin valve", the spacer layer between the two ferromagnetic layers in MTJ is an insulating layer. MTJ also exhibits MR effect which is called the tunneling magnetoresistance (TMR). TMR originates from quantum tunneling of electrons, that is, the electron has a probability to pass a potential barrier which is higher than the electron energy. The MR ratio induced by TMR effect is commonly expressed by:

$$\mathrm{TMR}=\frac{G_P-G_{AP}}{G_{AP}}=\frac{R_{AP}-R_P}{R_P}\times 100\% \tag{1.4}$$

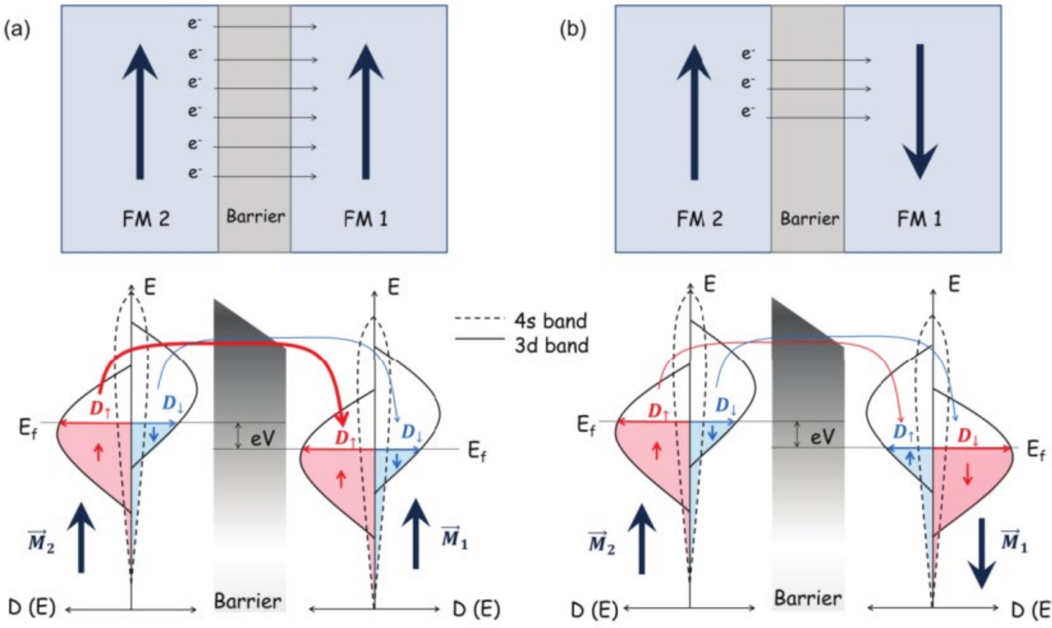

Figure 1-3 Schematic view of tunneling process (upper panel) and band structures (lower panel) in MTJ when the two ferromagnetic layers (FM1 and FM2) are arranged in parallel (a) and antiparallel (b). Figures extracted from [33].

The TMR effect was first discovered by Julliere *et al.* in Fe/Ge/Co multilayers in 1975 [35]. A 14% TMR ratio was obtained at low temperature (4.2K). In addition, they proposed a model in which the tunneling probability of conductive electrons is determined by the number of majority and minority electrons at Fermi level, as shown in Figure 1-3. Thus, the conductance of MTJ is defined as:

$$G_P \propto D_\uparrow^{FM1} D_\uparrow^{FM2} + D_\downarrow^{FM1} D_\downarrow^{FM2}$$
$$G_{AP} \propto D_\uparrow^{FM1} D_\downarrow^{FM2} + D_\downarrow^{FM1} D_\uparrow^{FM2} \qquad (1.5)$$

According to formula 1.2, 1.3 and 1.4, TMR ratio can be rewritten as:

$$TMR = \frac{G_P - G_{AP}}{G_{AP}} = \frac{D_\uparrow^{FM1} D_\uparrow^{FM2} + D_\downarrow^{FM1} D_\downarrow^{FM2} - \left(D_\uparrow^{FM1} D_\downarrow^{FM2} + D_\downarrow^{FM1} D_\uparrow^{FM2}\right)}{D_\uparrow^{FM1} D_\downarrow^{FM2} + D_\downarrow^{FM1} D_\uparrow^{FM2}} \qquad (1.6)$$

and subsequently

$$TMR = \frac{(D_\uparrow^{FM1} - D_\downarrow^{FM1})(D_\uparrow^{FM2} - D_\downarrow^{FM2})}{D_\uparrow^{FM1} D_\downarrow^{FM2} + D_\downarrow^{FM1} D_\uparrow^{FM2}} \qquad [25] \qquad (1.7)$$

The spin polarization defined by Juliere is expressed as:

$$p = \frac{D_{\uparrow}^{FM1} - D_{\downarrow}^{FM2}}{D_{\uparrow}^{FM1} + D_{\downarrow}^{FM2}} \tag{1.8}$$

Thus another form of TMR ratio can be expressed as:

$$TMR = \frac{2p^{FM1}p^{FM2}}{1 - p^{FM1}p^{FM2}} = \frac{R_{AP} - R_P}{R_P} \tag{1.9}$$

Where p^{FM1} and p^{FM2} are the spin polarization of the two ferromagnetic layers. From this model, it can be concluded that the TMR ratio is closely related to the spin polarizations of the two ferromagnetic layers. Moreover, a large TMR ratio can be enhanced by using materials with high spin polarization. Due to its weak effect, the industry did not give more attention to TMR until 1995, Miyazaki and Tezuka achieved 18% TMR ratio at room temperature and 30% at 4.2K in the Fe/Al_2O_3/Fe structure [36].

In 2001, Mathon and Butler independently predicted that a symmetric MTJ structure could result in a high TMR ratio due to the coherent tunneling process [37,38]. Based on first-principles calculations, they predicted that the Fe(100)/MgO(100) /Fe(100) structure should have a TMR ratio exceeding 1000%. They concluded that the tunneling conductance is significantly influenced by the symmetry of the Bloch states in the electrodes. Figure 1-4 shows the DOS (Density of state) of majority and minority electrons in parallel configuration and antiparallel configuration. In parallel state, majority electrons from $\Delta1$ Bloch state can tunnel through the barrier efficiently while electrons from $\Delta5$ and $\Delta2$ decay very fast, as shown in Figure 1-4(a-b). Meanwhile, because of the absence of $\Delta1$ Bloch state, the tunneling probability for the minority electrons is much lower than that for majority electrons, as shown in Figure 1-4(c-d). In antiparallel configuration, due to the lack of corresponding states in another FM layer, the tunneling DOS continuously decrease, leading to a larger resistance of MTJ.

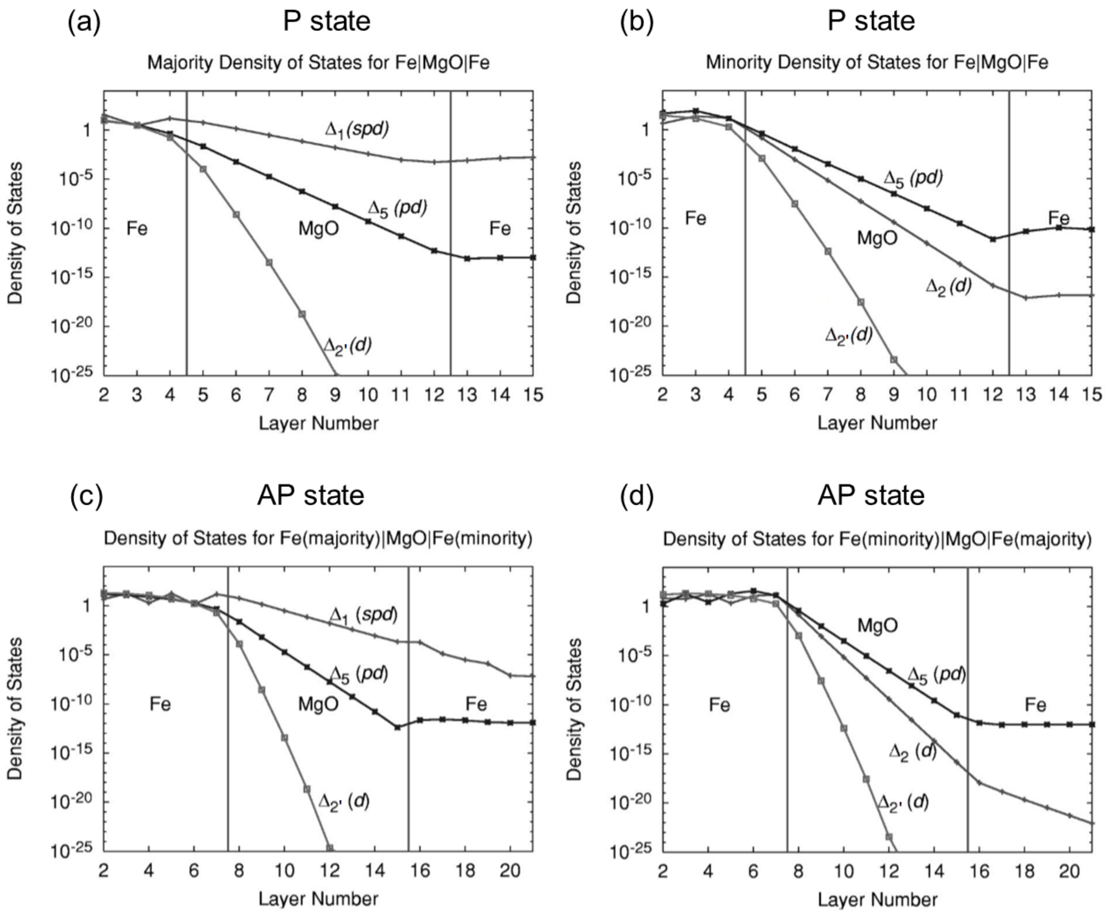

Figure 1-4: Tunneling DOS of majority and minority electrons for Fe(100)/MgO(100) /Fe(100) structure in parallel (P) configuration (a)(b) and antiparallel configuration (c)(d). Figures extracted from [38].

In addition, the barrier plays an important role in the tunneling process of conduction electrons as shown on Figure 1-5 schematically in Fe(001)/MgO(001)/Fe(001) and Fe(001)/Al-O/Fe(001). Note that Al-O is amorphous in this case. It is seen that the electrons in Δ1, Δ5 and Δ2’ Bloch states in Fe(001)/Al-O/Fe(001) possess the same tunneling probabilities (the width of the arrows represent the tunneling probabilities). Thus the tunneling efficiency of electrons in Δ1 state is smaller than that in Fe(001)/MgO(001)/Fe(001) structure.

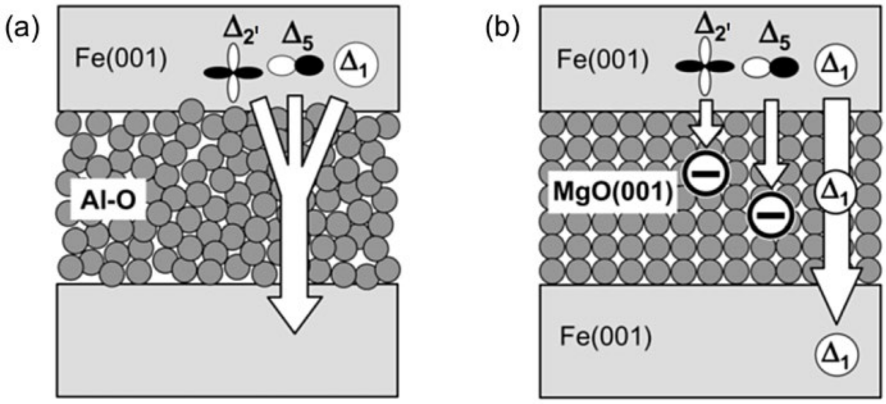

Figure 1-5 Schematic illustration of the difference of tunneling process between Fe(001)/MgO(001)/Fe(001) and Fe(001)/Al-O/Fe(001) structures, The width of the arrow indicate the tunneling probability. Al-O is amorphous. Figures extracted from [38]

In short, Fe and crystalline MgO have very similar band structure, thus efficient tunneling of conduction electrons is allowed when the two FM layers are arranged in parallel. Later, these predictions were confirmed. In 2004, Yuasa *et al*. and Parkin *et al*. independently obtained about 200% TMR ratio in Fe/MgO/Fe multilayers [39, 40]. With the development of material technology, the highest reported TMR ratio so far has reached about 604%, which was achieved by Ikeda *et al*. in 2008 [41].

From the application point of view, the second major cHallenge is how to increase the breakdown voltage of the MTJ while maintaining a low resistance area product (RA)., A lower RA value allows for a better matching of impedance with the outer circuit and a high breakdown voltage can ensure a longuer lifetime for the devices. So far the most reported value of these two parameters are around 1V and 1Ωμm^2. In 2006, Seagate Technology first launched the commercial TMR read head based on MgO-MTJ. Compared with GMR-based read head, it shows a much higher sensitivity which is about three times larger. Moreover, TMR read head exhibit a longer lifetime and lower error rate. The maximum storage density is about 300 GB/in^2. One year later, Fujitsu produced the TMR read head compatible with 500 GB/in^2 storage density. To date, this value has already exceeded 1000 GB/in^2.

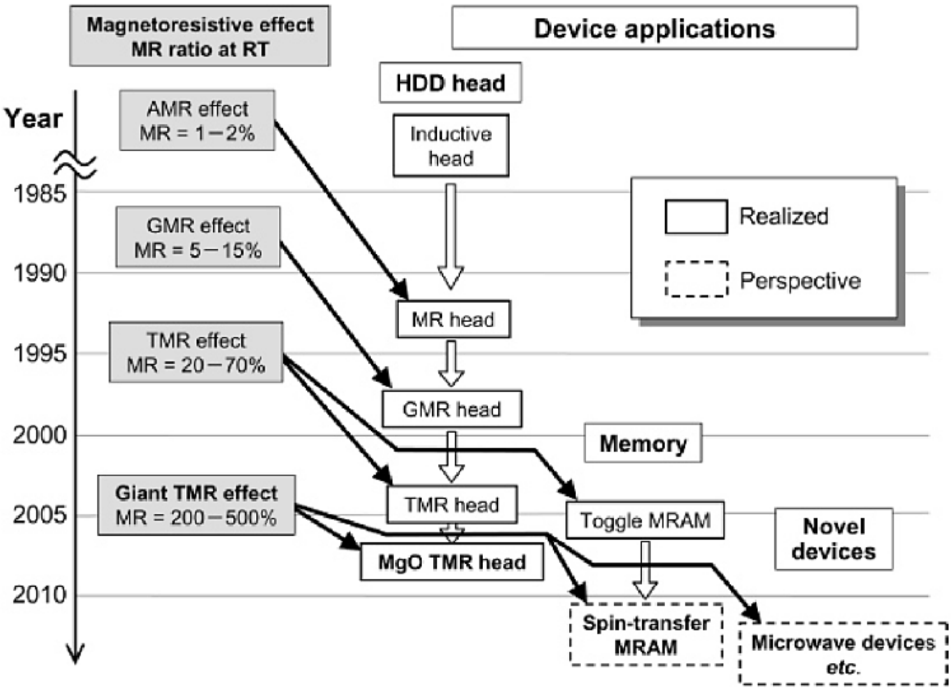

Figure 1-6 New spintronic devices based on MR effect. Figure extracted from [33].

The discoveries of AMR, GMR and TMR have greatly promoted the development of storage technology, In addition, based on these effects, a variety of novel spintronic devices have also emerged, as shown in Figure 1-6.

1.1.2 Spin-transfer-torque-based phenomena

Spin transfer torque

In 1996, Slonczewski and Berger independently predicted the spin transfer torque (STT) in magnetic materials [42, 43]. Based on STT effect, the magnetization of free layer in SV or MTJ can be manipulated by the spin polarized current. STT effect is considered to be another most important discovery in spintronics after the GMR. Fig.1-7 schematically demonstrates the mechanism of STT.

For a FM/NM/FM trilayer, when conduction electrons move from the pinned layer to the free layer as shown in Figure 1-7(a)(current flows from the free layer to the pinned layer), electrons whose spin directions are the same as the magnetization direction of the pinned layer can pass more easily. On the other hand, the electrons with the opposite spin direction are scattered by the pinned layer. As a consequence, the current is polarized along the magnetization direction of the pinned layer. When the spin-polarized electrons pass through the spacer layer, their spin directions remain unchanged due to the small thickness of the spacer layer. Finally, after the electrons reach the free layer, they will exert a torque on the local magnetization. In this case, the role of the STT is to make the magnetization of free layer parallel with that of reference layer. On the contrary, when conduction electrons flow from the free layer to the pinned layer as shown in Figure 1-7(b), electrons whose spin direction are different from the magnetization of the pinned layer will be reflected back and then exert the STT on the free layer. In this case, the STT tends to align the two ferromagnetic layers anti-parallel.

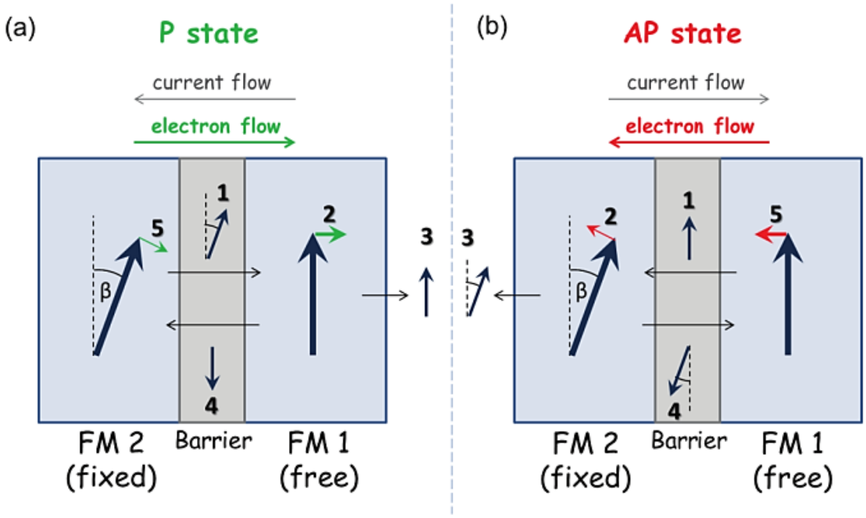

Figure 1-7 Schematic view of STT effect in MTJ when the two ferromagnetic layers are arranged in parallel (a) or antiparallel state (b).Taken from [33].

Landau-Lifshitz-Gilbert (LLG) equation

The magnetization dynamics in a thin magnetic film can be described by Landau-Lifshitz-Gilbert (LLG) equation which is expressed as [44, 45]:

$$\frac{\mathrm{d}\boldsymbol{m}}{dt} = -\gamma\mu_0\boldsymbol{m}\times\boldsymbol{H}_{eff} + a\left(\boldsymbol{m}\times\frac{\mathrm{d}\boldsymbol{m}}{dt}\right) \tag{1.10}$$

Where γ is gyromagnetic ratio, μ_0 is vacuum permeability. $\boldsymbol{H}_{\mathrm{eff}}$ is the effective field, a is the Gilbert damping constant. $\boldsymbol{m}$ is the unit vector of the magnetization. It is worth noting that $\boldsymbol{H}_{\mathrm{eff}}$ is a vector-sum of all the magnetic field that influence the magnetization, which can be defined as

$$\boldsymbol{H}_{\mathrm{eff}} = \boldsymbol{H}_{\boldsymbol{a}} + \boldsymbol{H}_{\boldsymbol{k}} + \boldsymbol{H}_{\boldsymbol{d}} + \boldsymbol{H}_{\boldsymbol{ex}} \tag{1.11}$$

where H_a is external magnetic field, H_k is anisotropy magnetic field which can be calculated by $H_k = 2H_u/(\mu_0 M_s)$, H_d is demagnetization field, and H_{ex} represent the exchange interaction field.

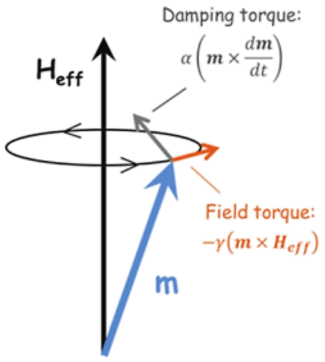

Figure 1-8 Schematic view of torques involved in LLG equation which describes the dynamics of magnetization.

By solving the LLG equation, we can obtain the trajectory of the magnetic moment motion. The first term on the right side of formula (1.10) indicates the torque exerted by the effective field. The direction of this torque is always perpendicular to the direction of the effective field. As a consequence, the magnetic moment precesses around $\boldsymbol{H}_{\mathrm{eff}}$. Thus it is also called the precession torque. $a(\boldsymbol{m} \times \mathrm{d}\boldsymbol{m}/dt)$ represents the damping torque which point to the axis of precession, tending to suppress the motion of magnetizations. Under the action of damping torque, the magnetization of the thin film will eventually reach an equilibrium state in which it is aligned along $\boldsymbol{H}_{\mathrm{eff}}$. These torques are schematically shown in Figure 1-8.

STT-induced magnetization switching and precession

As mentioned above, the spin polarized current will exert STT on the magnetization when passing through a magnetic layer. Thus, in SV or MTJ, STT should be introduced to LLG equation. Slonczewski first gave the mathematical description of STT and the so-called Landau-Lifshitz-Gilbert-Slonczewski (LLGS) equation can be then given by [46,47]:

$$\frac{\mathrm{d}\boldsymbol{m}_f}{dt} = -\gamma_0\left(\boldsymbol{m}_f \times \boldsymbol{H}_{eff}\right) + a\boldsymbol{m} \times \frac{\mathrm{d}\boldsymbol{m}_f}{dt} - \gamma_0\eta\frac{\hbar J_{app}}{2e\mu_0 M_s t}\boldsymbol{m}_f \times \left(\boldsymbol{m}_f \times \boldsymbol{m}_p\right) \quad (1.12)$$

Here $\boldsymbol{m}_f$ and $\boldsymbol{m}_p$ are, respectively, the unit vector of magnetization of free layer and pinned layer. α is the natural damping constant, γ_0 is the gyromagnetic factor given by $\gamma_0 = \mu_0\gamma$ with μ_0 is vacuum permeability, M_s is the saturation magnetization, $\hbar$ is Planck constant, J_{app} is the injected current, t is the thickness of the STNO device and η is the spin polarization value.

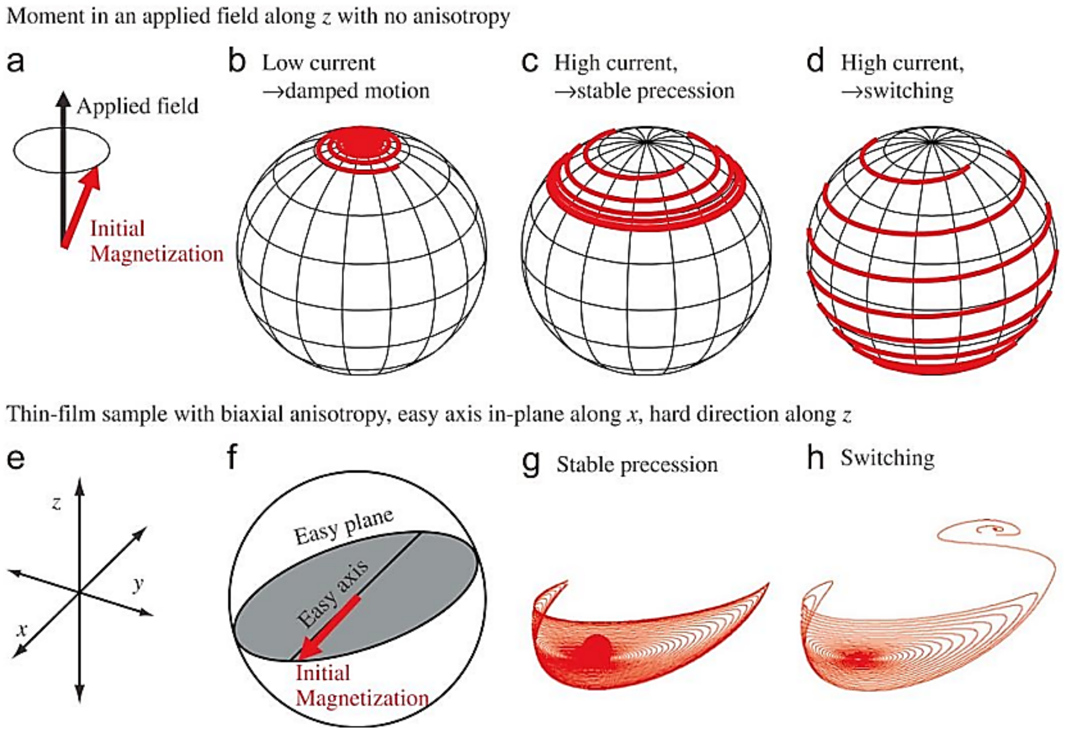

Figure 1-9 (a-d) Trajectory of magnetization in an applied field along z axis with no anisotropy for different applied current. (e)-(h) Trajectory of magnetization in a thin film with biaxial anisotropy, easy axis in-plane along x, hard direction along z. Figures extracted from [48].

According to LLGS equation, the magnetization dynamics of free layer in MTJ or SV is determined by precession torque, damping torque and STT. As a consequence, three different types of motion can be identified as the injected current I_e increases. As shown in Figure 1-9 (a-d), when I_e is small, the current-induced STT is smaller than the damping torque, consequently a damped precession is observed. When the current increases to a certain value, the damping torque is completely offset by STT, leading to a stable precession of the magnetization. If the current further increases, the cone angle of magnetization precession will continuously increase and eventually switch to another direction. It should be noted that the motion trajectories shown in Figures 1-9 (a-d) are calculated in the ideal case (no magnetocrystalline anisotropy). In fact, the magnetic ultra-thin films usually manifest biaxial anisotropy and the precession trajectory of the magnetization in this case is elliptical, as shown in Figures 1-9 (e)-(h). The frequency of precession can be obtained from the Kittel formula expressed as [49]:

$$f_0 = \frac{\gamma_0}{2\pi}\sqrt{\left(H_{app} + H_{an} + H_d\right)\left(H_{app} + H_{an} + H_d + 4\pi M_{eff}\right)} \qquad (1.13)$$

Here H_{app} is the applied magnetic field, H_{an} accounts for uniaxial easy-axis anisotropy and H_{d} models the coupling from the fixed layer. STT provides an all-electrical method to manipulate the magnetization, which could be utilized to switch the magnetization in magnetic storage devices or induce magnetization precession in STNOs.

1.1.3 Microwave generation in GMR/TMR structures

As discussed in 1.1.1, the resistance of a SV/MTJ is determined by the angle between magnetizations of two ferromagnetic layers for a given device. Thus a steady magnetization precession in free layer can result in a periodic change of resistance of SV/TMR. Meanwhile, the injected current is constant. As a consequence, a high-frequency AC voltage is obtained in this case. Figure 1-10 schematically show the process of microwave generation.

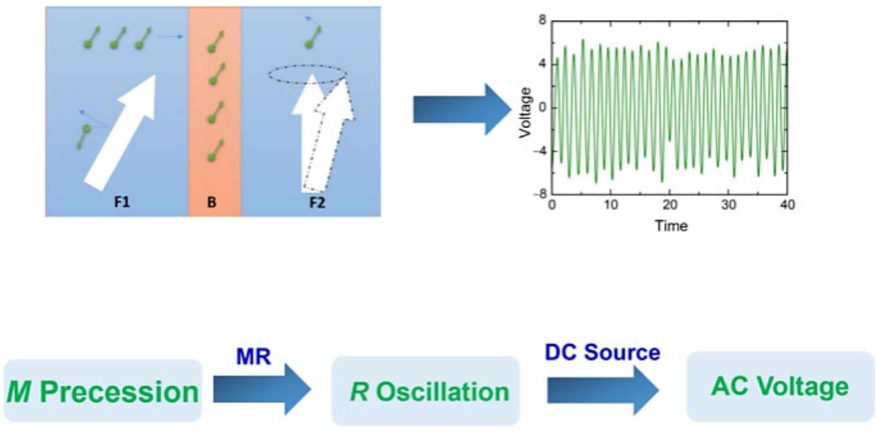

Figure 1-10 The process of microwave generation in MTJ and SV.

STNO with different device architectures

In 2003, Kislev *et al.* first reported the microwave emission in an elliptical pillar-shaped spin valve [Co(40 nm)/Cu(10 nm)/Co(3 nm)] prepared using electron beam lithography (EBL) [5], as shown in Figure 1-11 (a). They confirmed that the frequency of microwave signal can be modulated by changing the external magnetic field [(Figure 1-11(b)].

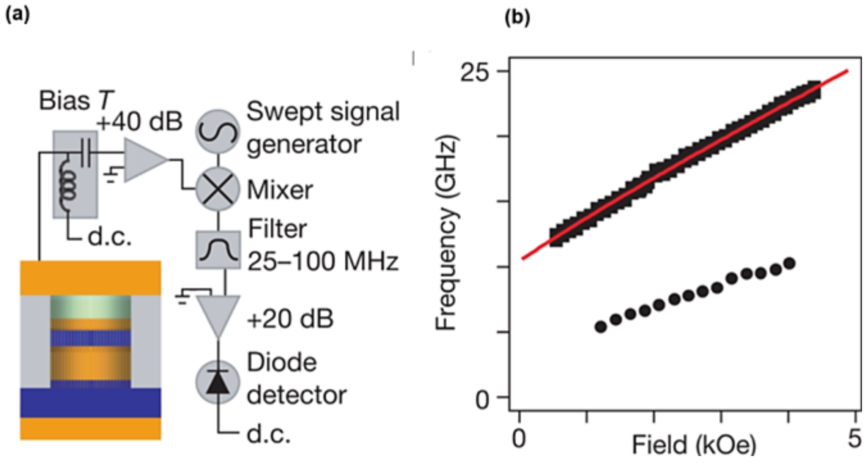

Figure 1-11 (a) Schematic view of the measurement set-up used for microwave detection for STNO, the bias T is used to separate the AC component from the output signal (b) Dependence of frequency on external magnetic field in different precession modes. Figures extracted from [5]

In 2004, Rippard *et al.* reported direct measurement of microwave signal in spin valve with a structure of $Co_{90}Fe_{10}$ (20nm)/Cu (5nm)/$Ni_{80}Fe_{20}$ (5nm) [6]. Different from the nano-pillar STNO, the core layers are intact without micro-fabrication process. The device is contacted with current source via microwave probes, which forms the so-called point-contact STNO, as displayed in Figure 1-12(a).

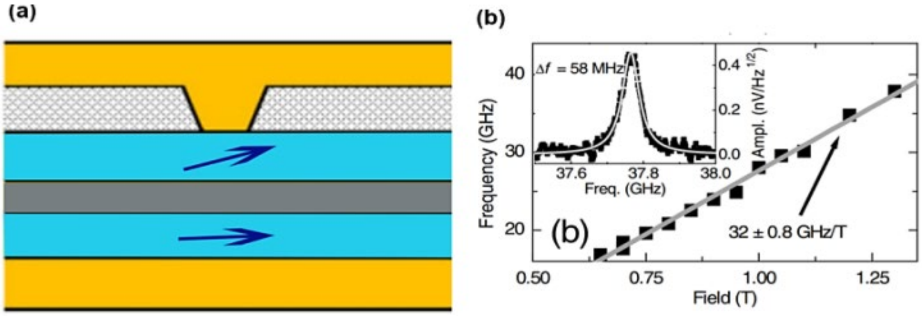

Figure 1-12 (a) Structure of nano-sized point-contact STNO. (b) The dependence of frequency of microwave emission on external magnetic field. Inset shows the power spectrum density. Figures extracted from [6].

Generally, the point-contact STNO possesses a narrower linewidth compared with the nano-pillar STNO, resulting in the microwave emission with higher Q factor. However, as shown in Figure 1-13, due to the presence of non-negligible shunt current in the point-contact structure, the efficiency of the applied current is very poor, leading to a low MR ratio [7].

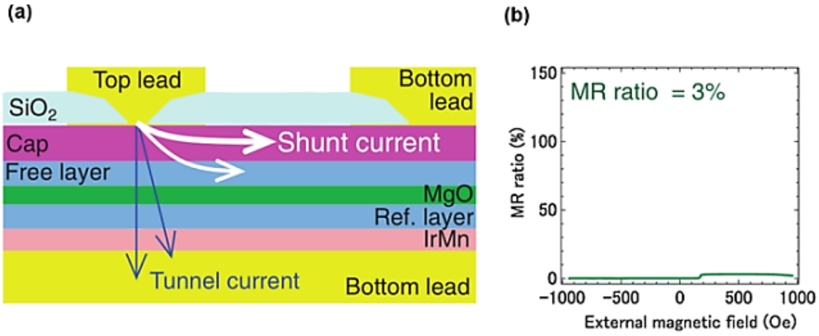

Figure 1-13 (a) Schematic view of current distribution in GMR structure. (b) The shunt current lead to a low MR ratio in GMR structure. Extracted from [7].

STNO with different magnetization configurations

In-plane STNO

Based on the magnetization configuration of MTJ or SV, STNOs can be divided into three categories. Initially, most research works focused on in-plane STNOs in which free and fixed FM layers have an easy-plane magnetic anisotropy, meaning that the magnetic moments lie in plane if no external magnetic field is applied. Co, CoFe and NiFe are commonly used materials with in-plane anisotropy. In this case, as discussed above, when a proper DC current is injected, the magnetic moments of the free layer will precess continuously. But it should be noted that the angle θ between moments of free and fixed layer remains unchanged during the precession, as shown in Figure 1-14. In this case, the injected current and device resistance are both constant, meaning that there is no AC signal output. Only when a large non-collinear external magnetic field is applied, the symmetry of the magnetic moments between the free layer and the fixed layer is broken; microwave signals could then be obtained.

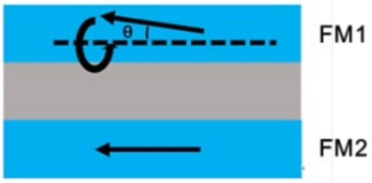

Fig 1-14 Schematic representation of principle of in-plane STNOs

Perpendicular STNO

For perpendicular STNO, both the magnetic free layer and pinned layer exhibit perpendicular magnetic anisotropy, as shown in Figure 1-15. Compared with in-plane STNOs, perpendicular STNOs show better thermal stability and scalability. Co/Pt, Co/Ni and Co/Pd multilayers are typical structures showing strong perpendicular magnetic anisotropy. Similar to the in-plane STNOs, external magnetic field is needed to obtain microwave emission for perpendicular STNOs.

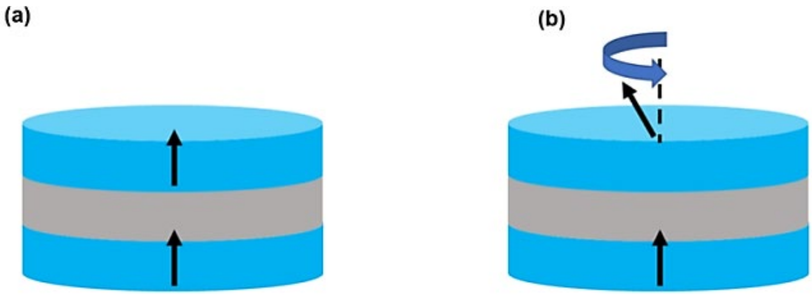

Figure 1-15 Schematic view showing the out-of-plane STNO before (a) and after (b) injection of spin current

Orthogonal STNO

As shown in Figure 1-16 (a), in the orthogonal STNOs, the directions of the fixed and the free layer in equilibrium state are orthogonal to each other. With the injection of a proper current, the magnetizations of free layer precess around the z-axis and the precession angle change periodically. Therefore, the orthogonal STNOs can generate microwave emission without the need of external magnetic field, as shown in Figure 1-16 (b).

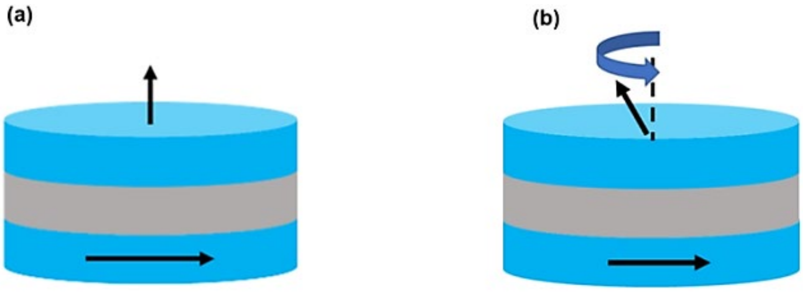

Figure 1-16 Schematic view showing the orthogonal STNO before (a) and after (b) injection of spin current

In 2013, Houssameddine *et al*. first reported microwave emission in an orthogonal STNO without the application of magnetic field [49]. The structure of the studied STNO is as follows: Pol/Cu/FeNi/Co/Cu/Co/IrMn. Here, Pol corresponds to Pt/(Co/Pt)$_5$/(Co/Cu/Co) and the bilayer FeNi/Co works as magnetic free layer. Compared with the above two types of STNO, the orthogonal STNOs usually exhibit a larger precession cone angle and thus a larger output voltage, as illustrated in Figure 1-17 (b).

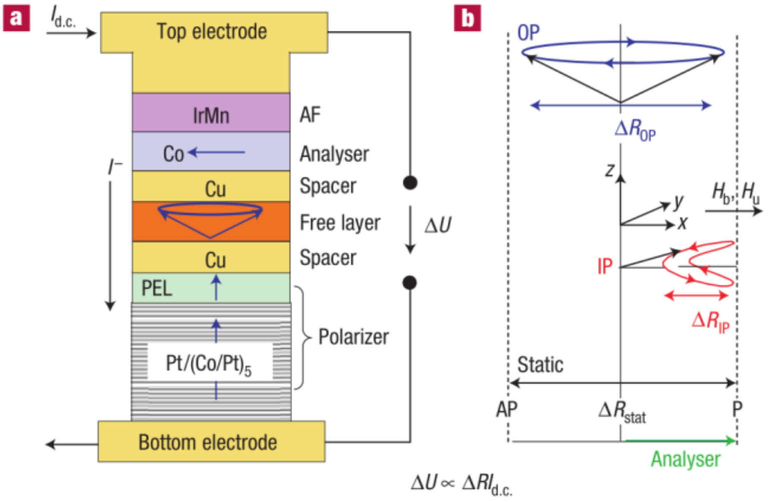

Figure 1-17 (a) Structure of studied orthogonal STNO in which Co/Pt multilayers constitute the perpendicular pinned layer while the bilayer FeNi/Co forms the free layer exhibiting in-plane magnetic anisotropy. Extracted from [49].

1.2 All optical magnetization switching

The rapidly increasing social needs for digital information drive the development of magnetic recording technology. In magnetic memory devices, digital information is stored by setting the magnetization of storage medium either "up" or "down". The data writing speed is therefore determined by how fast the setting process could be achieved, which is one of the most crucial parameters for storage devices.

The simplest way to switch the magnetization is by applying a magnetic field, which is used in Hard Disk (HD), the main product for mass data storage. When the magnetic field is strong enough, all the magnetic moments in the magnetic particles will be aligned along the direction of the external magnetic field, forming a macroscopic magnetization and realizing information storage [50]. Figure 1-18(a) schematically shows the structure of HD. The external magnetic field is applied via an electromagnet.

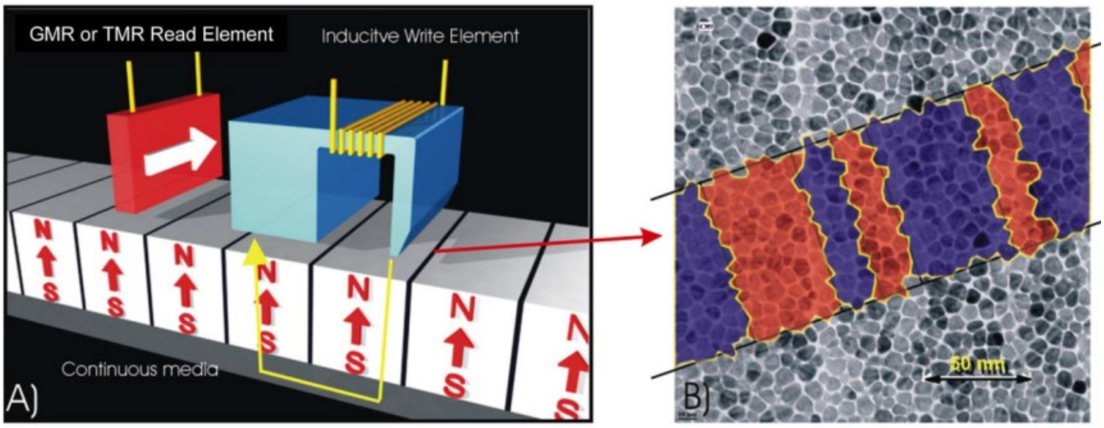

Figure 1-18 (a) A schematic of HD based on perpendicular recording technology; (b) Microscopic picture of storage medium taken via Transmission Electron Microscope (TEM). Magnetization up and down are indicated by red and blue respectively. Extracted from [50].

The control of magnetization using magnetic field has some drawbacks. For HD, with the increasing recording density, a larger magnetic field, i.e., a larger current is needed to fully switch the magnetization of storage bits, leading to higher power consumption. In addition, limited by the size of the write pole, the maximum applicable field is usually less than 2T. In such a context, various methods for manipulating the magnetization without the magnetic field have emerged recently, including strain[51,52], electric field[53,54], heat [55-62] and polarized current[63-77]. However, the switching process in the above cases usually happens via a coherent damping precession of the spins. The frequency of the precession is normally in the GHz range (corresponding to a period of hundreds of ps) and the reorientation process can take several nanoseconds. Therefore, a faster writing method is increasingly pursued by researchers.

In 2007, Stanciu *et al.* demonstrated the magnetization switching induced by circularly polarized femtosecond laser pulses in a 20 nm-thick $Gd_{22}Fe_{74.6}Co_{3.4}$, which has attracted much research interest [8]. Figure 1-19 shows the magneto-optical images of studied samples taken by Kerr microscope. As displayed in Figure 1-19(a), the thin film shows magnetic domains with different directions. M^+ and M^- represent orientations up and down, respectively. Figure 1-19(b) shows the magnetic configuration of the sample after exposure to femtosecond laser pulses with different polarizations. It can be seen that right circularly polarized σ+ (left σ−) laser pulses switch the magnetization from M−(M+) to M+ (M−). In contrast, the linearly polarized laser pulses (L) only result in a demagnetized state.

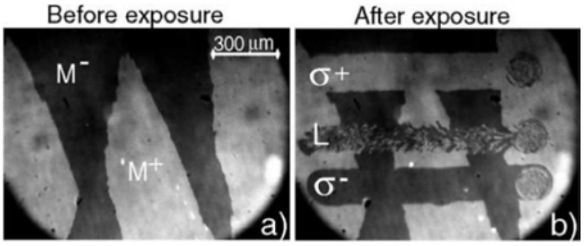

Figure 1-19 (a)Magneto-optical images showing initial magnetic configuration of a 20 nm-thick $Gd_{22}Fe_{74.6}Co_{3.4}$ (b) Magneto-optical images of $Gd_{22}Fe_{74.6}Co_{3.4}$ after exposure to laser pulses with different polarities. Σ+ (σ−) light reverses the magnetization of swept area “up” and “down” respectively. Extracted from [8].

GdFeCo alloys normally exhibit strong perpendicular magnetic anisotropy, which is promising to be applied in magnetic memory. It was proposed that the data writing in this case could be implemented by scanning a circularly polarized laser beam across the sample and simultaneously modulating the polarization of the laser beam, as shown in Figure 1-20. In this following part, I will briefly introduce the possible underlying mechanism and state-of-art of AOS.

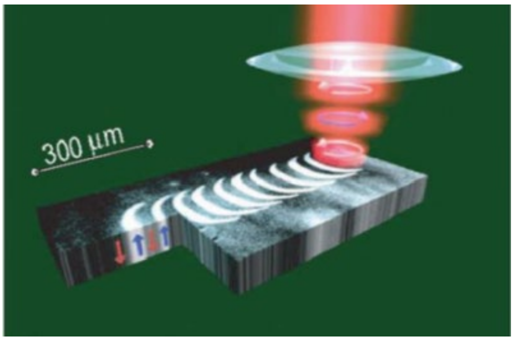

Figure 1-20 Demonstration of magnetic recording using polarized light. The digital information can be written by modulating the polarization of the laser beam. Extracted from [8]

1.2.1 Ultrafast laser-induced magnetization dynamics

In 1984, Agranat *et al.* first reported the evidence of ultrafast demagnetization in nickel films induced by ultra-short laser pulses [78]. Their results show that the nickel film with a 50-100 nm thickness demagnetized after exposure to a laser pulse with a 1-40 ns pulse duration. However, such a phenomenon was not observed when the pulse width is 5-20 ps. Consequently, they concluded that the demagnetization time in nickel film is on a time scale of 1-40 ns. In 1990, with the help of time-resolved spin-polarized emission spectroscopy, Vaterlaus *et al.* observed the evolution of magnetization of Gd after the action of a 10 ns laser pulse. Using 30 ps probe pulses, they showed that the spin relaxation in gadolinium took place within 100±80 ps [79]. Based on these studies, it was generally believed that the characteristic time of interaction between light and magnetization is similar to that of spin-lattice, which is on nanosecond time scale.

With the improvement in semiconductor technology, the generation of femtosecond laser pulse became possible. In 1996, Beaurepaire *et al*. reported similar results via the time-resolved magneto-optical Kerr effect. They found that a 60 fs laser pulse resulted in a significant demagnetization of a Ni film [80]. Surprisingly, the demagnetization time of Ni films is only about 1ps, as shown in Figure 1-21. Afterwards, many research groups obtained similar results in various materials such as Fe and Co. Ultrafast demagnetization was confirmed to be a universal effect.

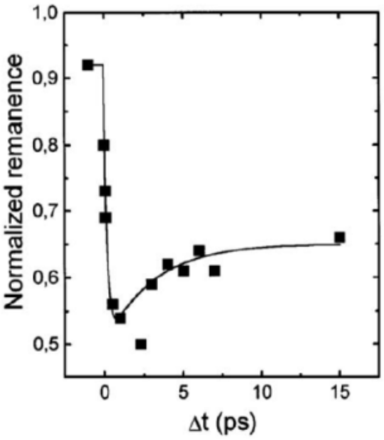

Fig. 1-21 Ultra-fast demagnetization of Ni film induced by a 60 fs laser pulse. Extracted from [80].

The ultrafast magnetization dynamics can be well explained via the phenomenological three-temperature model [80]. According to this model, a spin system possesses three mutually coupled thermal baths: electrons, lattice, and spin, as depicted in Fig. 1-22(a). The temporal evolution of temperature of these three baths can be described by three coupled differential equations:

$$\begin{aligned} C_e \frac{dT_e}{dt} &= -G_{ep}(T_e - T_p) - G_{es}(T_e - T_s) + P(t), \\ C_p \frac{dT_p}{dt} &= -G_{ep}(T_p - T_e) - G_{ps}(T_p - T_s), \\ C_e \frac{dT_s}{dt} &= -G_{es}(T_s - T_e) - G_{ep}(T_s - T_p), \end{aligned} \tag{1.14}$$

where P (t) represents the energy that the laser pulse brings to the entire system. C_e and C_p are the specific heat capacities of electrons and lattices, respectively, G_{ep}, G_{es} and G_{ps} are the electron-lattice, electron-spin, and lattice-spin coupling constant.

These three thermal baths have different heat capacities. Consequently, the temporal evolution of temperature of these three baths differs significantly. The heat capacity of electrons is typically one to two orders of magnitude smaller than that of lattice, thus a ultrafast laser pulse first results in a sharp rise of electron temperature which could be several thousand Kelvin. Then the heat will be transferred from the electrons to the lattice and spin until the thermal equilibrium is reached.

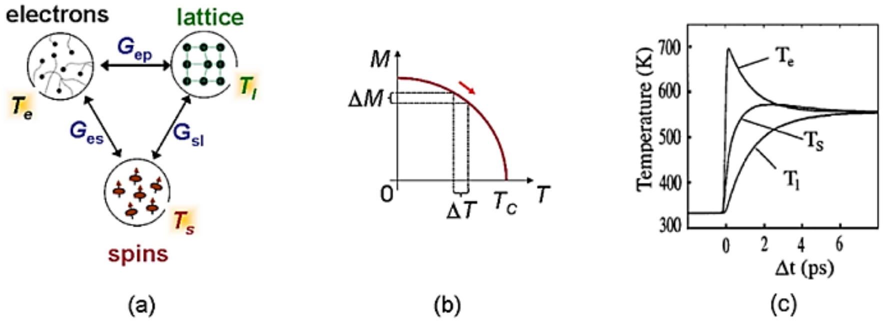

Figure 1-22 (a) Schematic representation of three temperature model. (b) Magnetization as a function of spin temperature. (c) Temporal evolution of electron, lattice and spin temperature calculated from three temperature model. Extracted from [81].

It is worth noting that the spin temperature is derived from M_S (T_S). As shown in Figure 1-22(b), the magnetization monotonically decreases with the increase of spin temperature. Figure 1-22(c) shows the typical temporal evolution of temperature of these three sub-systems.

As mentioned above, the writing speed is a crucial parameter for memory devices. The discovery of ultrafast laser-induced demagnetization triggered the new field of ultrafast manipulation of magnetization which has attracted increasing attention of industry community.

1.2.2 All-optical helicity-independent switching

To date, all-optical magnetization switching has been observed in a large variety of materials such as ferromagnets, ferrimagnets and multilayers [10-15, 81-85]. Moreover, two different types of AOS have been identified. The first one is All-Optical Helicity-Independent Switching (AO-HIS) in which case one laser pulse is enough to reverse the magnetization. However, AO-HIS is mostly observed in

Gd-based materials. For most other materials, it requires multiple pulses to obtain complete reversal, named All-Optical Helicity-Dependent Switching (AO-HDS). The final magnetization state in this case is determined by the laser helicity. In this part, we will give a brief review of AO-HIS and discuss its underlying mechanism.

The first observation of AO-HIS was reported by Radu *et al*. in 2011[10]. They found that a single 60-fs linearly polarized laser pulse resulted in the reversal of magnetization of GdFeCo. With element-specific X-ray magnetic circular dichroism (XMCD) technique, they present the temporal evolution of magnetization of Gd and Fe after the action of one laser pulse. As shown in Figure 1-23(a) and (b), the switching process of GdFeCo can be divided into two stages. First, the magnetizations of both sublattices rapidly decrease with different demagnetization rate. The Gd magnetic moment is quenched within 1.5 ps, while the moment of Fe sublattice is reduced to 0 within 400 fs. Second, the magnetizations of both sublattices switch their directions and recover slowly. Surprisingly, it is seen that the Gd and Fe magnetic moments are aligned in parallel between 400 fs and 2 ps, indicating the formation of a ferromagnetic-like state [schematically shown in Figure 1-23(c)].

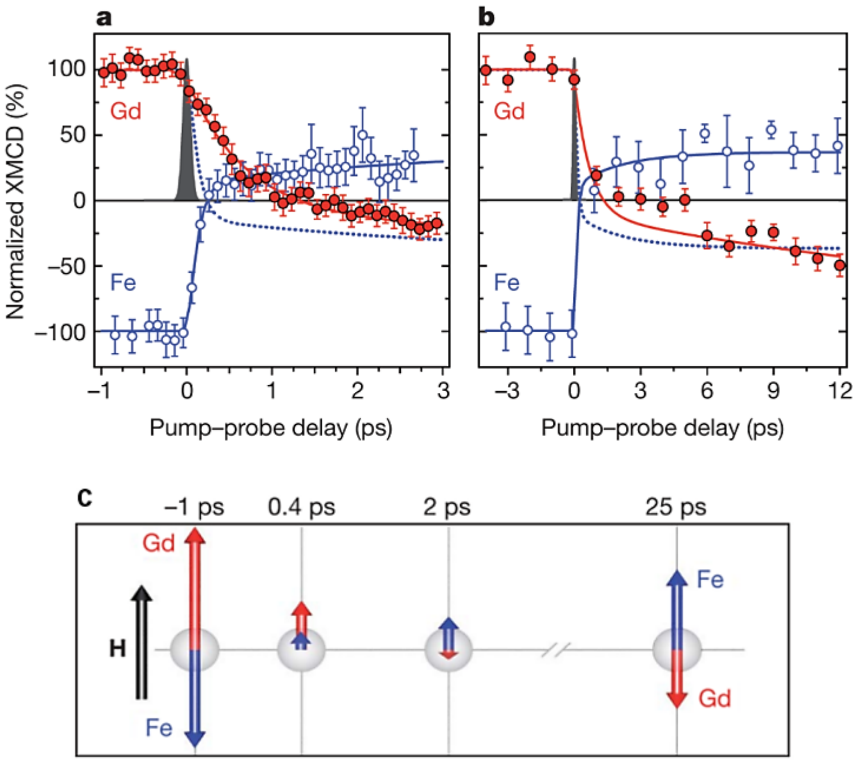

Figure 1-23 Element-resolved dynamics of the Fe and Gd magnetic moments measured by time-resolved XMCD. (a) Transient dynamics of the Fe (open circles) and Gd (filled circles) magnetic moments measured within the first 3 ps. (b) Evolution of Gd and Fe magnetic moments on a 12 ps timescale. (c) Schematic illustration of temporal evolution of Gd and Fe magnetization. Extracted from [10].

To gain a deep insight into its underlying mechanism, the authors also performed simulations based on atomistic spin model which combines atomic LLG formula with Langevin dynamics. As displayed in Figure 1-24, the simulated dynamics of Gd and Fe well reproduce the main features of experimental results. It is worth noting that the laser energy in atomistic model is considered a purely thermal input. The authors made a hypothesis that heat is the only driving force for AO-HIS in GdFeCo.

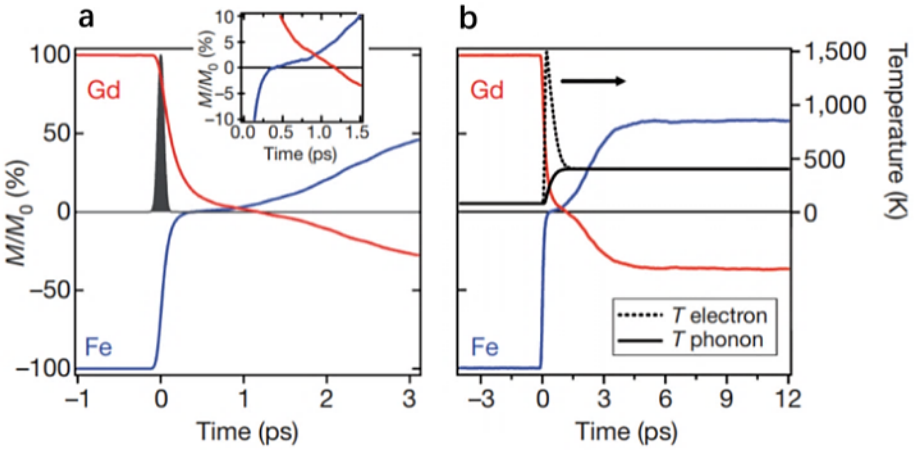

Figure 1-24 Temporal evolution of magnetization of Gd and Fe sublattice obtained based on atomistic spin model. Calculated dynamics are shown for first 3 ps (a) and 12 ps (b). The transient ferromagnetic state can be identified in inset. Extracted from [10].

One year later, T.A. Ostler *et al*. reported similar results in $Gd_{24}Fe_{66.5}Co_{9.5}$ [11]. As shown in Figure 1-25, One 100 fs linearly polarized laser pulse is enough to trigger the magnetization reversal of $Gd_{24}Fe_{66.5}Co_{9.5}$.

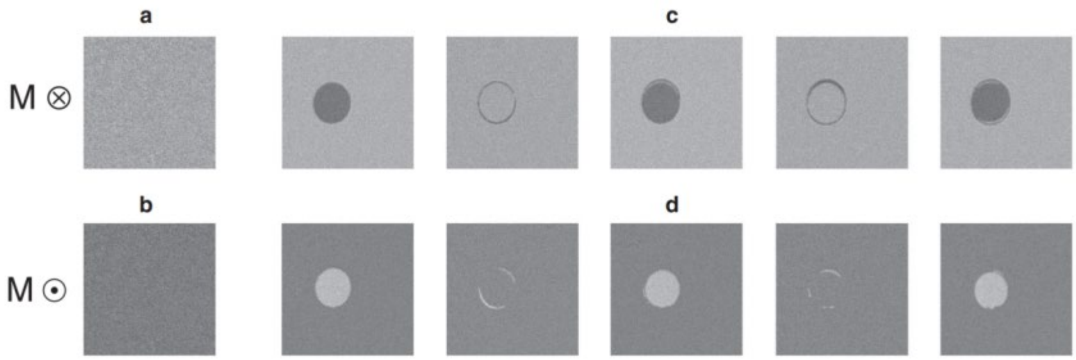

Figure 1-25 The magneto-optical images of $Gd_{24}Fe_{66.5}Co_{9.5}$ taken after the action of 100fs laser pulses. Extracted from [11].

Furthermore, to confirm that the ultrafast heating is a sufficient stimulus for magnetization switching in GdFeCo, they prepared arrays of 2 μm diameter disks of $Gd_{25}Fe_{65.6}Co_{9.4}$. The size is much smaller than that of beam spot size which is about 30 × 100 μm. As a consequence, several disks can be excited by the laser pulse at the same time. The magnetic response of these disks can be observed within the same field of view of the microscope. The distance between centers of two neighboring disks is twice the size of their diameter, which can significantly reduce the effect of dipolar interaction.

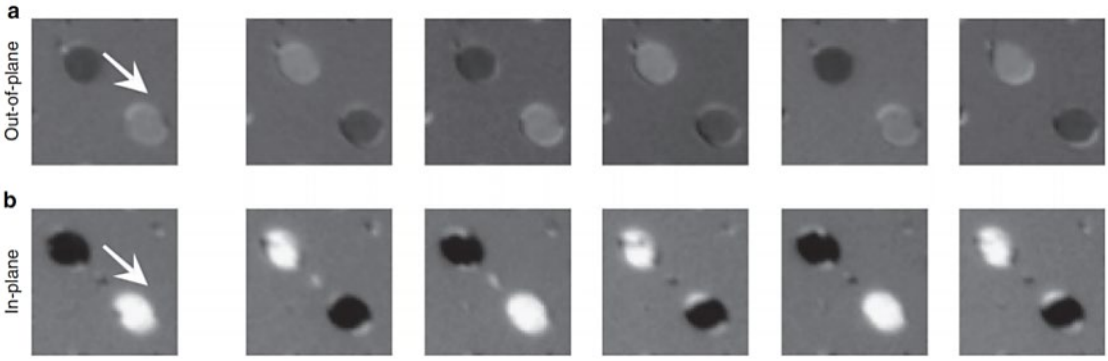

Figure 1-26 XMCD images of 2 μm diameter $Gd_{25}Fe_{65.6}Co_{9.4}$ disks with (a) perpendicular magnetic anisotropy and (b) in-plane magnetic anisotropy. The spot size of laser beam is about 30×100 μm which is much larger than that of GdFeCo disk. the dark grey and light grey correspond to magnetization up and down, respectively. Extracted from [11].

Figure 1-26 shows XMCD images taken before and after the action of laser pulses, the dark grey and light grey correspond to magnetization up and down, respectively. It is seen that a single linearly polarized laser pulse can still induce the deterministic magnetization reversal for disks with perpendicular (a) and in-plane anisotropy (b). Consequently, the authors concluded that the stray fields or domain walls surrounding the illuminated area have no effect on the AO-HIS.

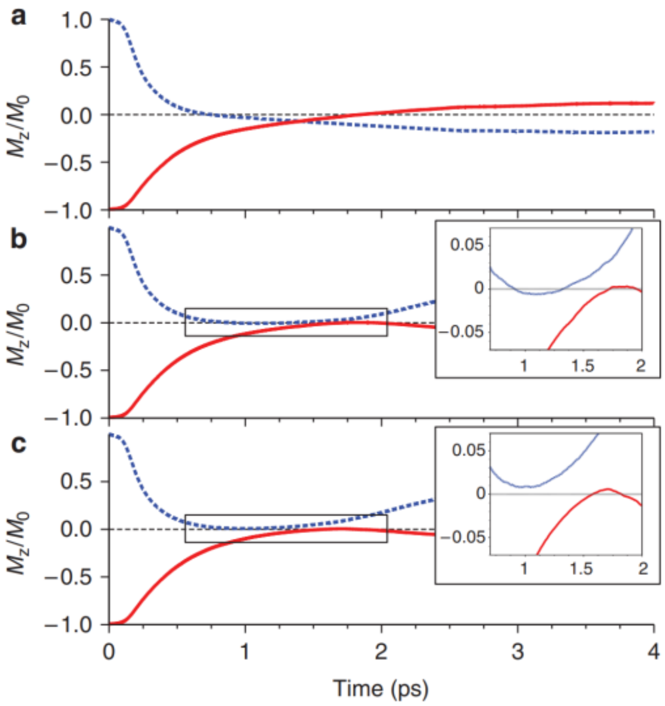

Figure 1-27 Temporal evolution of z component of magnetization of Gd and Fe sublattice under 10 (a), 40 (b) and 50T (c). The applied magnetic field aims to prevent the magnetization switching of Fe sublattice. Extracted from [11].

To further understand the role of transient ferromagnetic state, the authors performed calculations based on atomistic spin model shown in Figure 1-27. Different from what Radu did, a magnetic field is applied on Fe sublattice to prevent its magnetization reversal. However, as displayed in Figure 1-27 (b), the transient ferromagnetic state still occurs when the magnetic field reaches to 40 T. Based on these results, they proposed a novel switching mechanism in ferrimagnets. The scenario can be described as follows. The electron temperature of GdFeCo first rapidly increases to Curie temperature T_c after irradiation of one ultrashort laser pulse. Afterwards, the two sublattices demagnetize at different rates and the magnetization of Fe sublattice first reaches zero, resulting in the presence of transient ferromagnetic state. Then the magnetization of Fe sublattice grows in the opposite direction at the expense of that of Gd due to the exchange interaction. Finally, the antiferromagnetic exchange induces the overall switching of both sublattices.

These works suggest that ultrafast heating of the electronic system is the driving force for AOS in Gd-based ferrimagnetic materials. Inspired by this, in 2017, Yang et al. used picosecond charge current pulses to excite the conduction electrons of a GdFeCo metal film [60]. They observed deterministic, repeatable ultrafast reversal of the magnetization of GdFeCo. To exclude the effect of SOT coming from the buffer layer and caaping layer, they also performed simulations with LLG equation. The results show that the maximum change in the out-ofplane component of the magnetization due to SOT is less than 10%. From these calculations, they concluded that the toggling behavior of the GdFeCo magnetization is principally due to ultrafast heating of the electronic system and driven by physics similar to that responsible for AO-HIS.

1.2.3 All-optical helicity-dependent switching

In 2014, a breakthrough was made by Lambert *et al.*[86] They demonstrated evidence of AO-HDS in ferromagnetic materials such as Co/Pt, Co/Ni, Co/Pd and $Co_{1-x}Ni_x$/Pt multilayers, which makes AOS a more general phenomenon. In the experiment, both sweeping and static laser beam are used.

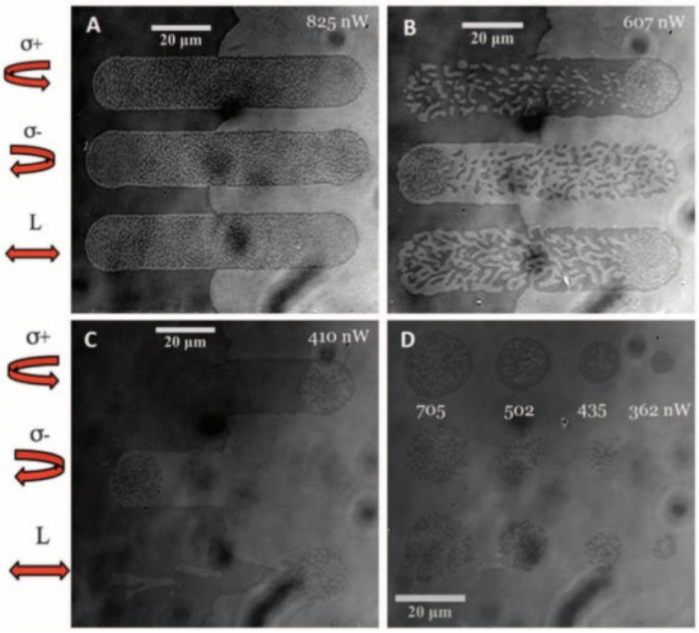

Figure 1-28 Magneto-optical images taken for $[Co/Pt]_N$ after action of sweeping laser beam with different polarizations. (a) N=8 repeats (b) N=5 repeats (c) N=3 repeats (d) Magneto-optical images taken for $[Co/Pt]_{x3}$ after exposure to static laser pulses with various pulse fluences. The repetition rate of laser pulses is 1 kHz. Extracted from [86].

With the magneto-optical microscope, they first studied the effect of ultra-short laser pulses on $[Co(0.4nm)/Pt(0.7nm)]_n$ film. Figure 1-28 shows the magneto-optical images taken for samples with repetition number N=8 (a), 5 (b) and 3 (c). It can be seen that when N=8 and 5, the sweeping laser beam only leads to a thermal-induced multidomain state, regardless of the helicity. However, complete magnetization reversal is achieved when N=3. In addition, the left and right circularly polarized light switch the magnetization to up and down, respectively. Then, they studied the effect of static laser pulses on $[Co/Pt]_3$. As shown in Figure 1-28 (d), a laser power of 362 nW induces a full magnetization reversal, although the switching domain is very small. As the fluence increases, multi-domain state is observed in the center of beam spot, indicating the occurrence of demagnetization. These results clearly indicate that AOS is not exclusive to ferrimagnets. Thus, the presence of antiferromagnetically coupled sublattices is not a necessary condition, which cHallenge the model proposed by previous work.

In 2017, Medapalli *et al.* studied the process of AO-HDS in Co/Pt using time-resolved magneto-optical imaging technique [87]. Figure 1-29 shows the magneto-optical images for $[Co(0.4\ nm)/Pt(0.7\ nm)]_{x3}$ taken at different exposure time. The repetition rate of applied consecutive laser pulses is 1 kHz. It is seen that as the exposure time increases, the right circularly polarized light first induces the nucleation of domain in the center of beam spot. Afterwards, the switching domain grows slowly until a complete reversal is achieved. Nevertheless, the left circularly polarized light only leads to a random nucleation regardless of the exposure time. These images provide clear evidence that the AO-HDS is mediated by the nucleation and propagation of magnetic domains. Thus, it is a cumulative process which is different from the case of AO-HIS in ferrimagnets.

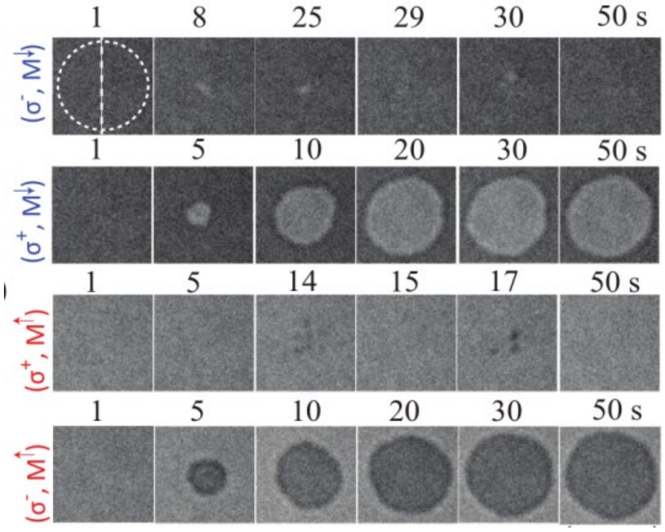

Figure 1-29 Magneto-optical images taken for different combinations (б±, M↑↓) at different exposure time. Extracted from [87].

Meanwhile, with the aid of time-resolved electrical measurement, El Hadri *et al*. studied the detailed process of AO-HDS in Co/Pt multilayers [88]. They prepared a 15μm-wide Hall cross as displayed in Figure 1-30,. In this experiment, the laser beam is kept static and about 40 μm away from the center of Hall cross. That is because the laser intensity follows the Guassian distribution, meaning that the center of the laser beam possesses much higher intensity then that at outer area, which can easily induce the thermal-induced demagnetization.

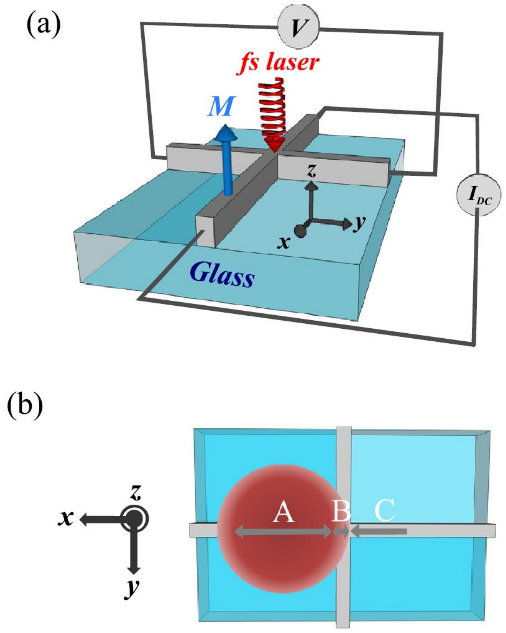

Figure 1-30 (a) Schematic view of investigated 15 µm-wide Co (0.6 nm)/Pt (0.7 nm) Hall cross. The Hall voltage is measured and recorded by a oscilloscope with a sampling rate of 1 M/s (b) Schematic showing the position of laser beam spot which is 40µm from the center of Hall cross, The FHWM of the laser beam spot is about 60 µm. Extracted from [88].

Figure 1-31 shows the temporal evolution of Hall resistance V_{Hall} under the action of 600 consecutive laser pulses for different polarities. Surprisingly, the change of V_{Hall} exhibits clear two-stage characteristic. First, V_{Hall} rapidly decreases to 0 within several laser pulses, indicating a formation of multidomain state. Afterwards, the evolutions of V_{Hall} diverge for different polarities. For linear light, V_{Hall} remains around 0 (green lines). In the cases of left and right circularly polarized light (blue and red line), V_{Hall} gradually increases, indicating the occurrence of remagnetization.

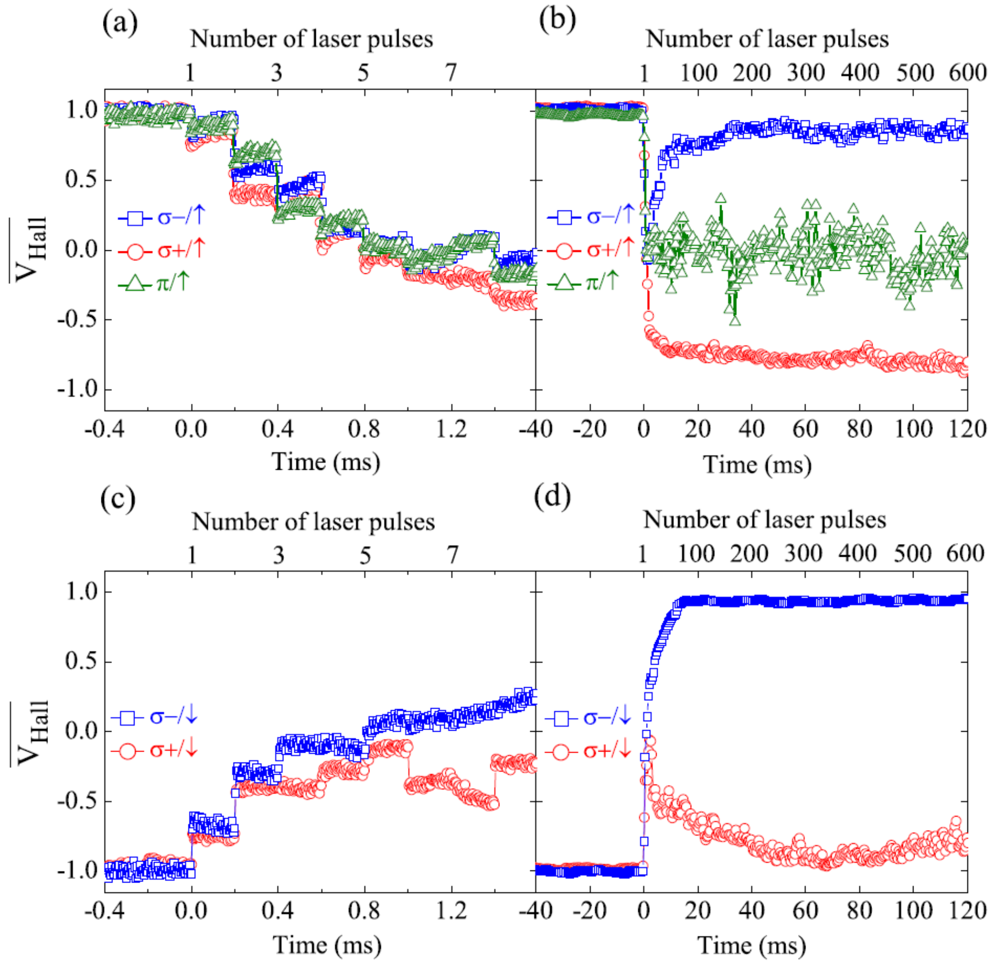

Figure 1-31 (a) and (b) Temporal evolution of Hall voltage V_{Hall} of Co/Pt Hall cross which is initially saturated up, after exposure to 600 consecutive laser pulses with different polarizations. (c) and (d) The same behavior is measured as (a) and (b) with initial saturation of the Hall cross down. Extracted from [88].

These results clear indicate that AO-HDS is a cumulative process which is governed by domain nucleation and propagation. But what role does the helicity play in AO-HDS? The authors proposed a scenario in which the driving force for domain wall motion comes from two important effects, that is, the magnetic circular dichroism (MCD) and the Inverse Faraday Effect (IFE). The MCD effect first leads to a temperature gradient across the domain wall due to the different absorption of the pulse energy for two circular helicities. Then such temperature gradient possibly induces a spin current via the spin seebeck effect (SSE), which results in the deterministic domain wall motion. The IFE is another possible driving force which works by directly generating magnetic field on spins.

2 Research methods

In this chapter, I will first introduce the research tools I used to prepare devices and analyze the results. Secondly, I will describe the atomistic modeling which has become a useful theoretical tool in understanding the behavior of magnetic materials.

2.1 Experimental tools

2.1.1 Sample deposition and fabrication

Magnetron sputtering

Magnetron sputtering is a conventional and useful method of Physical Vapor Deposition (PVD), which can be used to prepare thin films of metals, semiconductors and insulators. Figure 2-1 shows the schematic of magnetron sputtering process. The material target is placed on the cathode while the substrate is placed on the anode. To create plasma, a high voltage in the order of 1kV or more is applied between the electrodes. Usually the anode is grounded and the negative voltage is applied to the cathode. The sputtering process can be divided into two stages. First, upon the application of electric field, electrons rapidly move in the chamber and collide with Ar atoms, which generate Ar^+ ions and electrons. Second, the newly created Ar^+ ions move towards to the target and bombard the surface of target material, which result in the ejection of target atoms. These ejected atoms then condense on the wafer thereby forming the desired thin film. To improve the sputtering efficiency, a magnetic field is applied in the cathode to trap the electrons, which increases the probability of collision between electrons and the Ar atoms. The main advantage of sputtering is its relative simplicity. However, it suffers from two main limitations. Firstly, the plasma is present in the entire space between the electrodes, which has the consequence that this space is filled with electrons which are repulsed by the negative cathode and collide on the substrate. As a result, the substrate substantially heats up during sputtering process and the efficient cooling is required. Secondly, the plasma is unstable, so a tiny fluctuation of sputtering energy cannot be avoided, which can lead to a small variation of the sample composition even with the same sputtering parameters

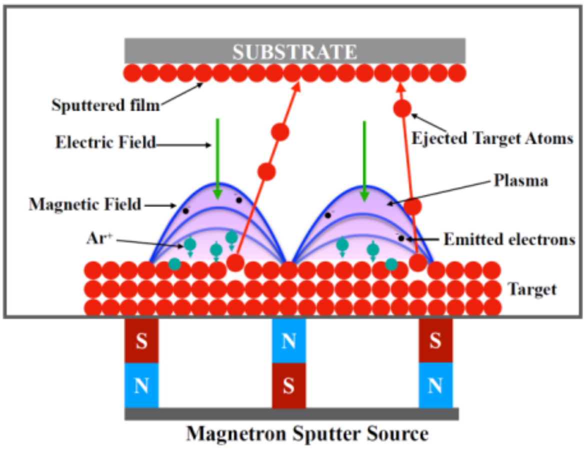

Figure 2-1 Schematic of magnetron sputtering process. Extracted from [89].

In this thesis, all the samples were grown by Magnetron sputtering with an Orion system from AJA International. We use argon gas with a flow rate of 50 sccm. During deposition, the main chamber was maintained at high vacuum (about 5×10^{-8} Torr). All the samples were deposited at room temperature.

Optical lithography

The key fabrication processes of the devices studied in this thesis are lithography and etching. I used ultraviolet lithography (UVL) and E-beam lithography (EBL) to fabricate micro-sized and nano-sized structures on the photoresist, respectively. Ion beam etching (IBE) technique is used to transfer the pattern from photoresist to thin films.

(1) UVL

There are two main approaches in light-based lithography. One is the serial writing using a scanning laser beam on the substrate referred to as "direct laser writing". The other approach consists of exposing the substrate through a mask. The exposure duration for the "direct laser writing" will heavily depend on the area to be exposed, while the exposure through a mask takes a short time. In this thesis, the latter method is used.

Lithography has two major steps. First is spin coating. Spin coating is a common technique for applying photoresist to substrates. When the photoresist is spun at high speeds, the centripetal force and the surface tension of the liquid together create an even covering. The thickness of photoresist after spin coating ranges from a few nanometres to a few microns which depends on the rotation rate and duration [90-100]. Figure 2-2 shows the spin coater used in this thesis. There is a rotatable sample holder in the center.

Figure 2-2 SPIN150 used for spin coating

The second step is exposure. The goal of this step is to transfer the pattern from mask to photoresist. The area exposed to light of a specific wavelength undergoes a change in chemical properties which could be then removed by developer, while the area shaded by mask is hard to be dissolved by developer [101-106]. As a consequence, the photoresist is shaped into the same structure as the pattern of mask. For UV lithography the wavelength is typically in the near ultraviolet regime of 300-400 nm. Figure 2-3 shows the UV machine used in this thesis.

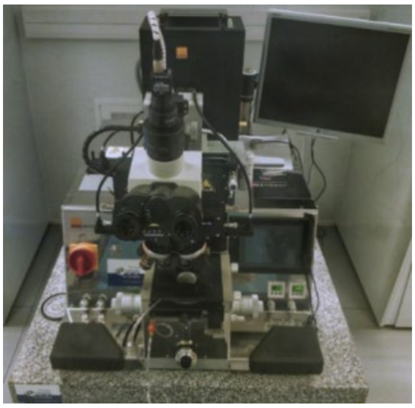

Figure 2-3 UV lithography machine (MA6, SUSS, Germany).

(2) EBL

Electron beam lithography (EBL) is an advanced technique to create the extremely fine patterns which are commonly used for microfabrication. Different from UV lithography, the resist used for EBL is sensitive to electrons. Thus a highly focused beam of electrons is used to write patterns. EBL is therefore a direct write serial technique, similar to laser writing that we discussed above.

The schematic diagram of EBL is presented in Figure 2-4. The electrons are first extracted from the gun and then accelerated towards a series of electron lenses that will focus and correct aberrations in order to obtain the smallest electron beam. A magnetic lens is formed from two circularly symmetric iron or some other high permeability materials, pole pieces, with a copper winding in between. Additional features include beam blanker and beam deflectors. Beam deflectors are introduced to scan the electron beam over the target. The electron beam may be deflected over a range of typically from a few tens of micrometers up to a millimeter. Writing a large area requires that the stage is physically moved to reach a neighboring region and ultimately to write the entire sample surface. This writing region is called a field and divided into many subfields. The main fields correspond to the maximum beam deflection range. Samples are loaded and unloaded into the system via a vacuum loadlock. E-beam lithography requires a high vacuum chamber so that the electron can freely travel from the electron gun to the samples. The main features of EBL are listed as follows.

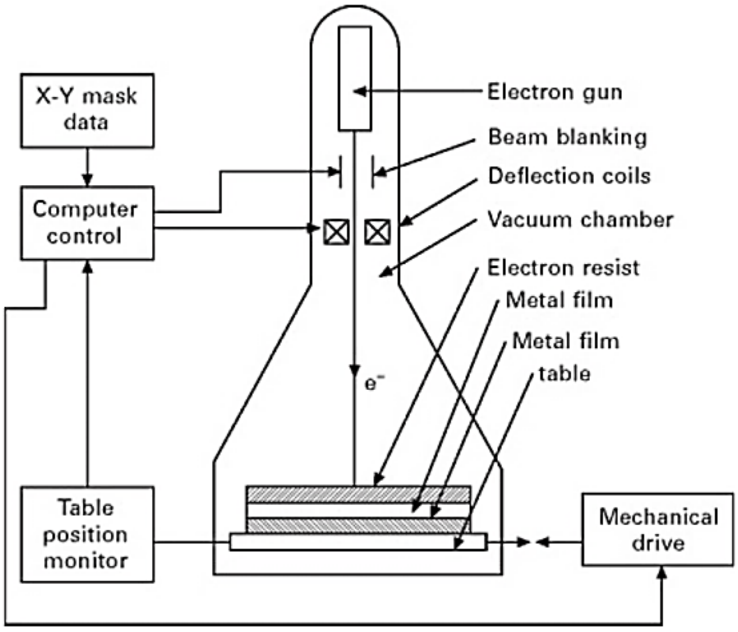

Figure 2-4 Schematic diagram of EBL. Extracted from [107].

1. It allows the creation of complex nanopatterns on resist.
2. The process is time consuming, which is much slower than UV lithography.
3. It doesn't require a real mask, the pattern is designed using related computer program.
4. The EBL machine is more expensive and complicated than UV machine.

The resolution or feature size that is achievable using this e-beam process is limited to around a few nanometers (~10 nm).

Figure 2-5 Electron beam lithography (Raith)

IBE

Ion Beam Etching (IBE) technology allows films to be etched by the use of beams of charged ions in a high vacuum system. During the etching process, the area protected by resist is not etched, while the area without a covering of resist is eroded. Consequently, the pattern is transferred from the resist to materials. The main etching mechanism of an ion beam is physical sputtering due to the high kinetic energy of the ions. The IBE works at a low pressure which results in a large mean free path and little re-deposition of material that is etched away from substrate.

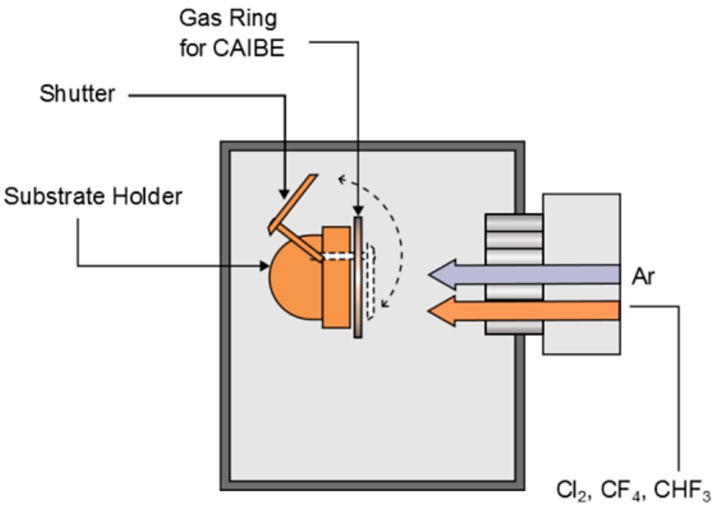

Figure 2-6 Schematic of Ion beam etching system. Extracted from [108].

Figure 2-5 shows the IBE system used in this thesis. Inside such a system, it is possible to vary the angle of incidence of the ion beam onto the samples. In addition, an analytical and secondary ion mass spectroscopy equipment is incorporated to probe the evolution of the etching.

2.1.2 Kerr imaging set-up

This thesis consists of the studies on STNOs and AOS. For the former, the electrical methods are used to analyze their performance. For the latter, we mainly use Kerr imaging set-up to observe the magnetization state of tested thin films after exposure to laser pulses with different parameters.

The Kerr imaging set-up mainly consists of three parts: the laser beam, the probe and the imaging part. Before reaching the sample surface, the laser beam goes through several optics, namely a Glan-Taylor polarizer, a half-wave plate, a quarter-wave plate and a convex lens. The Glan-Taylor polarizer linearly polarize the laser. The half-wave plate results in a phase shift of π/2 which allows us to vary the laser power continuously. In order to obtain circularly polarized light, the quarter-wave plate is placed after half-wave plate. The convex lens focuses the laser beam onto the sample surface. Moreover, the beam spot size can be tuned by changing the position of convex lens. With the Pulse Picker, the number and the repetition rate of laser pulses can be well controlled. The magnetic response of thin films to ultra-short laser pulses is probed via a probe light and a pair of polarizer-analyzer which are arranged in Kerr configuration. Lastly, the magnetic domains are imaged with a CCD camera that provides an image of 2448 × 2048 pixels. An IR filter is added to protect the camera from the direct exposure to laser pulses and allows the probe light to go through in the meanwhile.

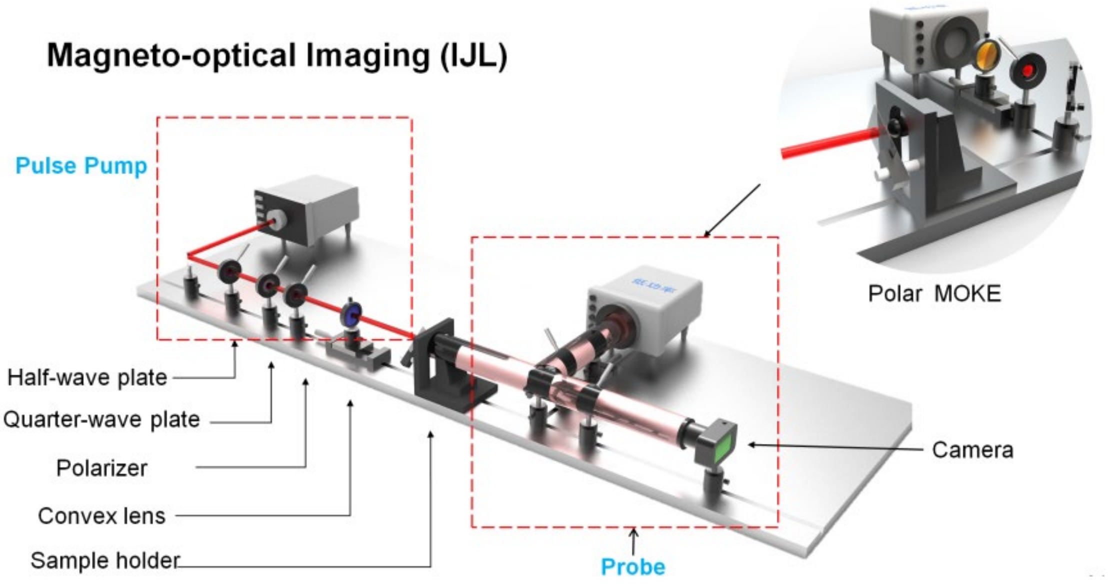

Figure 2-7 Kerr imaging set-up used for observation of magnetic configuration of thin flims.

2.1.3 Electrical characterization

In this thesis, the performance of STNO is measured by an electrical method. Figure 2-8 shows the schematic of the experimental set-up. The main parts of this set-up include a spectrum analyzer, a nano-voltmeter, a DC current source and a Bias Tee. The STNO is connected to the DC source via ground-signal-ground (GSG) probe. We measure the static transport properties at room temperature under a constant DC current of 10μA. A Rohde & Schwarz spectrum analyzer is used to characterize the power spectrum density of STNO output. The Bias Tee is a three-terminal device consisting of an inductor and a capacitor, which is used to extract the AC component of the STNO output. As mentioned above, once I_{DC} reaches a certain value, the damping torque in free layer is completely offset by STT exerted by the polarized spin current, leading to a steady magnetization precession and thus a high-frequency

AC output. It is important to note that the output power scales with the precession angle θ (marked in Fig 1-7). Output signals were recorded after 40 dB amplification and the background noise, measured at zero dc current, was subtracted from the power spectra. All the RF measurements were performed at room temperature with a projected field electromagnet that allows us to control the field angle continuously.

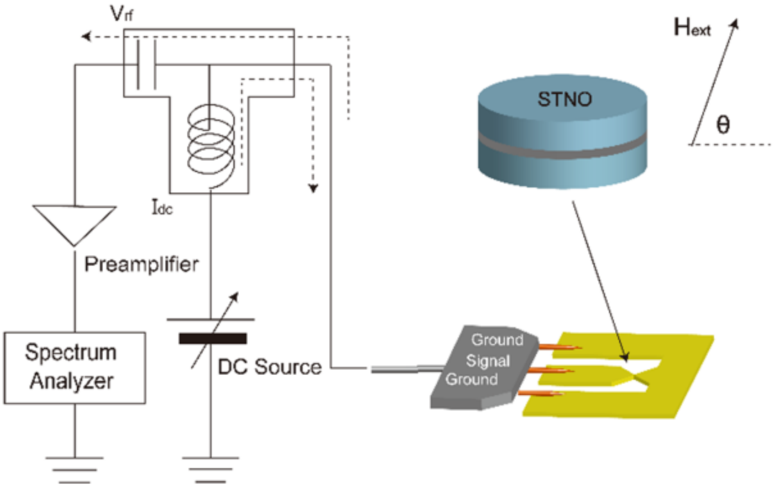

Figure 2-8 Schemes of the experimental setup and the sample geometry. Main parts of the setup: electromagnet, spectrum analyzer, nanovoltmeter, current source. Extracted from [109].

2.2 Atomistic modeling

Atomistic LLG equation

The physical basis of the atomistic spin model is the localization of unpaired electrons to atomic sites, leading to an effective local atomistic magnetic moment [110]. In this model, the energy of a magnetic system is described by the Hamiltonian given by:

$$H = -\frac{1}{2}\sum_{i\neq j} J_{ij}\boldsymbol{S_i}\cdot\boldsymbol{S_j} - \sum_{i} k_u \boldsymbol{S}_{\boldsymbol{z}}^2 \tag{2.1}$$

where J_{ij} is the exchange value between spin i and j (i, j are lattice sites); For ferromagnets, the magnetic moments align in parallel and $J_{ij} > 0$; for antiferromagnets, the magnetic moments tend to align in antiparallel, where $J_{ij} < 0$. S_i is the normalized spin vector and k_u is the local uniaxial anisotropy constant per atom.

As mentioned above, the magnetization dynamics in a thin magnetic film is typically described by the Landau-Lifshitz-Gilbert (LLG) equation:

$$\frac{\mathrm{d}\boldsymbol{m}}{dt} = -\gamma[\boldsymbol{m} \times \mathbf{H} + a\boldsymbol{m} \times (\boldsymbol{m} \times \mathbf{H})] \tag{2.2}$$

At the atomistic level, the LLG equation can be presented by [111]:

$$\frac{\partial \boldsymbol{S_i}}{\partial t} = -\frac{\gamma}{(1+\lambda^2)}\left[\boldsymbol{S_i} \times \boldsymbol{H_{eff}^i} + \lambda \boldsymbol{S_i} \times \left(\boldsymbol{S_i} \times \boldsymbol{H_{eff}^i}\right)\right] \tag{2.3}$$

where S_i is a unit vector representing the direction of the magnetic spin moment of site i, γ is the gyromagnetic ratio and $H_{eff}^i$is the net magnetic field on each spin. λ is the damping constant. It's worth noting that the damping constant has different definitions in these two forms of LLG [111]. In the macroscopic LLG, the damping constant indicated by α includes all contributions, both intrinsic (such as spin–lattice and spin–electron interactions) and extrinsic (spin-spin interactions arising from demagnetization fields, surface defects [112], doping [113] and temperature [114]), while the λ in atomistic LLG only includes the local intrinsic contributions.

Langevin dynamics

The standard LLG equation is only applicable to simulations at zero temperature. To study the thermal effects induced by ultra-short laser pulses, the atomistic model is combined with Langevin dynamics. Then, the net magnetic field in this case is given by $H_i = -\partial H_i/\partial S_i + \eta_i$, where η_i represents the fluctuations coming from thermal effects and is coupled to T_e. Noting that the increase of T_e represents an energy input from laser heating. In order to model the laser heating of the sample, the two-temperature model (2TM) is used [115]:

$$C_e\frac{dT_e(t)}{dt} = -G\left[T_e(t) - T_{\mathrm{ph}}(t)\right] + P(t)$$

$$C_p\frac{dT_p(t)}{dt} = G\left[T_e(t) - T_{\mathrm{ph}}(t)\right]$$

$$,\ P(t) = P_0 e^{-(t/\tau_\pi)^2} \tag{2.4}$$

where T_e is the electronic temperature, T_{ph} is the temperature assigned to the phonon bath, $C_e = \gamma T_e$ and C_p are the heat capacities for electrons and phonons, and G is a coupling parameter between these systems. At last, by means of time integration of the LLG equation, we can obtain the temporal evolution of a system of spins for different pulse energy.

3 Magnetization dynamics in in-plane Spin Nano-oscillators

3.1 Introduction

Initially most of the research studies were focused on in-plane STNOs [116-123], in which the free and fixed FM layers exhibit intrinsic easy-plane anisotropy—meaning that the magnetic moments in equilibrium state lie in the plane of the film if no external magnetic field is applied. Co, $Co_{90}Fe_{10}$ and NiFe are commonly used materials exhibiting easy-plane magnetization anisotropy.

In this chapter, I will present my study on the magnetization dynamics in a CoFeB-based in-plane MTJ under different magnetic field and current, so as to find the optimal conditions of in-plane STNOs for FSK or ASK. In addition, we propose a new RF modulation method by combing STNO with memristor (Memristor-controlled Spin Nano-oscillators, MSNs), which shows promise for amplitude and frequency modulation.

3.2 Samples and measurement set-up

We fabricated multilayer MTJ stacks with PtMn (15) / $Co_{70}Fe_{30}$ (2.5) /Ru (0.85) / $Co_{40}Fe_{40}B_{20}$ (2.4) / MgO (0.8) / $Co_{60}Fe_{20}B_{20}$ (1.8) (thickness in nm) structure using a ultrahigh vacuum Singulus TIMARIS PVD magnetron sputtering system. Subsequently, the films were annealed at 300 ℃ for 2.0 h under a magnetic field of 1 T and then patterned into elliptical pillars by electron beam lithography combined with Ar ion milling technique. The typical dimension is around 150 nm×50nm. The memristor stack consists of Al (500 nm)/TiN (20 nm)/TaO_x (60 nm)/HfO_2 (8 nm)/TiN (20 nm). The conductive metal oxide (TaO_x) not only improves the thermal efficiency but also acts as an inbuilt current compliance layer. Through atomic layer deposition (ALD) a HfO_2 switching layer was deposited first. Subsequently, a TaO_x layer was deposited by physical vapor deposition method. Following this, a 20 nm TiN top electrode and 500 nm Al pad were deposited by sputtering and electron beam evaporation. Finally, the top Al pad was patterned by dry etching with Cl_2/BCl_3 plasma.

All measurements are performed at room temperature, with an in-plane magnetic field applied using a projected field electromagnet that allows us to control the field angle continuously. At each current value, microwave measurements up to 8.0 GHz were recorded on a Rohde & Schwarz spectrum analyzer after 40 dB amplification. The background noise, measured at zero dc current, was subtracted from the power spectra. Electrical characterization of memristors are implemented via an Agilent B1500A semiconductor parameter analyzer and a Cascade Microtech probe station.

Figure 3-1 shows the measurement set-up used in this work. In order to connect an STNO and a memristor together, I designed a PCB board as a holder for the memristor and insert it into the circuit between T-bias and probe station via SMA connectors.

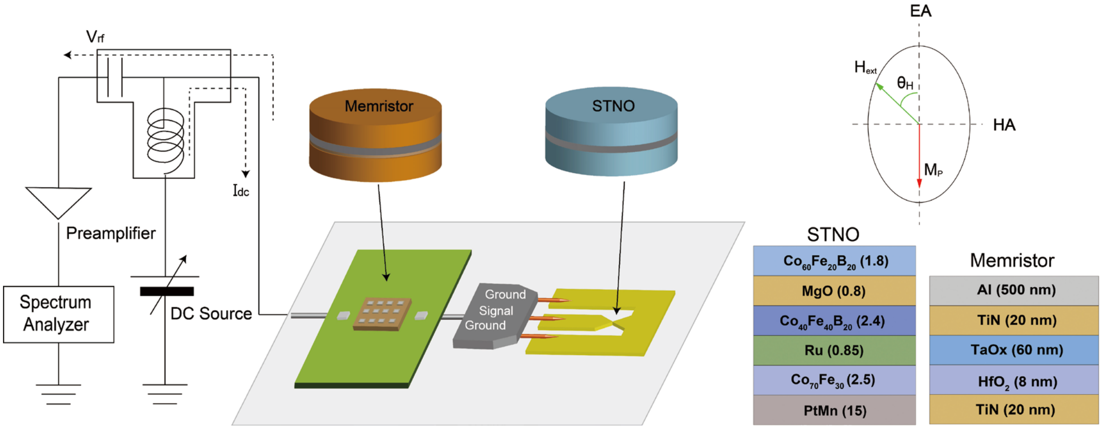

Figure 3-1 Schematic diagram of the new modulation approach realized by MSN. The exciting current for STNO is injected via 1 μm thick ground–signal–ground (GSG) waveguides. The memristor is connected to a high frequency electrical circuit board via wire-bonding and then combined with STNO in series. Sketch of the relationship between directions of the external magnetic field and the pinned layer magnetization (M_p) is also shown here. EA and HA indicate the easy axis and hard axis respectively. Extracted from [124].

PCB holder for memristor

The high frequency PCB board (HF-PCB) was made considering two factors: impedance matching and board design. Impedance is defined as the combined effect of capacitance, inductance, and resistance that a circuit offers a signal at a given frequency. When high-frequency signals are carried on transmission lines of any significant length, care must be taken that the transmission medium is matched to its terminations. The source and load impedances should be as close as possible to the characteristic impedance of the transmission line, as this minimizes signal reflection which causes serious power loss. As for the board design, stripline and microstrip are the two most popular RF/microwave transmission-line formats. Microstrip routing is a transmission line trace routed on an external layer of the board. Because of this, it is separated from a single ground plane by a dielectric material. Stripline and microstrip have different benefits, here, we choose microstrip routing since its transmission delay is smaller which benefits the signal modulation [125-132]. A schematic view of a microstrip PCB and the PCB board we used are shown in Figure 3-2.

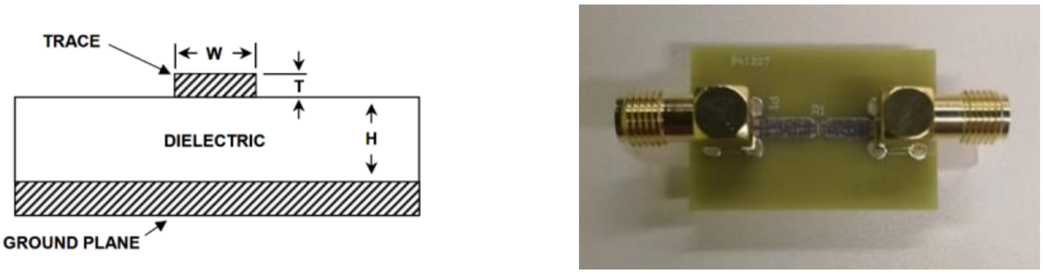

Fig 3-2 A microstrip ransmission line with defined impedance is formed by a PCB trace of appropriate geometry, spaced from a Ground Plane.

Usually, the impedance of transmission line and input impedance of Spectrum Analyzer are 50 Ω, so we should choose proper parameters to decrease the impedance of PCB board. The impedance of microstrip can be expressed by:

$$Z_0 = \frac{\eta_0}{2\pi\sqrt{2}\sqrt{E_r + 1}} ln\left(1 + 4\left(\frac{H}{W_{eff}}\right)(X_1 + X_2)\right) \tag{3.1}$$

where

$$W_{eff} = W + \left(\frac{t}{\pi}\right) ln \left\{ \frac{4e}{\sqrt{\left(\frac{T}{H}\right)^2 + \left(\frac{T}{W_\pi + 1.1T_\pi}\right)^2}} \right\} \frac{E_r + 1}{2E_r}$$

$$X_1 = 4\left(\frac{14E_r + 8}{11E_r}\right)\left(\frac{H}{W_{eff}}\right)$$

$$X_2 = \sqrt{16\left(\frac{H}{W_{eff}}\right)^2 \left(\frac{14E_r + 8}{11E_r}\right)^2 + \left(\frac{E_r + 1}{2E_r}\right)\pi^2}$$

In which T is trace thickness, H is substrate height, W is trace width and E_r is the substrate permittivity. In our case, we use parameters T= 20 µm, H= 1.6 mm, W= 3 mm and E_r=4.2, the calculated impedance is 51.6 Ω.

3.3 Basic Characterization for STNO

We first measured the static transport properties of the studied MTJ. Figure 3-3(a) and (b) display the magnetoresistance curve under external magnetic field applied along easy axis and hard axis, respectively. The bias current $I_{\rm dc}$ = 10 µA. The MTJ device exhibits two resistance states, denoted as R_{AP}≈1836 Ω (antiparallel) and R_P≈1100 Ω (parallel). Therefore, the TMR ratio of the fabricated MTJ devices can be calculated as~67%.

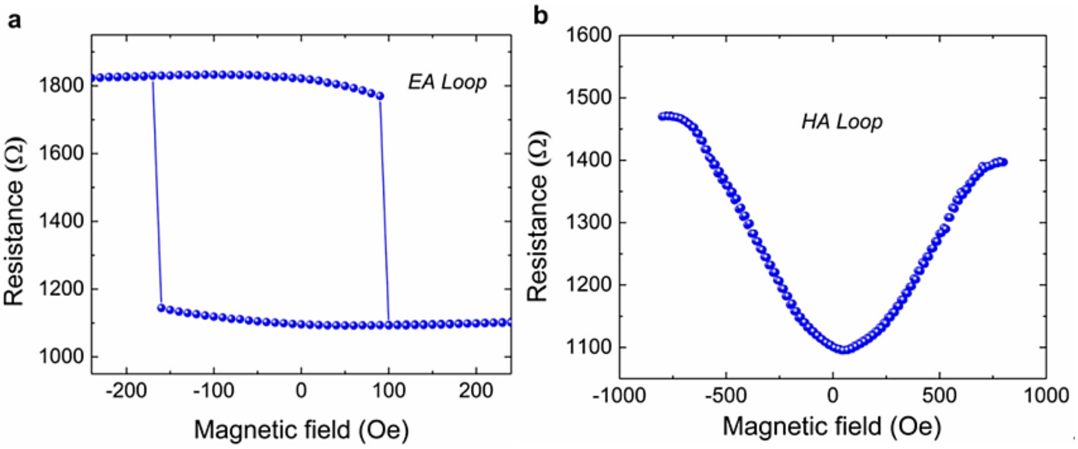

Figure 3-3 MR curves measured with (a) the in-plane easy-axis magnetic field and (b) the hard-axis magnetic field. A bias current of 10 µA was applied.

Next, we focused on the STT-induced magnetization oscillations. The magnetization oscillations of free layer of MTJ can generate two possible outputs: (1) a microwave voltage and (2) high frequency variation of the magnetic field close to the MTJ. The strong local microwave magnetic fields can be used for data recording applications. For instance, in Microwave-Assisted Magnetic Recording (MAMR), a MTJ or Spin valve is introduced to apply a microwave field to the storage medium, which put energy into the magnetization, reducing the threshold of recording magnetic field. Here, we are only interested in voltage and current outputs. As demonstrated in previous work [117], the amplitude of magnetization precession changes with the direction of applied magnetic field because of the angle dependence of STT. To obtain a signal with narrow linewidth, we applied in-plane magnetic field at an angle of approximately 60° off the easy axis. To avoid the breakdown of MTJ, we present our results in the range of 0~0.6 mA.

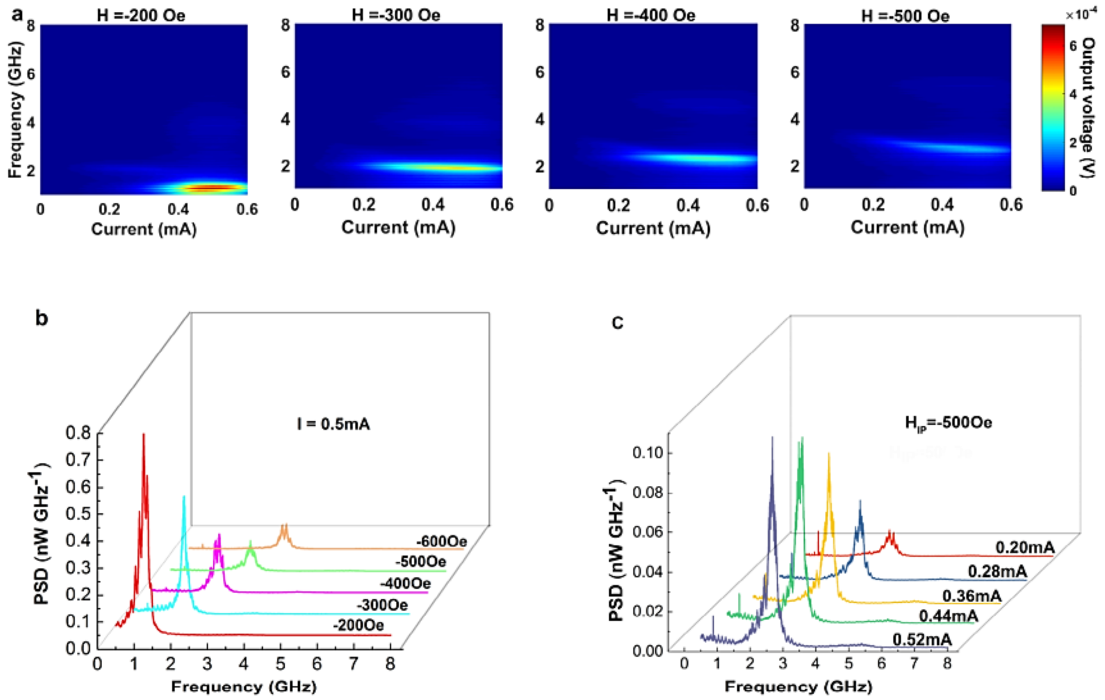

Figure 3-4 Basic Characterization for STNO alone (a) Output voltage measured as a function of exciting current under different magnetic field (b) The power spectrum density as a function of magnetic field under exciting current of 0.5mA. (c) The power spectrum density as a function of exciting current under an in-plane external magnetic field of 500Oe. The direction of the external magnetic field is fixed at an angle of 60° off the hard axis [124].

As is shown in Figure 3-4 (a), where the positive current is defined as electrons flowing from the pinned layer to the free layer, large-power microwave emission can be observed under a range of external magnetic fields and clear single oscillation mode can be identified in each case. Figure 3-4 (b) and (c) show the microwave emission spectra for different currents and magnetic fields. It can be seen first that the emission frequency increases with the rise of magnetic field, which is in agreement with the Kittel equation [5]:

$$f_0 = \gamma/2\pi\sqrt{(H + H_{an} + H_d)(H + H_{an} + H_d + 4\pi M_{eff})} \qquad (3.2)$$

Meanwhile, the signal amplitude dramatically decreases with the increasing magnetic field, due to the enhanced damping torque. Concerning the signal modulation, a large frequency (amplitude) tuning range is normally preferred in FSK (ASK) scheme. From the phase diagrams shown in Figure 3-4 (a), a wider frequency tuning range for current is observed under a larger magnetic field while a higher amplitude tunability for current is obtained under a smaller magnetic field.

3.4 Basic characterization for memristor

Recently we developed a memristor stack of TiN/TaO_x/HfO_2/TiN with high performance [133]. The TaO_x layer was shown to act as an in-built current compliance layer in the memristor device and improve thermal efficiency, which resulted in a much better reliability compared to the well-studied memristor stacks such as TiN/Ti/HfO_2/TiN.

In general, memristors exhibit two switching modes, the unipolar switching and the bipolar switching. For unipolar switching, we change the amplitude rather than the polarity of the applied voltage to manipulate the resistance of memristors. Thus, set/reset process takes place at the same polarity. For bipolar switching, the applied voltage bias for reset and set are opposite. Figure 3-5 (a) shows a typical I-V curve of our device, showing classical bipolar switching behaviors. When the positive applied voltage exceeds a certain threshold, the resistance decreases dramatically, which is generally attributed to oxygen ions drifting to the anode interface, the so-called formation of conductive filaments in metal oxide. By contrast, the conductive filaments break under reversed voltage bias, returning the memory cell to a high resistance state [134]. Such switching mechanism has been explained more comprehensively in another recent work [135]. Based on this, memristors also exhibit multilevel resistance states when setting different current limits as shown in Figure 3-5 (b). Applying voltage pulses with different amplitudes lead to different resistance states. Such operation method is similar as that for Phase Change Memory (PCM). Specifically, a small voltage leads to the formation of thin conductive filaments while a larger voltage results in thick ones.

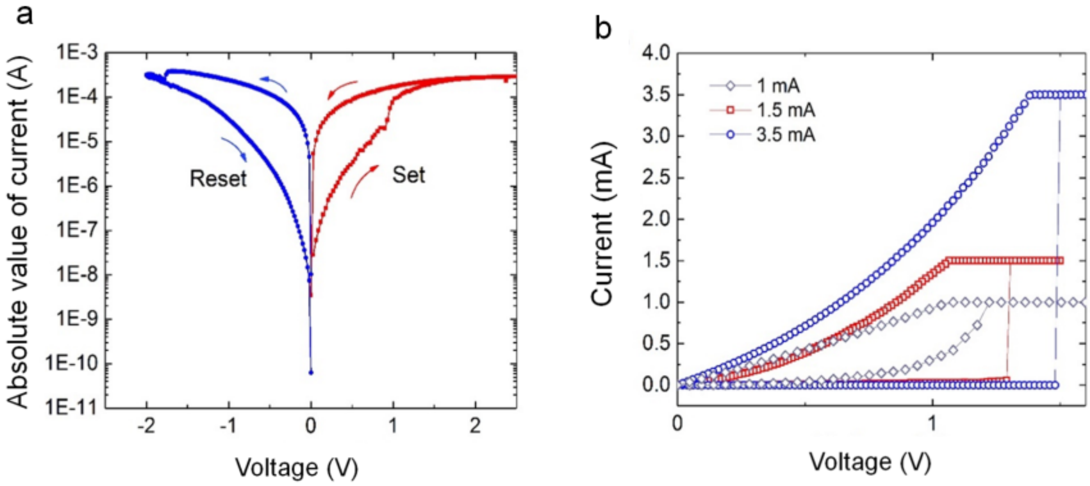

Figure 3-5 (a) Typical set and reset process of our memristor device. (b) Multilevel resistance states were realized by setting different compliance currents.

3.5 Microwave Modulation based on MSN

Background

WSNs are a new class of distributed systems that mainly consist of a central microcontroller, sensor nodes, sink nodes and communication device [136], as shown in Figure 3-6.

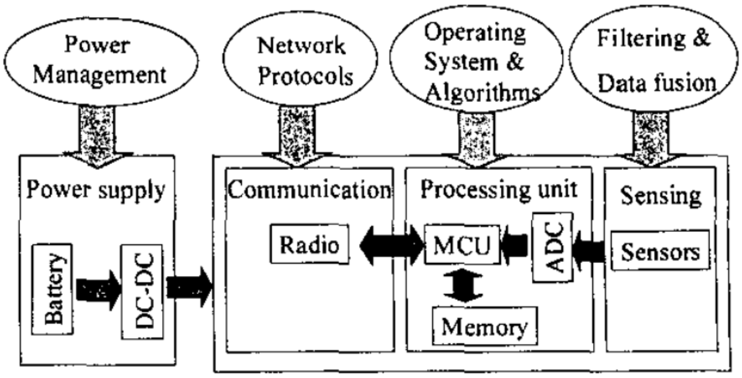

Figure 3-6 Typical architecture of WSNs. Extracted from [136].

In many cases, a large amount of sensor nodes are required in WSN. The information transmissions between these nodes are implemented by wireless communication. As a consequence, wireless communication is normally the most power consuming part in WSNs, as shown in Figure 3-7 [137]. Now it is urgent to develop compact, low cost and low power consuming microwave devices

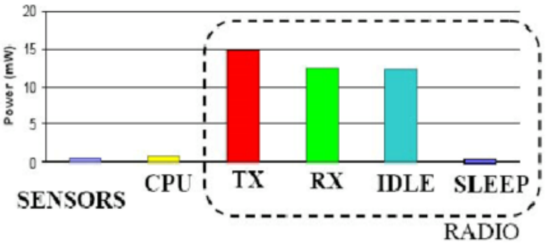

Figure 3-7 Power consumption distribution in WSNs. Extracted from [137].

As introduced above, STNOs are a novel type of oscillators which is promising to be used for wireless communication. However, due to their low power output, STNOs cannot provide strong enough carrier signal to drive the RF mixer. Recently, U. Ebels's group in Spintec proposed a solution which applies the FSK to STNO-based modulation [9]. In this case, the information is encoded and indicated by different frequency. Importantly, since the frequency of microwave emission in STNO can be directly tuned by changing the injected current, the RF mixer is not required [138-141]. In this section, we present a novel modulation approach, in which the STNO is connected with a memristor in series. We demonstrate that both the frequency and amplitude can be varied by setting the memristor into different resistance states, showing potential of being used for ASK and FSK.

Results

As is shown above in Figure 3-4, for single STNO, the frequency of microwave output can be varied by changing the injected current. Here, we proposed a new modulation approach by combining the STNO and memristor. The operation process can be described as follows: first, we apply a voltage pulse on memristor to reset it to a high resistance state where the STNO stops emitting due to the weak current injection; then a reversed voltage pulse set the memristor to different low resistance states which lead to different microwave output.

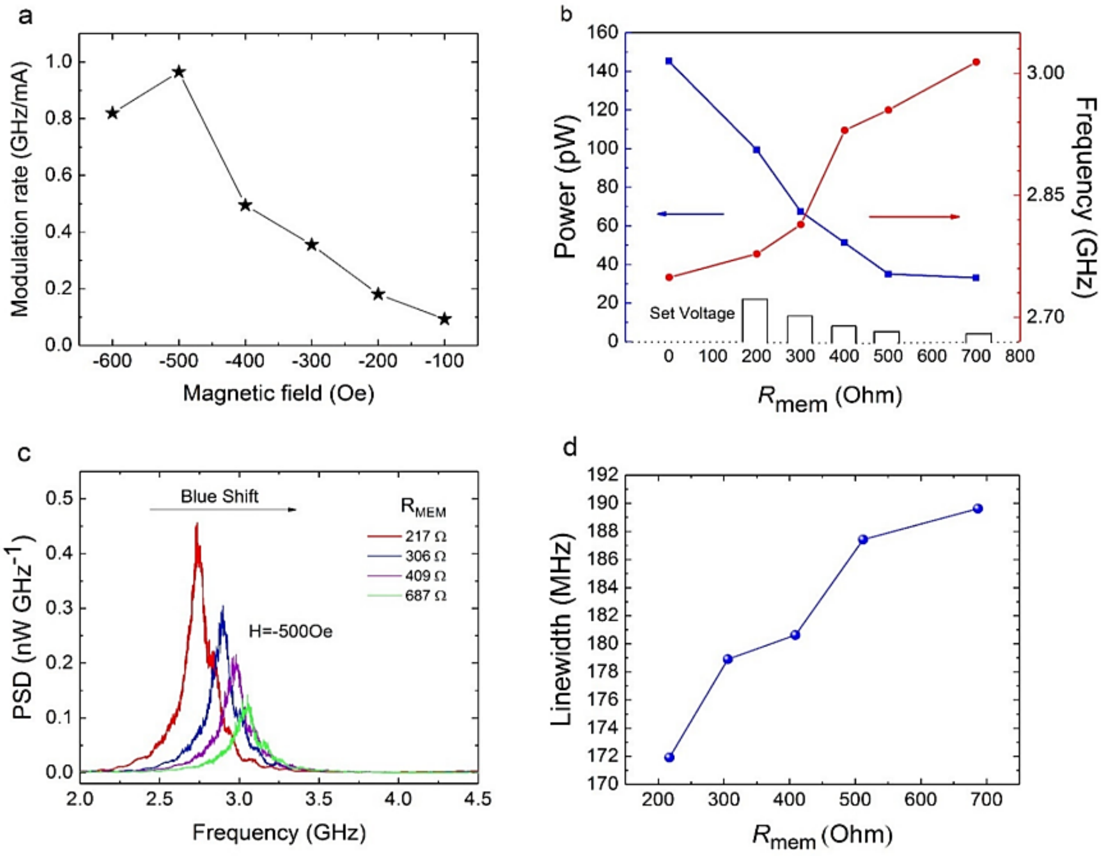

Figure 3-8 (a) Frequency tunability as a function of external magnetic field which was extracted from Figure 3. (a). (b) Output voltage and frequency modulation as a function of resistance states of memristor.(c) Power spectrum of modulated signals which show blue shift.(d) Linewidth vs Resistance of memristor.

To demonstrate the feasibility of MSN, first we connected different resistors instead of real memristor devices to STNO. Obvious frequency shift can be observed on the emission spectra (not shown here). Afterwards, we connected STNO to memristor via wire-bonding on specially-designed high frequency PCB board. We set memristor into different resistance states by applying a train of voltage pulses. As is shown in Figure 3-8(b), with the increasing resistance of memristor. the amplitude decreases and the signal shows a clearly blue shift which can also be identified in Figure 3-8 (c). In addition, the linewidth of microwave output gradually increases as shown in Figure 3-8 (d) while the output voltage dramatically drops to 100 μV below, which could be ascribed to a larger impedance mismatching.

We propose that two factors contribute to the observed results. First, based on the Landau-Lifshitz-Gilbert-Slonczewski (LLGS) equation, the oscillation amplitude of magnetization depends on damping torque that is intrinsic and spin transfer torque coming from spin current [142-146]. The variation of memristor resistance modulate the spin current injected to the connected STNO, which further change the amplitude and frequency of microwave signal [147-149]. Note that the STT acting on the free-layer magnetization $\boldsymbol{m}$ due to the misalignment with the polarizing layer magnetization $\boldsymbol{p}$ is given by two terms. The first term $\boldsymbol{T}_{/\!/}$ corresponds to a transfer of the transverse component of the spin momentum that lies in the plane of $\boldsymbol{m}$ and $\boldsymbol{p}$, while the second term, called field-like term $\boldsymbol{T}_{\perp}$, corresponds to a transfer of the transverse component that is perpendicular to the plane of $\boldsymbol{m}$ and $\boldsymbol{p}$. In this thesis, the field-like term is neglected, as it is assumed that $\boldsymbol{T}_{\perp}$ does not have strong impact on the dynamics of MTJ-based STNOs.

Second, for the impedance of spectrum analyzer is only ~50 Ω, far less than that of our devices, the transmission efficiency is poor and the impedance matching should be considered. To be more specific, an STNO may be viewed as a time dependent resistor. The resistance of the MSN is given by

$$\begin{aligned} R_{\mathrm{MSN}} = R_{\mathrm{MEM}} + R_{\mathrm{STNO}} &= R_{\mathrm{MEM}} + R_{\mathrm{av}} + \frac{\Delta R}{2}\left(\overrightarrow{m_f} \cdot \overrightarrow{m_p}\right) \\ &\approx R_{\mathrm{MEM}} + R_{\mathrm{av}} + \frac{\Delta R}{2}\cos\omega t \end{aligned} \tag{3.3}$$

where R_{av} is the average resistance of STNO during precession period, R_{L} is the impedance of spectrum analyzer, $\overrightarrow{m_f}$and $\overrightarrow{m_p}$are the magnetization vectors of free layer and pinned layer, respectively. Thus, in this case, the efficiency can be calculated by

$$\begin{aligned}\frac{P_{\mathrm{out}}}{P_{\mathrm{in}}} &= \frac{V_{\mathrm{out}}^2}{2I^2(R_{\mathrm{av}}+R_{\mathrm{MEM}})R_{\mathrm{L}}} \\ &= \frac{1}{8}\frac{\Delta R^2 R_{\mathrm{L}}}{(R_{\mathrm{av}}+R_{\mathrm{MEM}})(R_{\mathrm{av}}+R_{\mathrm{MEM}}+R_{\mathrm{L}})^2} \end{aligned} \tag{3.4}$$

It is obvious that a larger resistance leads to lower matching efficiency, which also contributes to the amplitude modulation.

In addition to frequency and amplitude modulation, we also found that multilevel resistance states can be realized within lower voltage range (<1V) in MSNs. The measured I-V curves of the MSN are shown in Figure 3-9 (a). Apart from the pinched hysteresis loop which is the typical feature of a memristor, the STT switching is also observed in the inset figure. Figure 3-9 (b) presents the R-V curve. Since the magnetic field and the easy axis of MTJ are noncollinear, we can see that the critical switching current increases with the magnetic field. More importantly, because of the dependence of R_{mem} on charge accumulation, the MSN shows four different resistance states, which differs from a standalone MTJ. To test their stability, we ran the I-V sweep process many times under different magnetic field, four resistance states can be always clearly defined.

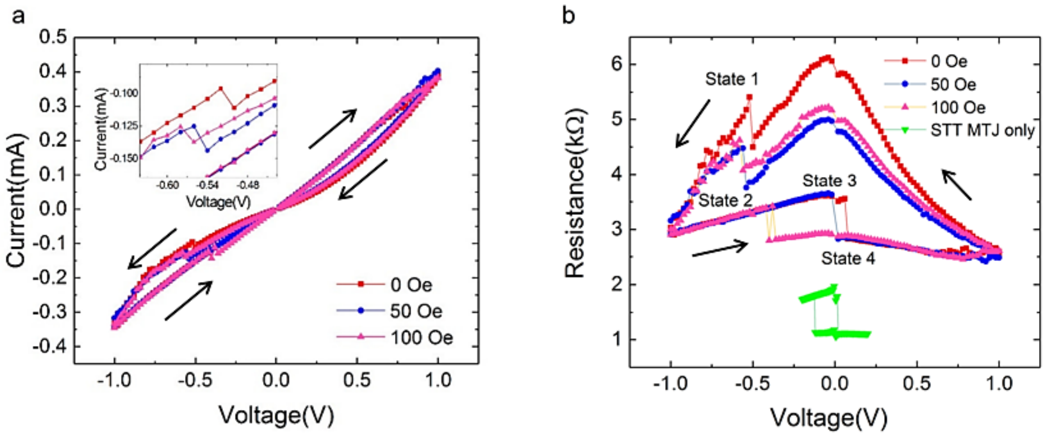

Figure 3-9. Electrical transport property measurements under low sweeping voltage (≤1V). (a) I-V curve and (b) Resistance variation of MSN under different external magnetic field.

3.6 Summary and discussion

In this section, we first studied the dynamics in a CoFeB-based in-plane STNO for different applied magnetic field and current. Then we investigated the transport characteristics of the TiN/TaO$_x$/HfO$_2$/TiN stack. Finally, we demonstrated a novel RF modulation method by combining a memristor with a STNO.

From the dynamics of a standalone in-plane STNO, it can be seen that the microwave characteristics can be tuned by directly changing the injected current. Therefore, STNO can be used for ASK and FSK scheme. Importantly, we show that a wider frequency tuning range is achieved under a stronger magnetic field while a higher amplitude tunability for current is obtained under a smaller magnetic field.

From the transport characterization of a TiN/TaO$_x$/HfO$_2$/TiN stack, we show that multilevel resistance states can be obtained by applying voltage pulses with different magnitude. Moreover, the resistance of the studied memristor is comparable with that of STNO. Therefore the current injected into the STNO can be effectively modulated by setting the memristor into different resistance states.

Finally, a novel RF modulation strategy based on memristor-controlled spin nano-oscillators is proposed for ASK and FSK, whereby the STNO is responsible for microwave emitting, and memristor serves as a current regulator which further modulates the frequency and amplitude of microwave emission.

Résumé du Chapitre 3

Dans cette section, nous avons d'abord étudié la dynamique dans un NOTS planaire à base de CoFeB pour différents champs magnétiques et courants appliqués. Ensuite, nous avons étudié les caractéristiques de transport d'un empilement TiN/TaOx/HfO2/TiN. Enfin, nous avons démontré une nouvelle méthode de modulation RF en combinant un memristor avec un NOTS.

À partir de la dynamique d'un NOTS planaire autonome, on peut voir que les caractéristiques des micro-ondes peuvent être réglées en modifiant directement le courant injecté. Par conséquent, NOTS peut être utilisé pour les schémas MDA et MDF. Surtout, nous montrons qu'une plage de réglage de fréquence plus large est obtenue sous un champ magnétique plus fort tandis qu'une accordabilité d'amplitude plus élevée pour le courant est obtenue sous un champ magnétique plus petit.

À partir de la caractérisation du transport d'un empilement TiN/TaOx/HfO2/TiN, nous montrons que des états de résistance multiniveaux peuvent être obtenus en appliquant des impulsions de tension de magnitude différente. De plus, la résistance du memristor étudié est comparable à celle du NOTS. Par conséquent, le courant injecté dans le NOTS peut être modulé efficacement en réglant le memristor dans différents états de résistance.

Enfin, une nouvelle stratégie de modulation RF basée sur des nano-oscillateurs à spin contrôlés par memristor est proposée pour MDA et MDF, dans laquelle le NOTS est responsable de l'émission de micro-ondes et du memristor, et sert comme un régulateur de courant qui module davantage la fréquence et l'amplitude de l'émission de micro-ondes.

4 Magnetization dynamics in all perpendicular spin nano-oscillators with composite Free Layer

4.1 Introduction

In chapter 3, the magnetization dynamics in a CoFeB-based in-plane STNO under different magnetic field and current are described in detail. However, the microwave emission spectra posses a large linewidth, leading to a small Q factor around 30 which fails to meet the requirements of wireless communication. Thus it is important to design new film stacks for STNOs to optimize their microwave emission.

In 2018, C. Zhang *et al*. presented a steady auto-oscillation in a CoFeB-based perpendicular MTJ (p-MTJ) [150]. As shown in Figure 4-1 (a), the film has a layered structure of bottom contact/$Co_{20}Fe_{60}$ B_{20}(1.2)/MgO(1)/$Co_{40}Fe_{40}B_{20}$(1.5)/$[Co/Pd]_4$(5) /Ru(0.85)/$[Co/Pd]_{10}$(10)/top contact. In dynamical measurement, a narrow linewidth down to 7 MHz corresponding to a high Q factor of 220 was achieved in a nano-sized MTJ pillar, as displayed in Figure 4-1(b), which suggests that the CoFeB-based MTJ with perpendicular magnetic easy axis could be helpful for developing spin-torque oscillators with narrow-linewidth.

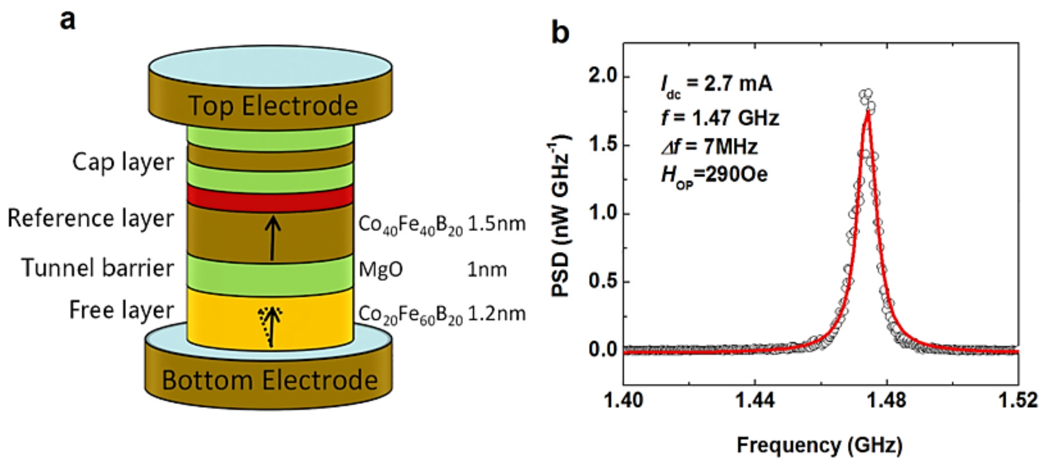

Figure 4-1 (a) Schematic of the structure of studied MgO-based p-MTJ with a diameter around 200nm. (b) A power density spectrum measured under the applied magnetic field of 290Oe. The red line indicates the Lorentzian fitting results. Extracted from [150].

Very recently, we reported spin transfer torque switching in p-MTJs with atom-thick W insertion layers and double MgO/CoFeB interfaces, shown in Figure 4-2[64]. Such kind of stacks show a high PMA, a large TMR of 249% and a low switching current of 3.0 mA/cm^2. Specifically, the single-atom W layer benefits the p-MTJ nano-pillar from the following aspects. First, using First-Principles calculation, it was revealed that the atom-thick W layers can induce more efficient resonant tunnelling transmission, which contributes to the larger magnetoresistance ratio in comparison with conventional MTJs with Ta layers. Second, it has been proved that the damping constant α is material dependent. By replacing Ta with W, a low α can be obtained, leading to a low J_c. Third, the atom-thick W layer not only provide a typical bcc template for the texture of adjacent CoFeB layers, but also absorb B atoms during annealing. Both the crystalline structure and atom distribution contribute to the large interfacial PMA. The p-MTJs with atom-thick W layers show great static transport properties. In this chapter, I focus on the dynamical characterization of such stacks.

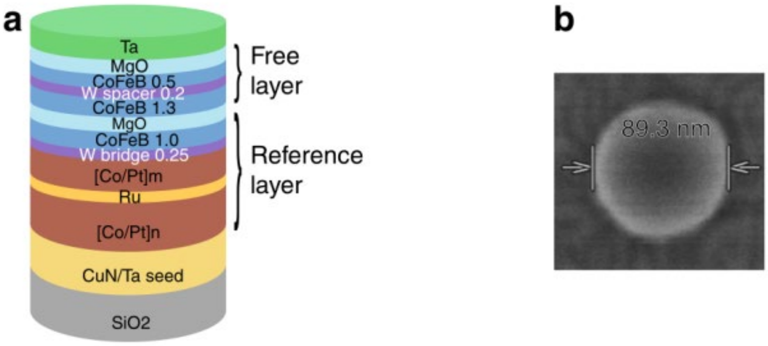

Figure 4-2 (a) Schematic illustration of p-MTJs with atom-thick W layers and double MgO/CoFeB interfaces. (b) Top view of a 89nm-wide MTJ pillar obtained via Scanning electron microscope (SEM). Extracted from [64].

4.2 Samples and experimental details

The p-MTJ stacks I studied here were composed of from the substrate side, Ta(5)/Ru(30)/Ta(0.7)/Pt(1.5)/6x[Co(0.5)/Pt(0.2)]/Co(0.6)/Ru(0.8)/Co(0.6)/3x[Pt(0.2)/Co(0.5)]/W(0.25)/CoFeB(1.0)/MgO(0.8)/CoFeB(1.3)/W(0.3)/CoFeB(0.5)/MgO(0.75)/Pt(0.

4)/Ta(3)/Ru(8) nominal thickness in nm)，as shown in Figure 4-3 (a). These layers were deposited on thermally oxidized Si substrate by a Singulus magnetron-sputtering system, where the MgO layers were deposited by RF magnetron sputtering whereas the other layers were deposited by DC magnetron sputtering. The deposited stacks were post-annealed in vacuum at 400 °C for 1 hour without any external magnetic field. Then, the Ta/Ru hard masks were fabricated using electron beam (e-beam) lithography and inductive coupling plasma etching. p-MTJs were defined by multistep Ar ion milling by using the Ta hard mask while varying the beam angle. During milling, we monitored the secondary-ion mass spectra and stopped the milling operation when the signal was detected through the 0.8-nm-thick MgO barrier. The diameter is around 110nm. The bottom residual metal layers were used as the bottom electrode for electrical measurement.

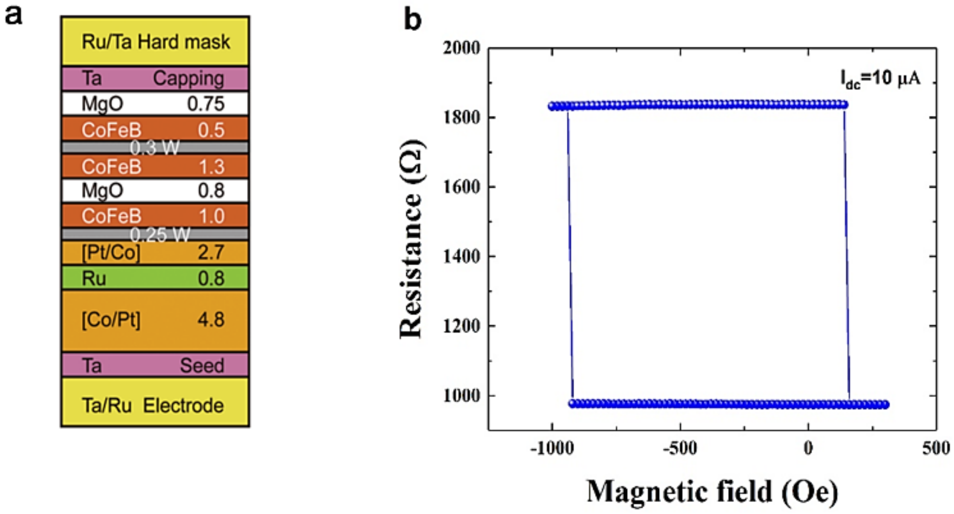

Figure 4-3 (a) Schematic illustration of the studied p-MTJ structure. (b) Magneto-resistance curves of the STNO measured under out-of-plane magnetic fields.

The measurement set-up is similar to that described in the last chapter. As is schematically illustrated in Fig. 4-4, the STNO device is connected to a DC source via ground signal ground (GSG) RF probe. We measure the static transport properties at room temperature under a constant DC current of 10μA. A Rohde & Schwarz spectrum analyzer was used for characterizing the power spectral density. Bias-T separates the output from driving source. The STT-induced magnetization oscillation generates a high-frequency voltage output signal due to the time variation in resistance originating from the TMR effect. Output signals were recorded after 40 dB amplification and the background noise, measured at zero dc current, was subtracted from the power spectra. All the RF measurements were performed at room temperature with a tilt magnetic field applied using a projected field electromagnet that allows us to control the field angle continuously. The positive I_{dc} is defined as the direction of the electron flow from the free layer to the pinned one.

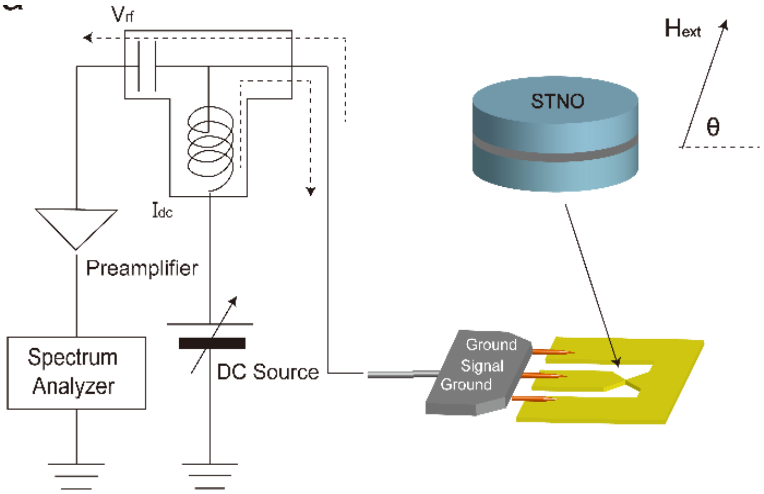

Figure 4-4 Schematic illustration of the measurement set-up used for dynamic characterization of STNO. The current is injected through a GSG rf probe and bias tee. Experiments are performed under a tilted external magnetic field.

4.3 Results

4.3.1 PSD measured under external magnetic field along different directions

Fig. 4-5 (a) shows the PSD measured under different directions of applied magnetic field H_{ext}, where H_{ext}=1000 Oe, I_{dc}=400 μA and θ is the angle with respect to the x-y plane. With the field tilts toward out-of-plane, the frequency drops dramatically from 7.66GHz to 3.39GHz while the linewidth gradually decreases from 152MHz to 56MHz. In addition, the peak power also shows strong dependence on field direction. The decreasing linewidth suggests that the magnetization dynamics become more coherent as θ increases [151-153]. The increasing peak power indicates that the precession amplitude grows with increasing θ. Furthermore, as is shown in Fig. 4-5 (b) and (c), dependence of frequency on magnetic field (H_{ext}) is described. As H_{ext}

increases from 100Oe to 1000 Oe, the emission frequency exhibits an approximately linear dependence on field with different slope rate determined by the direction of field. Based on the Kittel's formula, $\mathrm{f} = \gamma(H_{ext} + H_K - 4\pi M_S)/2\pi$, where H_K is the perpendicular anisotropy field and the $4\pi M_S$ is the saturation magnetization of CoFeB free layer, the $H_K - 4\pi M_S$ can be estimated around 1.150 kOe. The experimental value of $4\pi M_S$ is 14.7 kOe [111]. Then, the perpendicular anisotropy field here can be calculated as 15.85 kOe, which is very high and thus leads to a high emission frequency of 7.6 GHz when $\theta = 30°$, H_{ext}=1000 Oe and I_{dc}=400 μA. Along with our previous study, the high PMA in such stacks can be explained as follows. In the sample presented in this study there are two interfaces of CoFeB/MgO which effectively enhanced the perpendicular anisotropy. In addition, CoFeB/heavy metal interfaces with strong spin–orbit coupling also contribute to perpendicular anisotropy. Fig. 4-5 (d) shows the dependence of integrated power on external field. Theoretically, the emission power of a nanopillar STNO can be expressed as follows:

$$\mathrm{P} = \frac{1}{8}\eta(MR')^2\left(\frac{\Delta\theta}{2}\right)^2 sin^2\theta_0 R(\theta_0) I^2, \tag{4.1}$$

$$\mathrm{MR}' = \frac{R(\pi) - R(0)}{R(\theta_0)}, \tag{4.2}$$

$$\eta = \frac{4R(\theta_0)Z_0}{(R(\theta_0) + Z_0)^2}. \tag{4.3}$$

It is seen the microwave power is influenced by the average angle θ_0 between magnetization in free and reference layer, the precession cone angle of the free layer magnetization $\Delta\theta$, transmission efficiency η, MR ratio, resistance $\mathrm{R}(\theta_0)$ and electrical current I_{dc}. In this study, the electrical current is fixed at 0.4 mA. By increasing the magnetic field, the magnetization direction of free layer gradually tilts toward in-plane, thus both the average angle θ_0 and precession cone angle $\Delta\theta$ increase which leads to the enhancement of emission power.

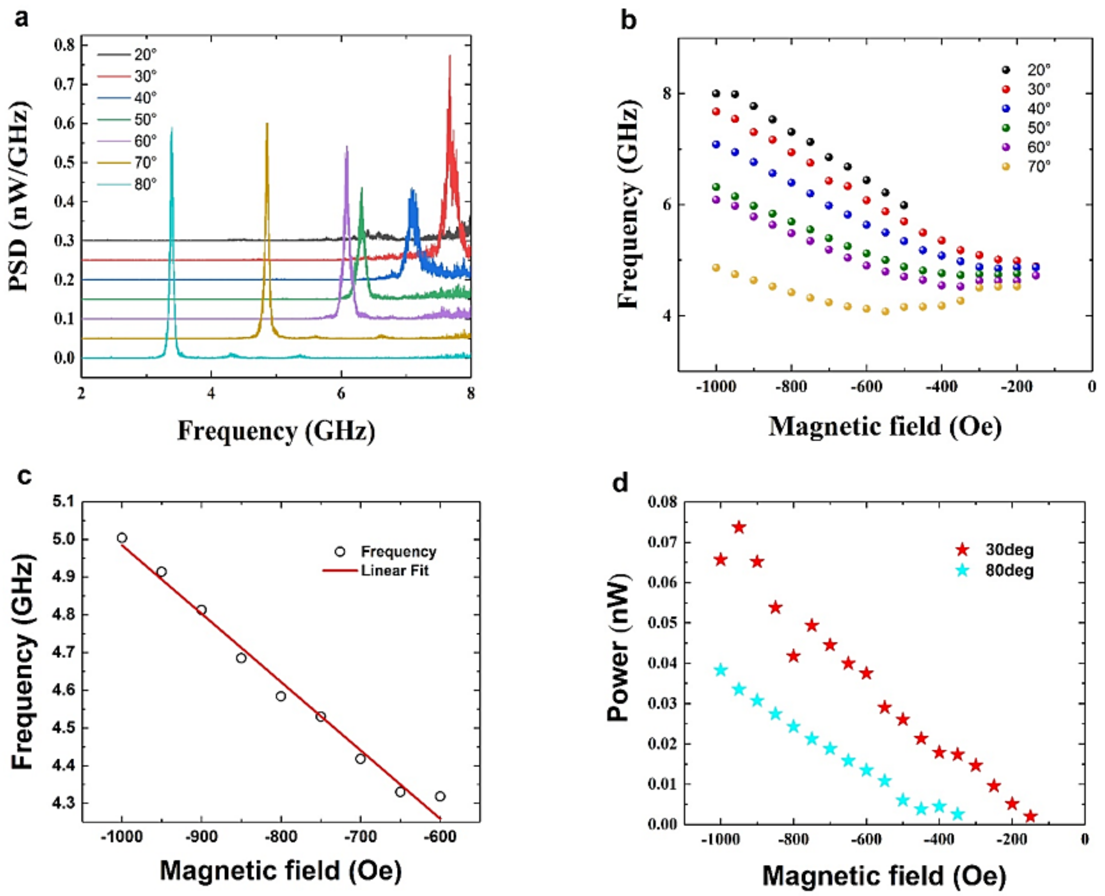

Figure 4-5 (a) Power spectrum density (PSD) measured under external magnetic field H_{ext}=1000Oe at different direction. (b) Dependence of microwave frequency on external magnetic field. All the data was extracted from PSD which is shown in Fig.2. (a). (c) Results of linear fitting for frequency shift when the magnetic field angle $\theta = 70^{\circ}$. (d) Dependence of integrated power on different magnetic field.

4.3.2 PSD measured for different current

Figure 4-6 (a) shows microwave emission spectra for different I_{dc}. To avoid damaging devices, all data presented here were collected at I_{dc}=400 μA or below. When the current is positive, steady precession cannot be sustained because both the spin current and field favor the antiparallel state. Nevertheless, the negative current reduce the net effective damping to zero, which results in spontaneous steady state magnetic precession [154-160]. Below 0.15 mA, no obvious microwave emissions are observed. By gradually increasing the current above 0.2 mA, one dominant single oscillation peak appears obviously, suggesting the onset of a uniform steady magnetization precession. Figure 4-6 (b) shows emission spectra at I_{dc} = −400 μA which is well fitting with a Lorentian function. The central peak frequency is around 4.85 GHz and a narrow linewidth (Δf) of 61 MHz is obtained.

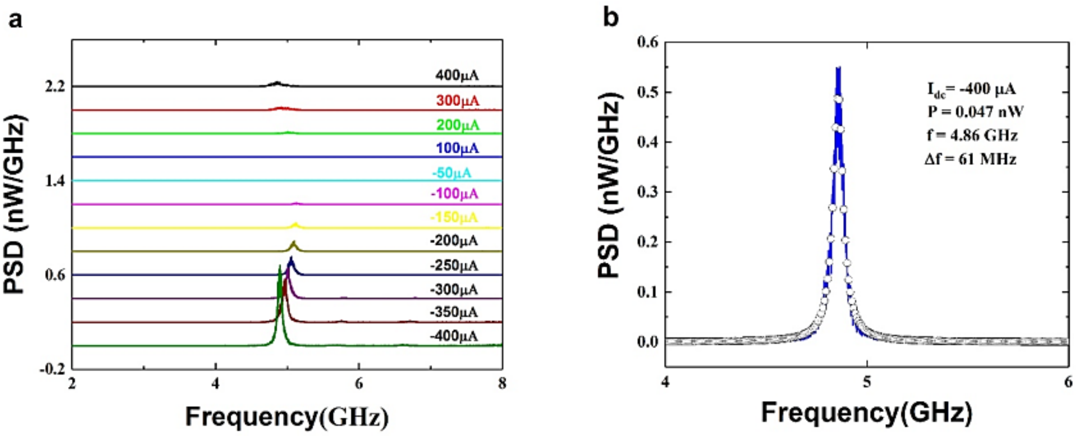

Figure 4-6 (a) Power spectrum density (PSD) measured with different dc current under external magnetic field of 1000 Oe. The field angle is 70° (b) Spectrum and Lorentian fitting for I_{dc}=−400 μA.

Figure 4-7 (a) shows the quantitative data extracted from emission spectra by Lorentian fitting. It is seen that the output power rapidly increases with I_{dc} while the frequency gradually declined, the calculated frequency tunability is about $0.86\ \mathrm{GHz} \cdot mA^{-1}$, which is larger than a previous work on single free layer STNO [118]. In addition, low-power emissions can be observed at positive current due to thermally excited ferromagnetic resonance (TE-FMR). As is presented in Figure 4-7 (b), linewidth also shows strong dependence on I_{dc}. In the low-current regime, the precession amplitude is small and it induces large-linewidth signal due to the enhanced relative effect of thermal fluctuations for small-amplitude magnetization oscillations. Subsequently, linewidth decreases with increasing the I_{dc} since the precession amplitude is considerably larger. In our device, a narrow linewidth of 61MHz can be obtained when I_{dc} = −400μA, which is comparable with single free layer STNOs [161-168]. Hence, we conclude that the strong ferromagnetic coupling between the two free layers can drive coherent precession. Moreover, a high PMA leads to a uniform demagnetizing field in nanosized pillars, which is also supposed to contribute to the narrow linewidth.

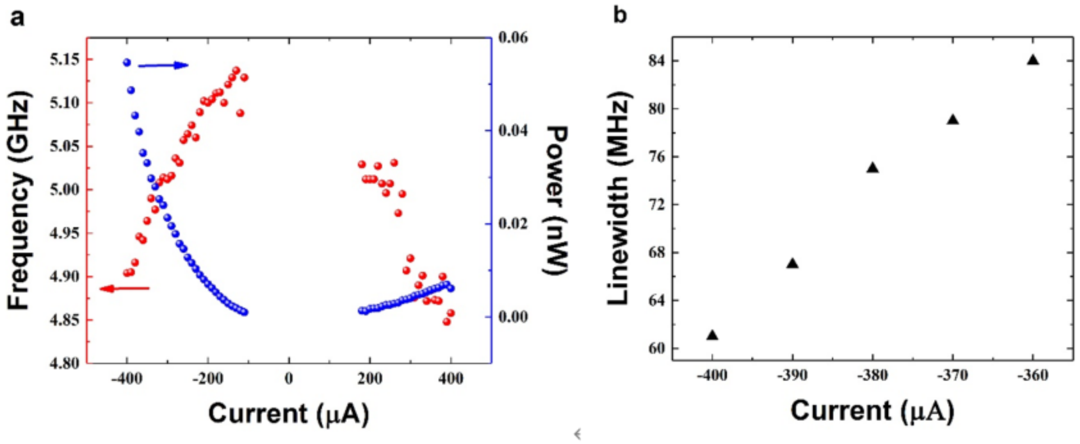

Fig. 4-7 (a) Integrated power and frequency as a function of current under the external magnetic field of 1000 Oe. (b) Dependence of Linewidth on current. Data were collected from spectrum shown in Fig. 3.

4.4 Summary and discussion

In this chapter, I present my study on the magnetization dynamics in a CoFeB-MgO based p-MTJ which has two free layers separated by an atom-thick W insertion. The ultrathin W spacer layer not only enables the two CoFeB free layers precess synchronously but also greatly enhance the PMA, inducing high frequency microwave emission.

The studied perpendicular STNO generates microwave output with a high frequency of 7.6GHz and a large frequency tunability of $0.86\,\mathrm{GHz}\cdot\mathrm{mA}^{-1}$ under a moderate external magnetic field. Importantly, a high Q factor around 80 is obtained which is much higher than that of CoFeB-based in-plane STNOs studied in chapter 3. Along with our previous work, p-MTJs with composite free layer are promising to be used as STNOs.

Résumé du Chapitre 4

Dans ce chapitre, je présente mon étude sur la dynamique d'aimantation dans un jonction tunnel magnétique perpendiculaire (p-JTM) à base de CoFeB-MgO qui a deux couches libres séparées par une insertion de W d'épaisseur atomique. La couche d'espacement ultrafine de W non seulement permet aux deux couches libres de CoFeB de précéder de manière synchrone, mais aussi améliore considérablement le PMA, induisant une émission de micro-ondes à haute fréquence.

Le NOTS perpendiculaire étudié génère une sortie micro-ondes avec une fréquence élevée de 7,6 GHz et une grande accordabilité en fréquence de 0,86 $\mathrm{GHz \cdot mA^{-1}}$ sous un champ magnétique externe modéré. Il est important de noter qu'un facteur Q élevé autour de 80 est obtenu, ce qui est beaucoup plus élevé que celui des NOTS planaire à base de CoFeB étudiés au chapitre 3. Parallèlement à nos travaux précédents, les p-JTMs avec couche libre composite promettent d'être utilisés comme NOTS.

5 A study on all-optical helicity-independent switching state diagram in GdFeCo alloys

5.1 Introduction

The mechanism of AO-HIS observed in GdFeCo alloys has been explained by the presence of two magnetization sublattices with two different relaxation times leading to a transient ferromagnetic-like state [10]. Later, Gorchon *et al.* studied the role of electron temperature in the formation of such state [12]. According to this work, the laser fluence should be high enough to sufficiently heat the free electrons, and initiate the demagnetization and switching process. On the other hand, the laser fluence should also ensure that the phonon temperature T_{ph} is below T_c, since crossing T_c would lead to magnetic disorder and the final magnetization state would then be determined by the cooling conditions. Therefore, AO-HIS should only occur within a narrow range of pulse fluence.

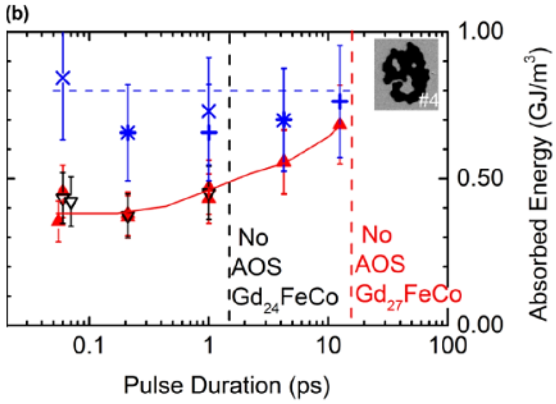

Figure 5-1 Critical fluence for switching (red triangle) and multidomain state (blue cross) as a function of pulse width. Extracted from [12].

In addition, the pulse duration is another important laser parameter. As mentioned above, high T_e is essential for AOS, so it is initially predicted that the maximum pulse duration ($\tau_{\max}$) should be on the timescale of the electron-lattice interaction τ_{e-l} (around 2 ps in GdFeCo) in order for a dramatic heating of electrons. However, Gorchon *et al.* demonstrated AOS in a 15 nm $Gd_{27}FeCo$ film with a pulse duration up to 15 ps as shown in Figure 5-1, which raise new questions about the fundamental mechanism of helicity-independent AOS. Very recently, Davis *et al*. presented a new understanding about pathways for single-shot AOS in ferrimagnets [169]. As shown in Figure 5-2, the magnetization states of a ferrimagnetic $A_{100\text{-}x}B_x$, where A and B are two antiferromagnetically coupled sublattices, are indicated by green dots in a Cartesian coordinate system. S_A and S_B are spin moments of A and B sublattices, respectively. The lines connecting the initial state and final state indicate the switching routes. Apparently, $A_{100\text{-}x}B_x$ needs to go through states 1, 2 and 3 in sequence to achieve magnetization reversal, indicating spin moment of A should reach 0 before B. However, a long pulse duration (~ps) results in comparable demagnetization rates of A and B (inset), which does not satisfy the condition for switching. On the other hand, the initial state and final state vary with the change of composition of AB. Increasing the concentration of B leads to a larger distance between these two states in this coordinate system, which allows a steeper line to connect them. In other words, a longer pulse duration still satisfy the condition required for magnetization reversal for a higher B concentration.

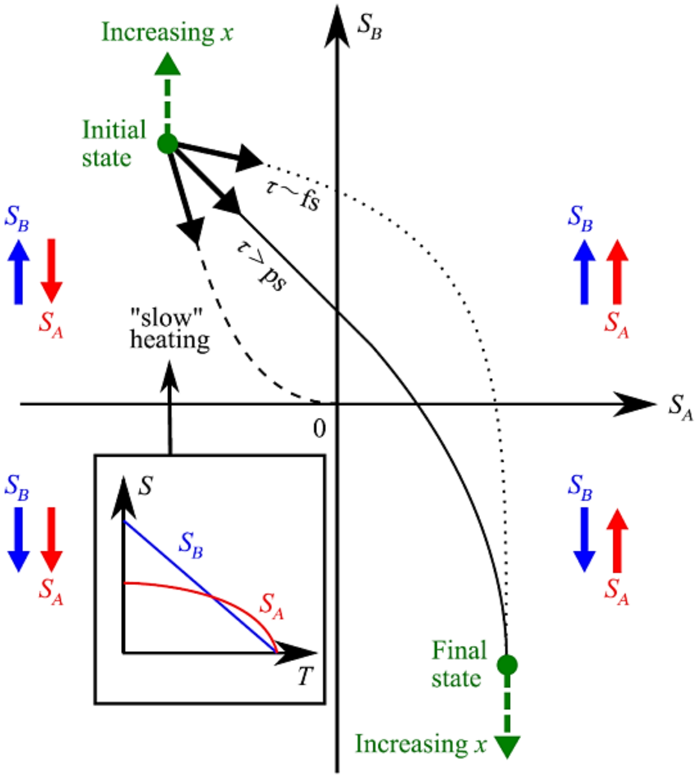

Figure 5-2 Pathways for AO-HIS in ferrimagnets $A_{100-x}B_x$. Extracted from [169].

These works indicate that pulse parameters have very significant influences on single-shot AO-HIS. A deep understanding about this would help us to optimize the material properties and the laser characteristics to obtain energy-efficient AOS. In this chapter, I present a study about the magnetization state diagrams for GdFeCo thin films with different compositions and thicknesses, which clearly reveals the dependence of single-shot AO-HIS on laser parameters.

5.2 Samples preparation

We prepared a series of 10 nm and 20 nm thick $Gd_x(FeCo)_{100-x}$ layers with different Gd concentrations around the compensation concentration ranging from 22% to 27%. The amorphous alloys are ferrimagnetic metallic materials, with two antiferromagnetically exchange coupled sublattices. The net magnetization of the alloy is given by the sum of the transition metal (FeCo) sublattice magnetization and the rare-earth (Gd) sublattice magnetization. Therefore, by tuning the composition of the $Gd_x(FeCo)_{100-x}$, it is possible to modulate the magnetic properties. For a composition called the magnetization compensation point ($x=x_{comp}$), the net magnetization reaches zero and the coercivity diverges. The investigated samples were deposited by DC magnetron sputtering onto a glass substrate according to the following multilayered structure: Glass/Ta (3 nm)/Pt (5 nm)/$Gd_x(FeCo)_{100-x}$ (t nm)/Ta (5 nm). The thin Ta capping layer on top prevents the oxidation of the magnetic film, while allows the probing of the magnetic properties via magneto-optical Kerr effect (MOKE). The bottom Ta layer improves adhesion of the structure to the glass substrate. According to the magnetic hysteresis loops obtained by MOKE (see Figure 5-3), all studied samples show strong perpendicular magnetic anisotropy (PMA). From the MOKE results, at room temperature, we could determine x_{comp} between 24 % and 25 %. The net magnetic moment is thus aligned in the direction of the FeCo magnetization sublattice below x_{comp} while it changes its sign and becomes aligned with the Gd magnetization sublattice above x_{comp}. Note that x_{comp} also depends on the temperature.

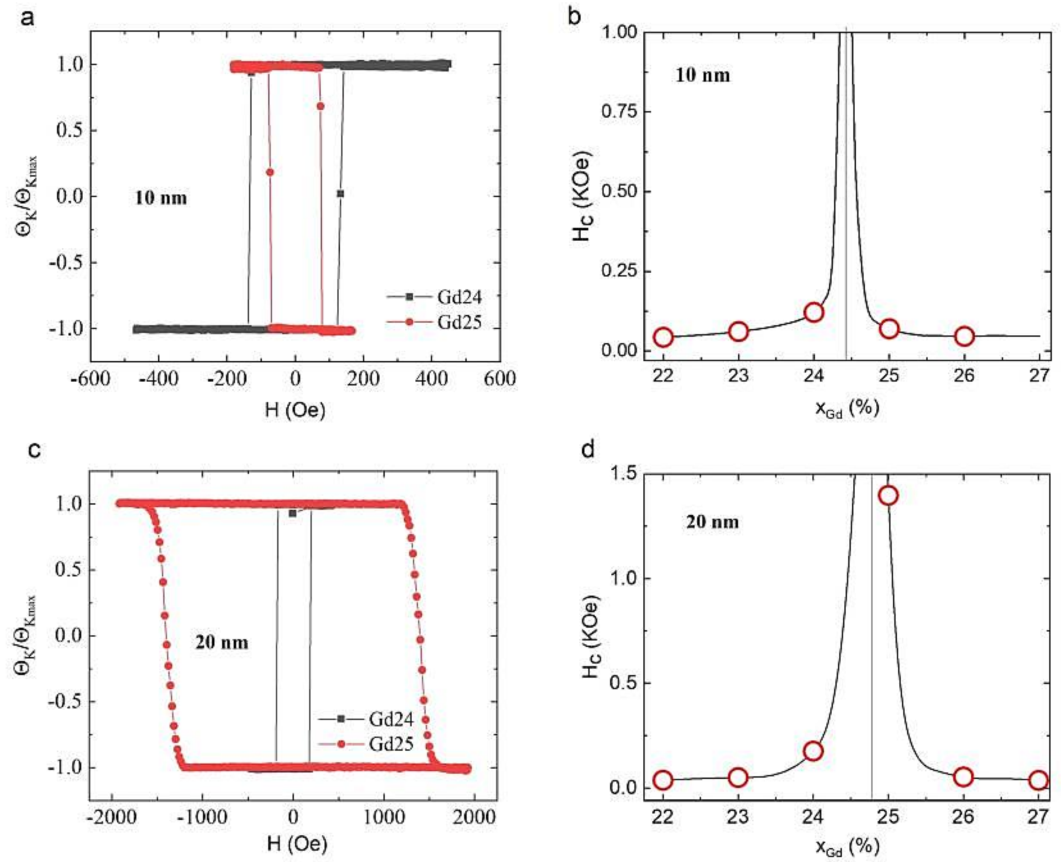

Figure 5-3 Magneto-Optical Kerr Effect (MOKE) results obtained for a 10nm and a 20 nm Gd$_x$(FeCo)$_{100-x}$. (a) Normalized Kerr angle ($\Theta_K/\Theta_{K_{max}}$) as a function of the magnetic field H applied perpendicular to the film plane for a 10 nm Gd$_x$(FeCo)$_{100-x}$ with x = 24% and 25 % . (b) Coercive field H_c deduced from hysteresis loop for a 10 nm Gd$_x$(FeCo)$_{100-x}$ such as the one presented in (a) as a function of the composition x. (c) Normalised Kerr angle ($\Theta_K/\Theta_{K_{max}}$) as a function of the magnetic field H applied perepependicular to the film plane for a 20 nm Gd$_x$(FeCo)$_{100-x}$ with x = 24% and 25 %. (d) Coercive field H_c deduced from hysteresis loop for a 20 nm Gd$_x$(FeCo)$_{100-x}$ such as the one presented in (a) as a function of the composition x.

5.3 Results

5.3.1 Magnetization state diagram of GdFeCo

To build the magnetization state diagram for GdFeCo, we need to record its magnetic state for different parameter combinations. More specifically, for different pulse durations, the fluence thresholds at which AOS or a multidomain state is observed are recorded.

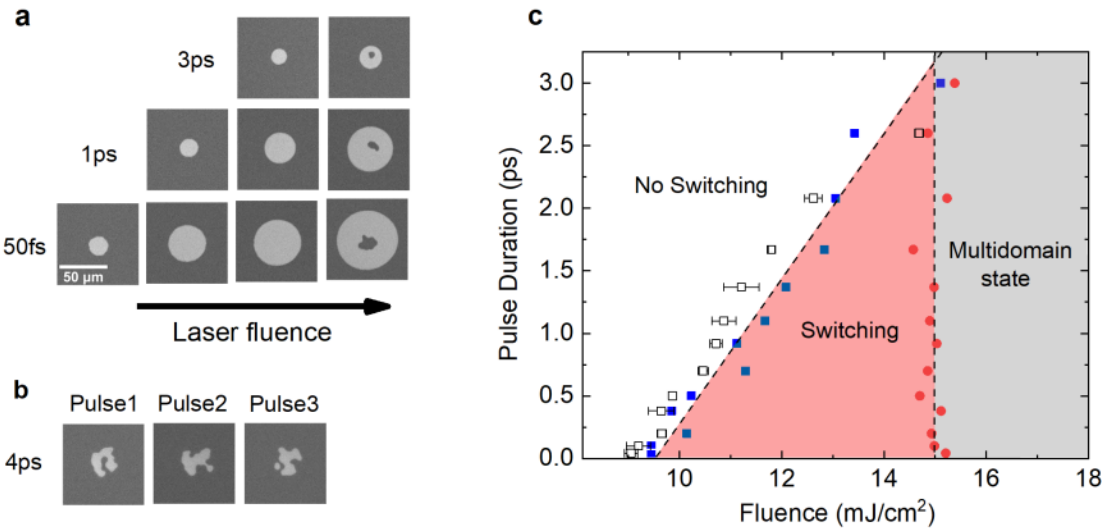

Fig. 5-4 Magneto-optical images and all optical helicity independent switching state diagram for a 20 nm Gd$_{24}$(FeCo)$_{76}$ film. (a) Magneto-optical images of Gd$_{24}$(FeCo)$_{76}$ after exposure to a single linearly-polarized laser pulse with a pulse duration of 50 fs, 1 ps and 3 ps, and with various fluences ranging from 9.5 to 15 mJ/cm^2. (b) Magneto-optical images of Gd$_{24}$(FeCo)$_{76}$ after exposure to a single linearly-polarized laser pulse with a pulse duration of 4 ps and a fluence of 17 mJ/cm^2. (c) AO-HIS state diagram: Switching fluence F_{Switch} (open black square and full blue square) and multidomain fluence F_{Multi} (full red circle) as a function of the pulse duration for a single linearly-polarized laser pulse. The blue full squares represent the critical switching fluences F_{Switch} recorded when the diameter of switched area reaches around 10 μm. The open squares are the fitting results obtained via the method proposed by Liu *et al.*[170] The spatial full-width half-maximum (FWMH) of laser beam is around 70 μm.

Fig. 5-4 (a) shows magneto-optical images obtained on a 20 nm Gd$_{24}$(FeCo)$_{76}$ film after exposure to a single laser pulse for different pulse durations (50 fs, 1 ps and 3 ps) and different fluences. The film is initially saturated under an external magnetic field before exposure. We could observe that above a certain fluence defined as F_{Switch}, the magnetization of the GdFeCo switches. Moreover, the spot showing AO-HIS expands as the fluence increases and a similar trend is shown for different pulse durations. It is clear that F_{Switch} depends on the pulse duration. For fluences lower than F_{Switch} the laser has no effect on the magnetic configuration (not shown). Above a given fluence F_{Multi}, multiple domains start to appear in the middle of the spot. Consequently, AO-HIS is only observed for a fluence value between F_{Switch} and F_{Multi}. In addition, as displayed in Fig. 5-4(b), fully demagnetized patterns are only found when the pulse duration increases to 4 ps, indicating that deterministic all-optical switching could not be achieved above certain pulse duration whatever the laser fluence. Indeed, for AO-HIS the fluence window for switching narrows as the pulse duration increases, which is opposite to the trend observed for AO-HDS for which the fluence window broadens as the pulse duration increases.

To gain a more detailed insight of the dependence of AO-HIS on the pulse characteristics, F_{Switch} and F_{Multi} are presented as a function of the pulse duration indicated by blue squares and red dots, respectively, as shown in Fig. 5-4(c). The open squares indicate the F_{Switch} obtained via the method proposed by Liu *et al*. [170]. This AO-HIS state diagram allows defining the single pulse laser characteristics leading to AO-HIS, multidomain state or no reversal. Moreover, F_{Switch} and F_{Multi} show obviously different dependence on pulse duration. F_{Multi} is independent on the pulse duration in this pulse duration range, whereas F_{Switch} shows in first approximation a linear increase as the pulse duration increases until $F_{\text{Switch}} = F_{\text{Multi}}$ which defines the maximum pulse duration (τ_{max}) for which AO-HIS can be observed. Increasing further the pulse duration only lead to a multidomain state.

Method for extracting the accurate F_{Switch}

The critical fluences for switching F_{Switch} indicated by blue squares in Figure 5-4 are recorded when a switching domain was observed. However, due to the resolution limitation of the microscope, there should be a deviation from the true values of F_{Switch}. To make sure if these errors are acceptable, we calculated F_{Switch} via the method proposed by Liu *et al* [170], which are indicated by open squares. According to their work, the relationship between radii r of switching domain and laser fluence F is given by:

$$r^2 = \rho^2 \left(\ln F - \ln F_{Switch}\right) \tag{5-1}$$

where ρ is the coefficient connecting the fluence with radii r. The threshold fluence for switching F_{Switch} can be derived from the intercepts of the fit lines on the horizontal axis. Thus, we recorded a group of magneto-optical images for 20 nm $Gd_{24}FeCo$ after exposure to laser pulses with different fluences and pulse durations as shown in Figure 5-5. From equation 5-1, r^2 shows a linear dependence on ln F. The linear fitting results for 200 fs, 700 fs and 1.67 ps are represented in Figure 5-6 for illustration. Finally, we find that the critical switching fluences obtained using these two methods are very close and show similar trends (shown in Figure 5-4).

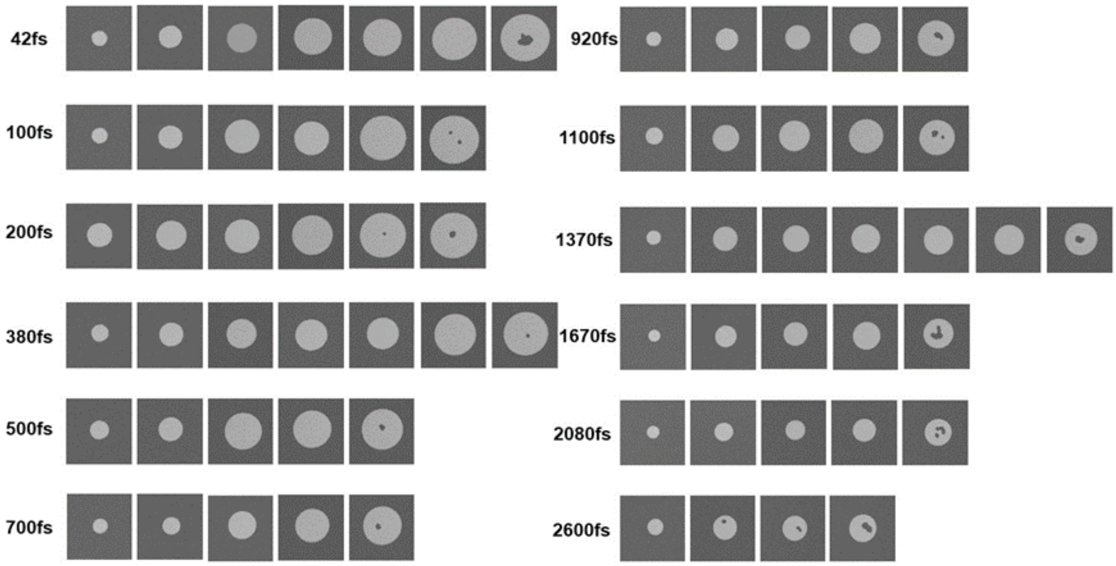

Fig. 5-5 Magneto-optical images of 20 nm $Gd_{24}(FeCo)_{76}$ after exposure to laser pulses with different fluence and pulse durations.

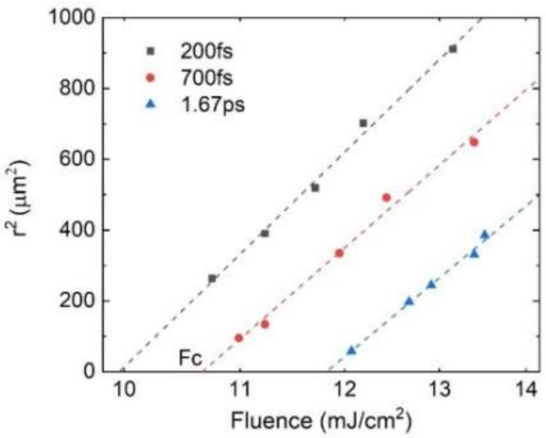

Fig. 5-6 Semilog plots of the energy dependence of radii of switching domain, induced by 200 fs, 700 fs and 1.67 ps laser pulses.

5.3.2 Atomistic modeling for single-shot AO-HIS

To obtain a more detailed insight into the roles of T_e and T_{ph} in single-shot AO-HIS, we use atomistic spin model to simulate the collective magnetic response in GdFeCo to linearly-polarized laser pulse. In atomistic calculation, each spin is coupled to the temperature of electron thermal bath. Due to small heat capacity of electrons, the action of ultrashort laser pulse first induces a rapid increase of electron temperature, followed by a slow heat exchange between electron and phonon thermal bath until the equilibrium is reached. The temporal evolution of T_e and T_{ph} are described by two temperature model (2TM). In the experiments, the small amount of Co is added to ensure the perpendicular magnetic anisotropy. Therefore, in order to save computation resources, only element Gd and Fe are taken into account for atomistic modelling.

Table I. Parameters of atomistic modeling for GdFeCo, taken from Ref. 171, 172

Electronic heat capacity	$C_e=\gamma T_e$, γ=300 Jm^{3}K^{-1}
Phonon heat capacity	$C_{ph}=3\times10^6$ Jm^3
Electron-phonon coupling	10^{18} W/m^{3}K
$J_{Gd\text{-}Gd}$	1.26×10^{-21} J
$J_{FeCo\text{-}FeCo}$	2.835×10^{-21} J
$J_{Gd\text{-}FeCo}$	-1.1×10^{-21} J
α_{Gd}，α_{FeCo}	0.01

Using atomistic model we can describe the evolution of the projection along z

(direction perpendicular to plane) of the Fe magnetization sublattice and the Gd magnetization sublattice as a function of time for various fluences as shown in Figure 5-7. From these graphs we can define if the single laser pulse leads to no switching as in the case 1 because the M_z components do not cross zero, or switching as in the case 2 since we could observe a clear inversion of the two M_z component, or a multidomain state as in the case 3 where the two M_z components are close to zero for a long time.

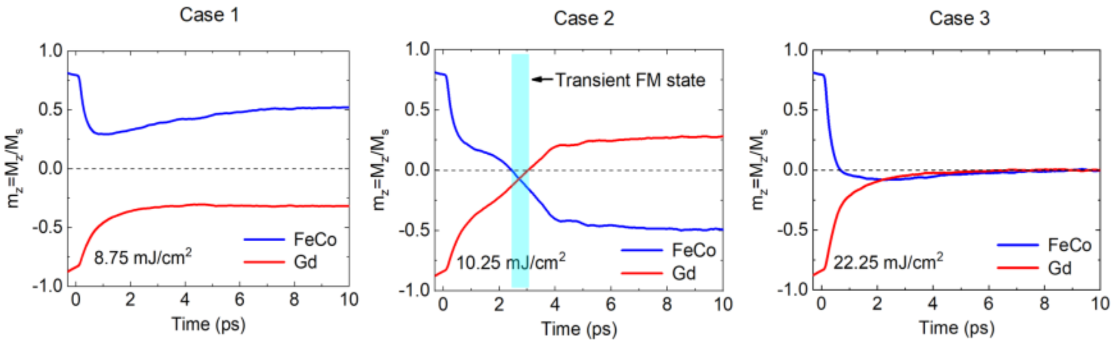

Figure 5-7 Temporal evolution of the normalized z component m_z of the FeCo magnetization sublattice and the Gd magnetization sublattice magnetization for Gd$_{24}$-(FeCo)$_{76}$ and a pulse duration of 50fs. M_z is the magnetization of sublattice M_z divided by saturated magnetization M_s (obtained at 0 K).

To simplify the presentation of the obtained results, we show in Figure 5-8 the variation of the z component of the FeCo sublattice magnetization $m_z(t)/m_z(0)$ at t=10 ps after the action of a single laser pulse for different fluences and pulse durations (50 fs, 500 fs, 1000 fs). We have chosen “10ps” to allow for magnetization recovery. In these figures, the value of $m_z(t)/m_z(0)$ below, above or equals to 100% corresponds to no switching, full switching or multidomain state, respectively. The fluence window for deterministic AOS is highlighted in pink. This type of calculation and of representation was first used by Moreno *et al.*[173] It is seen that the simulation results well reproduce main features of the experimental magnetization state diagram. First, for each pulse duration, AO-HIS takes place in a certain window of pulse fluence, ending with demagnetization as fluence increases. Moreover, the switching window becomes narrower for longer pulse duration and finally almost vanishes at 1.5ps which denotes the pulse duration threshold. Second, F_{Switch} obviously increases with pulse duration while threeF_{Multi} remains almost constant.

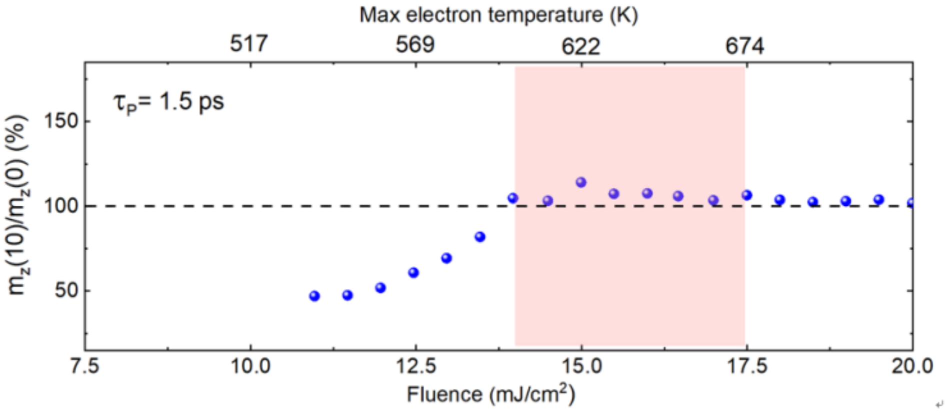

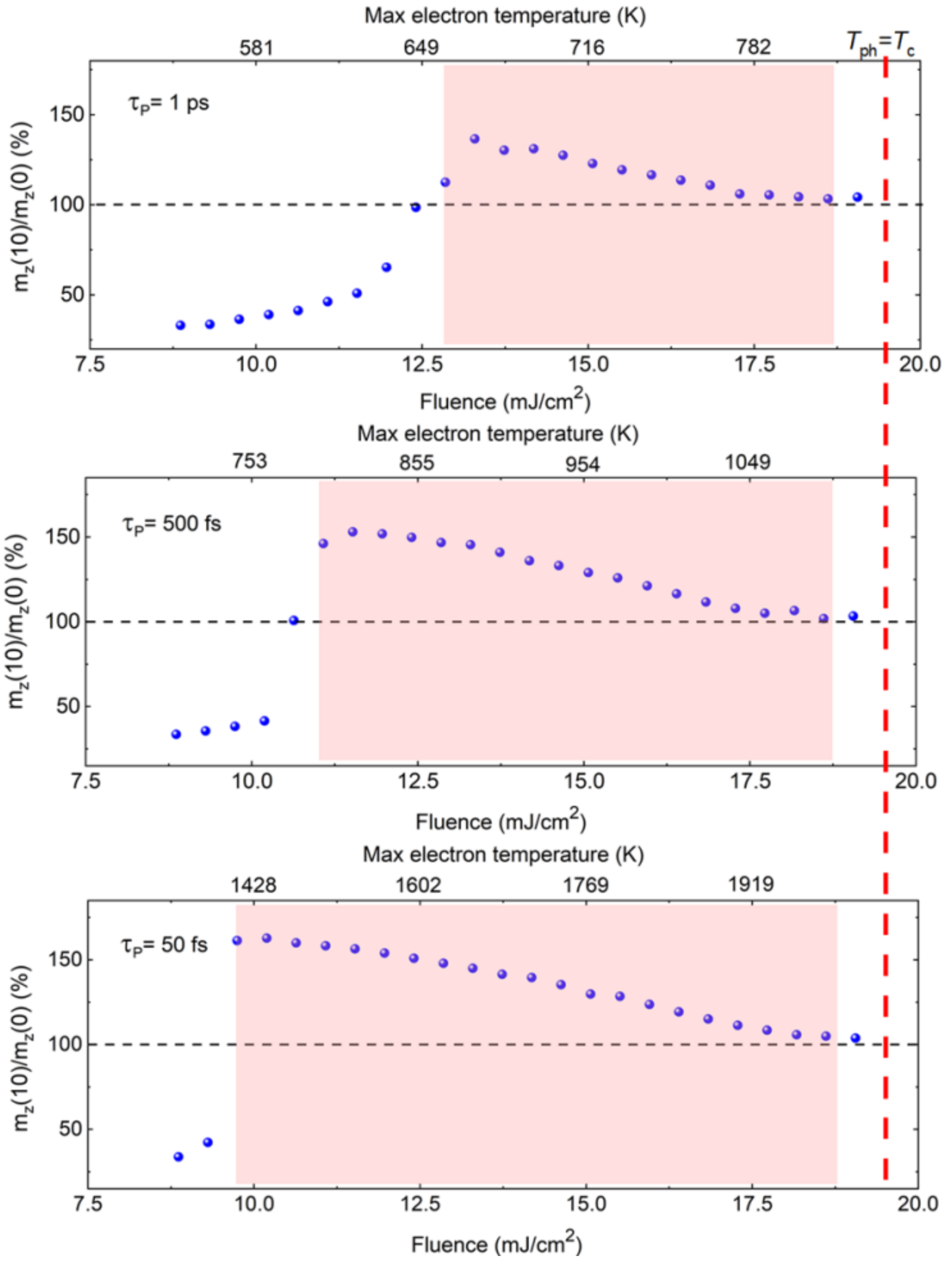

Figure 5-8 Variation of the *z* component of the FeCo sublattice magnetization 10 ps after exposure to a single pulse with different pump fluences, and a given pulse duration of (a) 50 fs, (b) 500 fs, and (c) 1 ps. The fluence window for deterministic AO-HIS is highlighted in pink. The maximum electron temperature T_e is indicated in the upper horizontal axis. The red dashed line indicates the fluence at which T_{ph} reaches T_c. T_e and T_{ph} are obtained using the two-temperature model (2TM).

Noting that the results obtained by choosing a shorter time t=5ps shows a similar trend as shown in Figure 5-9.

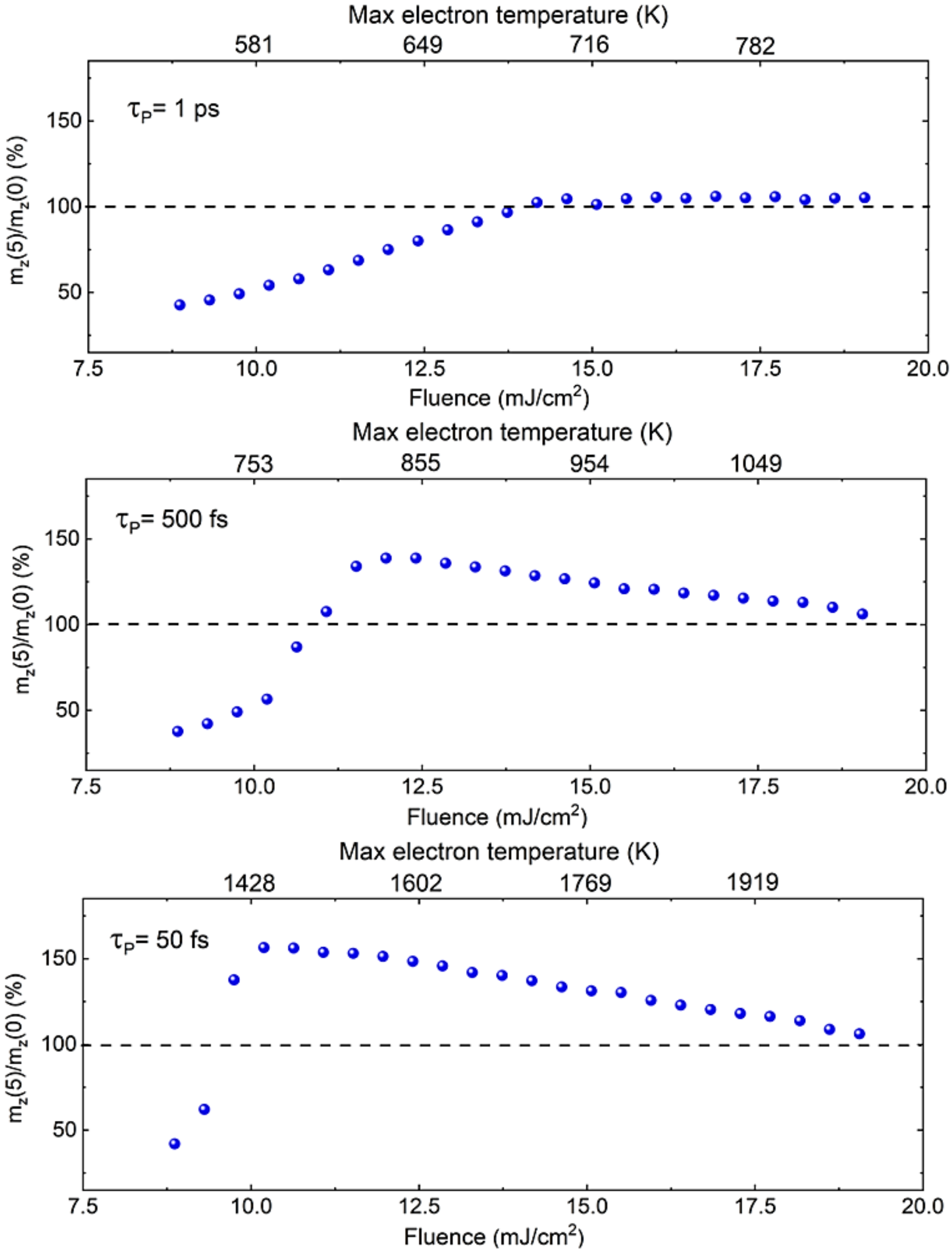

Figure 5-9 Variation of the magnetization of FeCo sublattice 5 ps after the pulse for different fluences and pulse durations of 50 fs, 500 fs and 1 ps.

To reveal the role of T_e in AO-HIS, we calculate peak T_e at several laser fluences which are indicated on the upper horizontal axis. It is seen that the peak T_e at critical switching fluence remarkably declines as pulse duration increases, from ~1409 K for τ=50fs to ~650 K for τ=1ps (for t=10ps). Importantly, the peak T_e for τ=1.5ps is around 632K which is well above the calculated curie temperature T_c (see Figure 5-10).

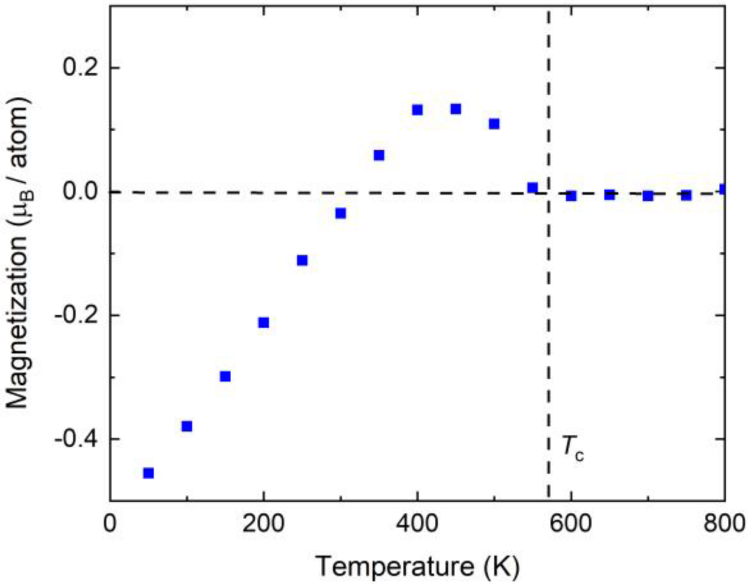

Fig. 5-10 Numerically calculated magnetization of $Gd_{24}(FeCo)_{76}$ as a function of temperature. T_c is estimated to be around 570 K.

On the other hand, we also calculated the temporal evolution of T_{ph} at demagnetization thresholds for different pulse durations as shown in Figure 5-11. Interestingly, peak phonon temperature T_{ph}^{max} shows almost no change as the pulse duration is varied. As a consequence, it depends mostly on the pulse energy and reaches T_c at a very similar fluence for different pulse durations.

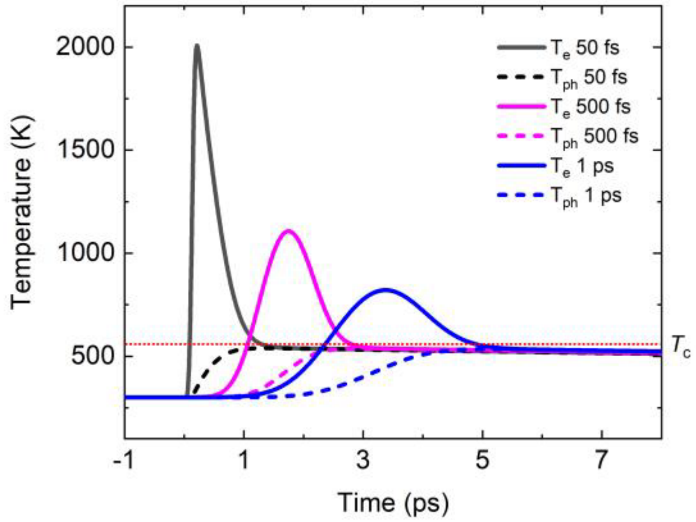

Figure 5-11 Temporal evolution of electron and phonon temperature at multidomain fluence thresholds for pulse durations of 50 fs, 500 fs and 1 ps.

We can then conclude that atomistic spin dynamics modeling of thermally induced magnetization switching can reproduce the AO-HIS state diagram in GdFeCo. It becomes very clear that shorter pulses are more energy efficient than longer pulses.

5.3.3 AO-HIS state diagrams as a function of Gd concentration

Figure 5-12 (a) and (b) present state diagrams for 20nm $Gd_x(FeCo)_{100-x}$ films, with $22 \leq x \leq 27$. For clarity, only the switching regions are highlighted by dashed lines. One can clearly see that the switching regions for different samples share a similar outline. However, obvious changes could be found as the composition is varied. First, the area of the switching region becomes larger, followed by a shrink as the Gd concentration increases. Importantly, it reaches the maximum at Gd concentration around 25%. According to the MOKE results, the magnetization compensation point x_{comp} is also located near 25 at room temperature. These observations therefore imply that for a given pulse duration, the widest fluence window for switching can be obtained at x_{comp}. Second, the maximum pulse duration τ_c also exhibits similar trends. A complete AOS is observed for laser pulse duration up to 3.8 ps for $Gd_{25}(FeCo)_{75}$. Finally, the F_{switch} shows different dependence on pulse duration for different alloy compositions. It exhibits a slower increase as the laser pulse broaden for GdFeCo with higher Gd concentration. In order to facilitate the analysis, the switching region in state diagram can be characterized by a right-triangle as shown in Figure 5-12 (c). The hypotenuse describes the dependence of F_{switch} on pulse duration. The other two sides indicate pulse duration threshold τ_c and maximum achievable switching window w_s, respectively. Apparently, the switching region is mathematically determined by w_s and slope k of hypotenuse. Moreover, τ_c could be roughly estimated as $w_s \bullet k$.

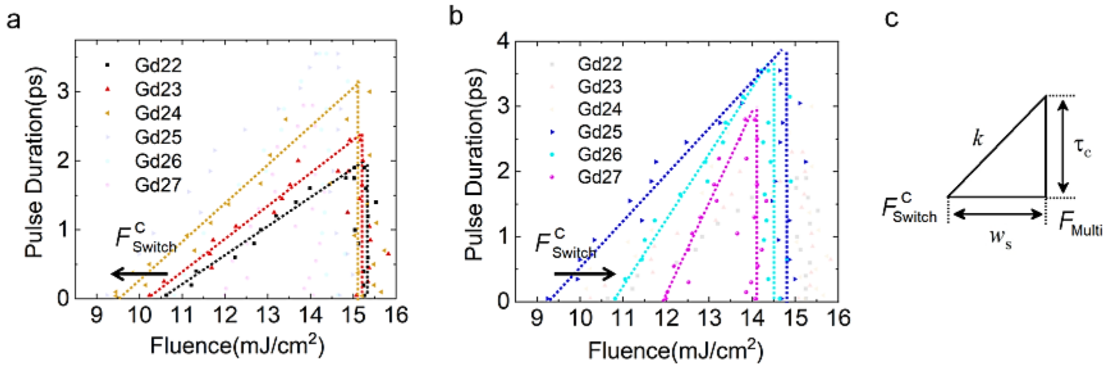

Figure 5-12 (a) and (b) Magnetization state diagram for Gdx(FeCo)100-x (22≤x≤27). The switching regions for different Gd concentration are highlighted by colored dashed lines. (c) Schematic illustration of switching region. w_s is the largest obtainable fluence switching window. k is the slope of switching region which describes the dependence of critical switching fluence FC-AOS on pulse duration.. τ_c is the critical pulse-duration threshold.

Figure 5-13 demonstrates $F_{\text{Switch}}^{\text{C}}$ (F_{switch} at 50fs), k and τ_c as a function of Gd concentration derived from the state diagrams. As shown in Figure 5-13 (a), $F_{\text{Switch}}^{\text{C}}$ strongly depends on the alloy composition and reaches the minimum around magnetization compensation point x_{comp}=25 (x_{comp}=24 for 10nm GdFeCo). On the other hand, F_{Multi} changes a little for different samples due to their similar curie temperature. As a consequence, the largest switching window is obtained around x_{comp}. The second crucial factor is k which describes the pulse duration dependence of F_{switch}. As displayed in Figure 5-13 (b), k monotonically increases with Gd concentration. Moreover, a larger k is obtained in 10nm GdFeCo for a given composition. Figure 5-13 (c) shows estimated τ_c as a function of Gd concentration. As mentioned above, for Co rich samples, both w_s and k increase with Gd concentration, which results in a dramatic increase in τ_c. For Gd rich ones, w_s rapidly decrease as Gd concentration increases, leading to a gradually decrease in τ_c. In addition, since *k* is larger in thinner samples, AO-HIS is observed in the 10 nm $Gd_{25}(FeCo)_{75}$ for pulse duration up to 11.8 ps which is much larger than that observed in 20 nm GdFeCo.

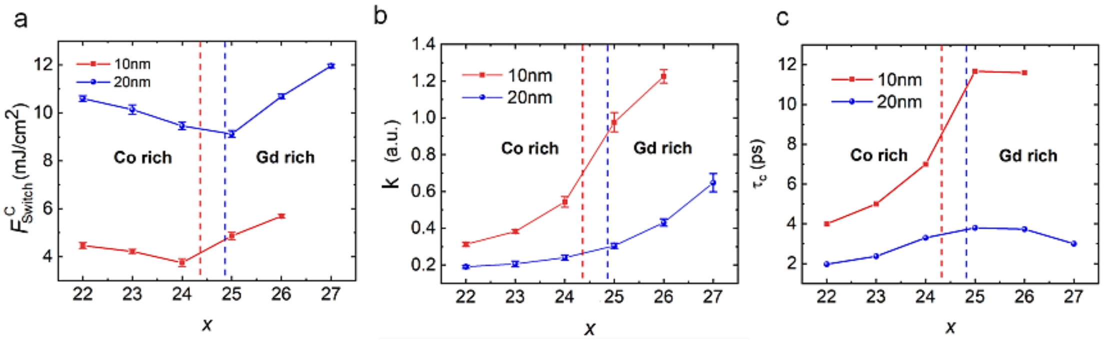

Figure 5-13 (a) The critical fluence F_{switch} for switching is plotted as a function of Gd concentration, measured using linearly polarized laser pulses with a pulse duration of 50fs. (b) Slope *k* as a function of Gd concentration, *k* is obtained by fitting of F_c for different pulse durations. (c) The pulse duration threshold τ_c as a function of Gd concentration. Only a fully demagnetized pattern is observed if $\tau>\tau_c$.

5.4 Summary and discussion

In this chapter, the effects of pulse characteristics on AO-HIS are described in detail. The studied GdFeCo samples have relatively large thicknesses and thus high critical switching fluences F_{switch}. High F_{switch} greatly minimizes the influence of errors such as fluence and pulse duration shift which are inevitable in laser related experiments, enabling us to precisely build AO-HIS state diagram for GdFeCo.

The experimental AO-HIS state diagrams allow to quickly visualize the laser pulses conditions (Fluence and Pulse duration) required for single-shot AO-HIS. We could then determine the evolution of the state diagrams as a function of the GdFeCo alloy concentration and thickness. This experimental study helps to address technologically relevant controversy and provides crucial guidelines to engineer energy efficient and technologically feasible single pulse all-optical switching of magnetization. Since it has already been shown that both single femto-second light pulse and single femto-second hot electron pulse can induce AO-HIS, the next issue is to generalize the effect to longer pulses to be technologically compatible with feasible electronics. This study allows answering two controversial questions: How can we optimize the material and the laser excitation to obtain a low energy AO-HIS and how can we observe AO-HIS for long pulse duration?

Concerning the first question, initial studies proposed that the existence of magnetization compensation temperature T_M is essential to achieve AO-HIS in ferrimagnets [174]. Later, it was proved that T_M is not indispensable while low net magnetization M_net greatly promotes AO-HIS [175]. However, a following theory work highlighted the importance of temperature derivative of the magnetization $dM_\mathrm{net}(T)/dT$ and it pointed out that the critical switching fluence is not the minimum at magnetization compensation point x_comp [176]. In this study, we experimentally demonstrate that $F_\mathrm{Switch}^\mathrm{C}$ significantly depends on the alloy composition and reaches a minimum around x_comp. We also find that $F_\mathrm{Switch}^\mathrm{C}$ scales with the layer thickness which can be ascribed to the variation of the laser absorption and the domain volume, indicating that a smaller thickness helps to develop energy-efficient AOS devices.

The second issue is about the pulse duration threshold τ_c. In this work, we reveal that τ_c is determined by $F_\mathrm{Switch}^\mathrm{C}$ which defines the base of the triangle-shaped switching region and the slope k which describes the dependence of F_Switch on pulse duration and F_Multi which seems to be given by the material Curie temperature. To obtain the largest τ_c we should just aim for a small $F_\mathrm{Switch}^\mathrm{C}$, a large F_Multi and a large k. However, k increases with Gd concentration whereas F_Multi decreases with Gd concentration and $F_\mathrm{Switch}^\mathrm{C}$ is minimum around the magnetic compensation alloy composition. Therefore, to maximize τ_c it is certainly interesting to be close to the compensation to obtain the smallest $F_\mathrm{Switch}^\mathrm{C}$, but it is also interesting to play with the relative Fe and Co concentration in order to increase the alloys Curie temperature and increase k. The influence of the sample thickness on AO-HIS is more complicated than it appears. From the state diagrams, the right-triangle shaped switching region for 10 nm GdFeCo possesses a much steeper slope than that for 20 nm GdFeCo, which results in a larger τ_c. This difference is likely caused by the nonuniform light absorption with respect to the sample depth. Xu *et al.* have calculated the heat absorption profile for similar 20 nm GdFeCo stacks [177]. They revealed that the electron temperature sharply decreases within the bottom 5 nm part of a 20 nm GdFeCo film when excited with a laser having a wavelength of 800 nm. Therefore, it needs much more energy to induce an overheating for thicker samples as pulse duration increases, leading to a smaller *k*.

Résumé du Chapitre 5

Dans ce chapitre, les effets des caractéristiques d'impulsion sur RTO-IH sont décrits en détail. Les échantillons de GdFeCo étudiés ont des épaisseurs relativement importantes et donc des fluences seuil de renversement élevées F_{switch}. High F_{switch} minimise considérablement l'influence des erreurs telles que la fluence et le décalage de la durée d'impulsion qui sont inévitables dans les expériences liées au laser, nous permettant de construire avec précision le diagramme d'état RTO-IH pour GdFeCo.

Les diagrammes d'état expérimentaux de l'RTO-IH permettent de visualiser rapidement les conditions d'impulsions laser (Fluence et Durée d'impulsion) requises pour l'RTO-IH avec une seule impulsion. Nous avons alors pu déterminer l'évolution des diagrammes d'état en fonction de la concentration et de l'épaisseur de l'alliage GdFeCo. Cette étude expérimentale permet d'aborder technologiquement la controverse pertinente et fournit des directives cruciales pour concevoir un renversement d'aimantation tout optique avec une seule impulsion, économe en énergie et faisable technologiquement. Puisqu'il a déjà été montré qu'une seule impulsion lumineuse femto-seconde et une seule impulsion d'électrons chauds femto-seconde peuvent induire l'RTO-IH, le prochain problème est de généraliser l'effet à des impulsions plus longues pour être technologiquement compatible avec l'électronique réalisable. Cette étude permet de répondre à deux questions controversées : Comment optimiser le matériau et l'excitation laser pour obtenir un RTO-IH de faible énergie et comment observer un RTO-IH pour une longue durée d'impulsion ?

Concernant la première question, les premières études ont proposé que l'existence d'une température de compensation d'aimantation T_M est essentielle pour atteindre l'RTO-IH dans les ferrimagnétiques [174]. Plus tard, il a été prouvé que la T_M n'est pas indispensable alors que la faible aimantation nette M_{net} favorise grandement l'RTO-IH [175]. Cependant, un travail théorique suivant a souligné l'importance de la dérivée de température de l'aimantation $dM_{net}(T)/dT$ et a souligné que la fluence seuil de renversement n'est pas le minimum au point de compensation d'aimantation x_{comp} [176]. Dans cette étude, nous démontrons expérimentalement que $F_{\mathrm{Switch}}^{\mathrm{C}}$ dépend de manière significative de la composition de l'alliage et atteint un minimum autour de x_{comp}. Nous constatons également que $F_{\mathrm{Switch}}^{\mathrm{C}}$ s'adapte à l'épaisseur de la couche qui peut être attribuée à la variation de l'absorption laser et du volume du domaine, indiquant qu'une épaisseur plus petite aide à développer des dispositifs RTO économes en énergie.

Le deuxième problème concerne le seuil de durée d'impulsion τ_{c}. Dans ce travail, nous révélons que τ_c est déterminé par $F_{\mathrm{Switch}}^{\mathrm{C}}$ qui définit la base de la région de retournement en forme de triangle et la pente k qui décrit la dépendance de F_{Switch} sur la durée d'impulsion et F_{Multi} qui semble être donnée par la température de Curie du matériau. Pour obtenir le plus grand τ_{c}, nous devrions simplement viser un petit $F_{\mathrm{Switch}}^{\mathrm{C}}$, un grand F_{Multi} et un grand k. Cependant, k augmente avec la concentration en Gd alors que F_{Multi} diminue avec la concentration en Gd et $F_{\mathrm{Switch}}^{\mathrm{C}}$ est minimum autour de la composition de l'alliage de compensation magnétique. Par conséquent, pour maximiser τ_{c} il est certes intéressant d'être proche de la compensation pour obtenir le plus petit $F_{\mathrm{Switch}}^{\mathrm{C}}$, mais il est également intéressant de jouer avec la concentration relative en Fe et en Co afin d'augmenter la température de Curie des alliages et d'augmenter k. L'influence de l'épaisseur de l'échantillon sur RTO-IH est plus compliquée qu'il n'y paraît. D'après les diagrammes d'état, la région de retournement en forme de triangle droit pour 10 nm de GdFeCo possède une pente beaucoup plus raide que celle pour 20 nm de GdFeCo, ce qui entraîne un τ_{c} plus grand. Cette différence est probablement causée par l'absorption de lumière non uniforme par rapport à la profondeur de l'échantillon. Xu *et al.* ont calculé le profil d'absorption de chaleur pour des empilements GdFeCo similaires de 20 nm [177]. Ils ont révélé que la température des électrons diminue fortement dans la partie inférieure de 5 nm d'un film de GdFeCo de 20 nm lorsqu'elle est excitée avec un laser ayant une longueur d'onde de 800 nm. Par conséquent, il faut beaucoup plus d'énergie pour induire une surchauffe pour des échantillons plus épais à mesure que la durée d'impulsion augmente, conduisant à un k plus petit.

6 A study on all-optical helicity-dependent switching state diagram in Co/Pt multilayers

6.1 Introduction

As described above, all-optical helicity-independent switching (AO-HIS) is mostly observed in Gd-based materials. For other ferrimagnetic and ferromagnetic materials, multiple pulses are needed to achieve a full magnetic reversal. Thus how to reduce the number of pulses required for AO-HDS attracts a lot of research interests. In 2017, R. Medapalli *et al*. presented a study on the magnetization dynamics of AO-HDS in Co/Pt multilayers [87]. They built magnetization state diagrams to determine the optimal pulse parameters for AO-HDS. The method can be described as following. First, using the static magneto-optical imaging technique, they first recorded a series of magneto-optical images after the sweeping of the laser beam with different fluences and pulse durations along the sample surface, as shown in Figure 6-1 (a) and (b). The swept regions were exposed to a 500 Hz pulsed laser beam moving at a speed of 1 μm/s. Second, they calculated the switching probability by measuring the mean intensity of swept regions in these pictures. Based on these results, they then constructed magnetization state diagram as a function of pulse width and fluence as shown in Figure 6-1 (d). They concluded that AO-HDS is the most efficient when the pulse duration is around 2.0 ps and the fluence is near 0.5 mJ/cm^2.

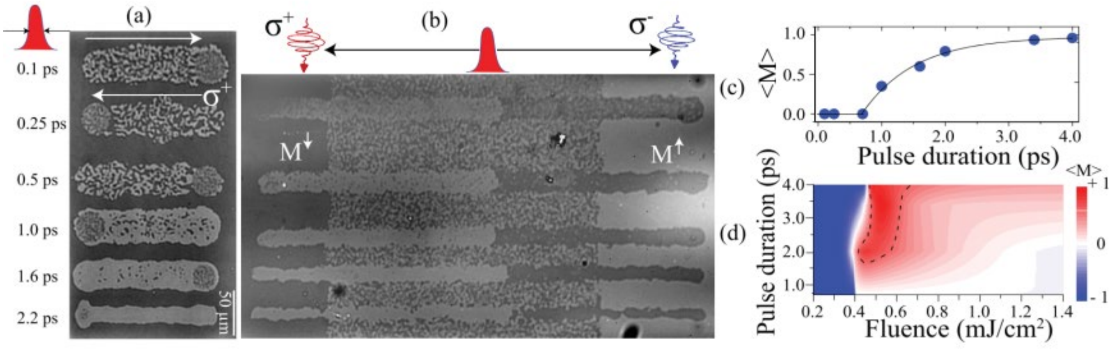

Figure 6-1 (a) Magneto-optical image of the Co/Pt thin film after action of sweeping of the circularly polarized pulsed laser beam along the sample surface. Each pattern corresponds to a specific duration of the pump pulse. (b) HD-AOS induced by a series of 4.0 ps optical pulses: Magneto-optical image of the domain patterns induced by slowly sweeping of the σ + (left) and σ − (right) circularly polarized pulsed laser beam along the sample surface. The bright and dark regions represent M↑ and M↓ states, respectively. The multidomain, demagnetizedlike, pattern between the uniform dark and bright regions was prepared by sweeping a 4.0 ps linearly (vertical) polarized laser beam. After the sweeps, irrespective of the initial magnetic state, the final state is determined by the helicity of the laser pulses. (c) Average value of the photo-induced magnetization <M> as a function of the pulse duration. The pump fluence and repetition rate is 0.5 mJ/cm2 and 500 Hz, respectively. (d) The state diagram as a function of the pulse duration and fluence. Extracted from [85].

Later, G. Kichin *et al.* demonstrated a similar work on the magnetization state diagram in Co/Pt multilayers [85]. Different from what Medapalli has done, the laser beam was kept static during the measurement. To obtain the state diagram, they first recorded a series of MOKE images for different pulse fluences and durations. Secondly, by assembling the cross-section lines of these pictures using IMAGE J, they obtained pictures which describe the evolution of magnetization state as fluence varies for different pulse durations, as shown in Figure 6-2 (a)-(e). Based on these results, they plot the state diagram which shows the dependence of magnetization state on pulse duration and fluence, as displayed in Figure 6-2 (f).

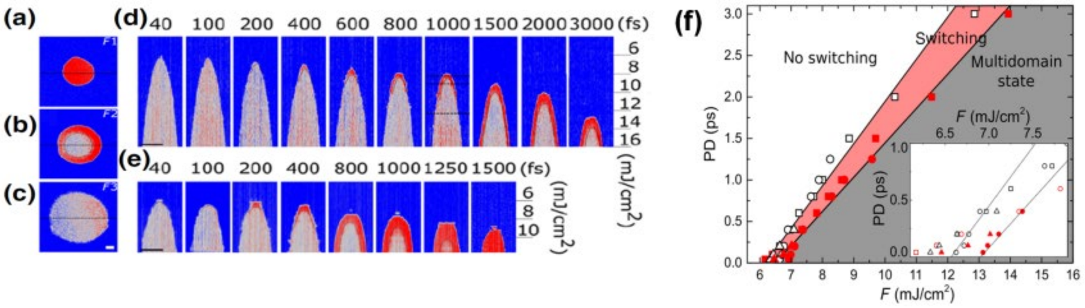

Figure 6-2 (a)–(c) Magneto-optical Kerr images obtained after exposing the sample to 600 laser pulses with a pulse duration of 1 ps, a $\sigma+$ polarization, and laser fluences of 8.3 mJ/cm^2 (a), 9.1 mJ/cm^2 (b), and 12.3 mJ/cm^2 (c) corresponding to the lines in (d). The red and blue contrasts correspond to opposite perpendicular magnetization directions. (e)–(d) Cross section of the laser excited area for laser fluences between 4 and 18 mJ/cm^2 and various pulse durations for a laser spot diameter of 104 μm (d) and 168 μm (e). (f) Magnetization state diagram as a function of the lase fluence, *F*, and the pulse duration, PD, for a circularly polarized static beam of different diameters illuminating a Co/Pt. For a given fluence, the maximum (minimum) pulse duration for which we have AO-HDS is plotted as filled (open) symbols. The inset shows a magnification of the diagram for the short pulse durations. Extracted from [85].

Afterwards, they try to see how the optimized laser parameters can facilitate the AO-HDS. They fabricated a 5-µm Co/Pt Hall cross and measured the evolution of the Hall voltage which is proportional to the out-of-plane component of magnetization. As can be seen in Figure 6-3, they demonstrated that a 10% switching can be obtained for an optimized circular polarized laser pulse, which is more efficient than previously reported results.

To date, AO-HDS state diagrams have only been reported in the above two works where different laser configurations are chosen. In this Chapter, a study on AO-HDS state diagram in Co/Pt multilayers using both static and sweeping laser beam is presented. Moreover, using time-resolved electrical measurement, the switching process in Co/Pt is demonstrated pulse by pulse, which provides a detailed insight into the physics behind AO-HDS.

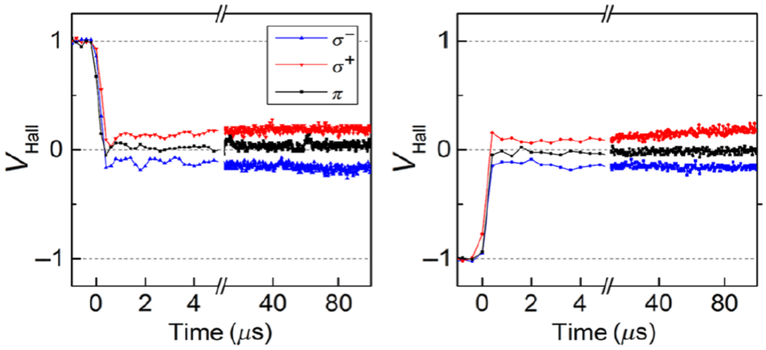

Figure 6-3 Normalized Hall voltage V_{Hall} showing the time-resolved magnetization dynamics of Co/Pt. The signal is normalized to the values measured for saturation of magnetization. The sample with initially saturated magnetization is excited with a single laser pulse of helicity $\sigma+$ (red), $\sigma-$ (blue), and linear π (black). The two graphs correspond to opposite initial magnetization directions. Switching time is estimated as less than 200 ns. Pulse duration is approximately equal to 2 ps. Laser fluence is approximately equal to 11 mJ/cm^2. Extracted from [85].

6.2 Samples and measurement set-up

The sample studied here is a multilayered stack of glass/Ta(3)/Pt(3.7)/Co(0.6)/Pt(3) (thicknesses in nm), grown on glass substrates by DC sputtering at room temperature. The bottom Ta layer improves adhesion of the structure to the glass substrate. Pt layers are inserted to induce a strong perpendicular magnetic anisotropy and the top Pt layer also prevents sample oxidation. For comparison purposes, the thickness of Co is consistent with previously reported works.

In order to get a detailed insight of the switching process in Co/Pt, we combine magneto-optical imaging and transport measurements. The studied device was fabricated through a two-step UV photolithography. First, the sample was patterned into a Hall cross. The portion that was not covered by photoresist was etched down to glass substrate by Ar+ ion. Second, the Hall cross was partially etched down to the bottom Pt layer while only material in the center of Hall cross has complete stack structure, as shown in Fig 6-4(a).

The optical excitation is performed using ultrashort laser pulses with a wavelength of 800 nm (1.55 eV), variable fluences and pulse durations. The FWHM (Full width at half maximum) of laser beam is about 70 μm, which is determined from the Gaussian fitting of the intensity profile. During the laser exposure, a high-frequency oscilloscope is used to record the Hall resistance via the anomalous Hall effect (AHE). Sampling is performed every 1 μs, which enables us to observe the multi-shot AOS process pulse by pulse. The injected DC current is 0.5mA, corresponding to a current density of 5.4×10^9 A/m^2.

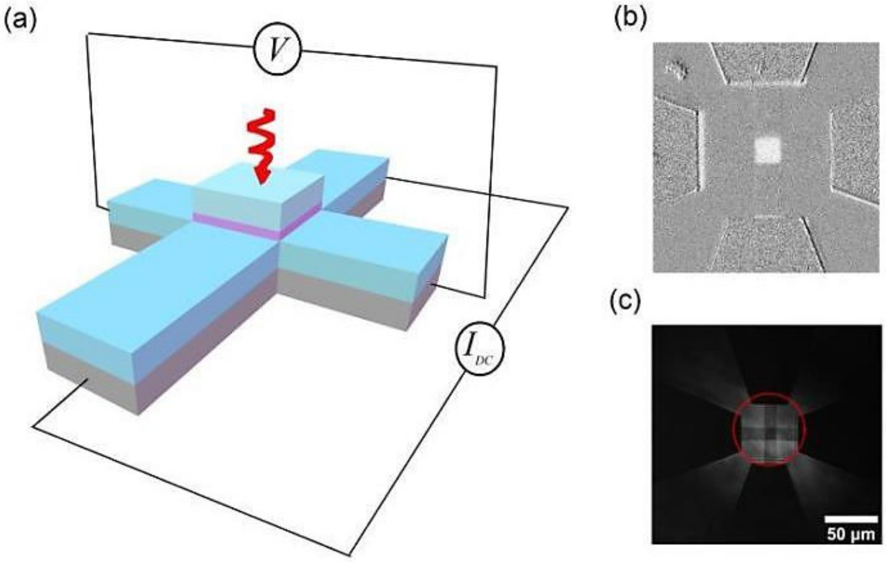

Figure 6-4. (a) Schematic view of set-up for Hall measurement. The studied device is a specially designed 9-μm-wide Hall cross which is partially etched down to the bottom Pt layer. Therefore, only the magnetic Co film in the central part of Hall cross is retained during the fabrication process. The Hall voltage is measured using an oscilloscope with a temporal resolution of 1 μs. (b) The back-ground corrected magneto-optical image of studied Hall cross. (c) Normal image of studied Hall cross illuminated by continuous laser pulses. The laser beam is fixed in the center of Hall cross, which is indicated by the red circle.

6.3 Results

6.3.1 AO-HDS state diagram

It was initially reported that a full magnetic reversal occurs only in a rim around the edge of a demagnetized area. Until recently, G. Kichin *et al.* showed that a complete AO-HDS can be achieved for static laser beam with suitable pulse duration and laser fluence [85]. Here, we make a comparison between magnetization state diagrams obtained using laser in both static and sweeping configurations as shown in Fig. 6-5.

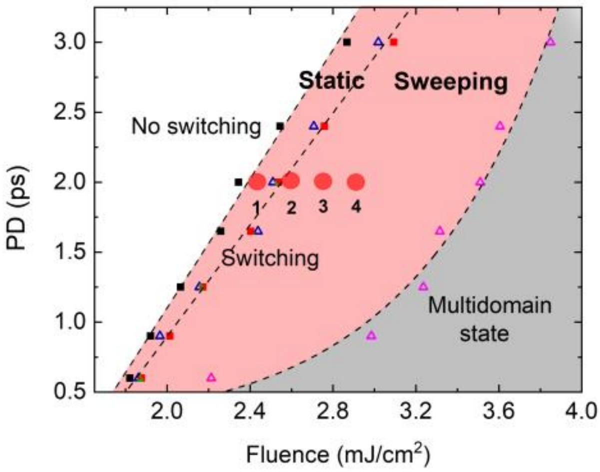

Figure. 6-5. Magnetization state diagram as a function of the laser fluence and the pulse duration (PD), obtained with a left circularly polarized (σ^-) laser beam in both static and sweeping laser configuration. For a given pulse duration, the black and red solid squares indicate, respectively, the critical fluence for switching F_c and minimum fluence required for multidomain-formation F_m in static laser configuration. In the case of sweeping laser beam, F_c and F_m are indicated by blue and pink hollow triangle, respectively. All the results were obtained in Co/Pt full film.

It is seen that an obvious switching window is achieved only for a pulse duration longer than 600 fs in both cases and the switching window becomes wider as the pulse duration increases. Importantly, two fingdings are demonstrated in the state diagram. First, the switching regions obtained in two laser configurations are adjacent to each other, meaning the demagnetizing fluence threshold for static laser is close to the switching fluence threshold for sweeping laser. Second, the switching window for sweeping laser beam is much wider than that for static laser beam. It is worth noting that a recent experimental work has demonstrated that sweeping the laser beam could lead to helicity-independent domain wall dragging [89]. This may explain the above results. To avoid effects coming from domain motion, in the following Hall measurements, the laser beam is fixed at the center of Hall cross. Moreover, a pulse duration of 2 ps is chosen in order for a large switching window.

6.3.2 AO-HDS process

As is seen from Figure 6-6(a)-(d), four different types of magnetic responses can be identified as the fluence increases from 2.4 mJ/cm^2 to 2.9 mJ/cm^2. The graphs in this figure show the time-dependent evolution of the normalized Hall resistance R_{AHE} of a 9-μm-wide Co/Pt Hall cross under the action of laser pulses with different polarizations. In addition, in each case, a magneto-optical image is taken for full film after exposure to laser pulses with same parameters in order to provide intuitive interpretation for the Hall measurement results.

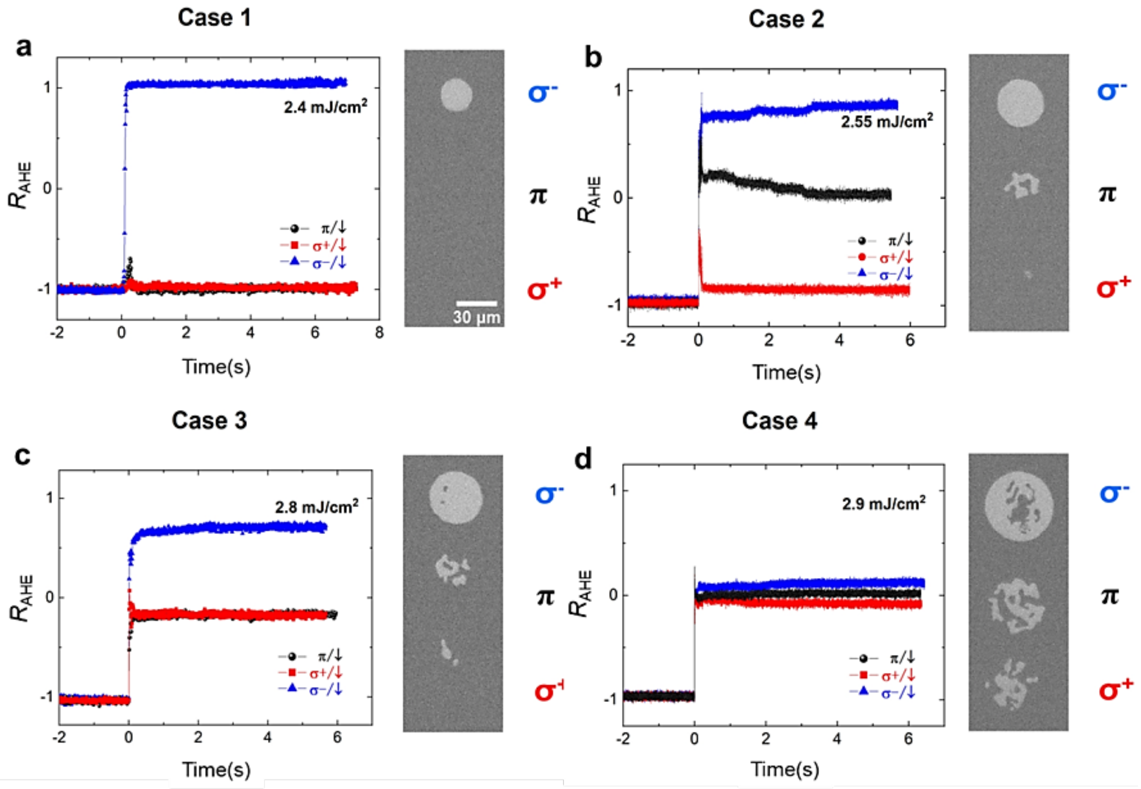

Figure 6-6 (a)-(d) Normalized Hall resistance showing the time-resolved magnetization dynamics of a specially designed 9-μm-wide Ta(3nm)/Pt(3.7nm)/Co(0.6)/Pt(3nm) Hall cross, under the action of laser pulses with a 5 kHz repetition rate and different fluences. In each case, a magneto-optical image is taken for full film after exposure to laser pulses with same parameters in order to provide intuitive interpretation for the Hall measurement results. The magnetization is initially saturated up before exposure to laser pulses every time.

In case 1, it is seen that a full magnetic switching is achieved under the action of 1500 consecutive σ^- laser pulses while the linear and σ^+ laser pulses have almost no impact on the magnetization. In case 2, 500 σ^- laser pulses fully switch the magnetization at a fluence of 2.55 mJ/cm^2. Unlike case 1, the linear light induces multiple-domain formation. As the fluence continues to increase, in case 3, the value of normalized R_{AHE} plateaus around 0.8 after the action of 500 σ^- laser pulses, which indicates occurrence of demagnetization. Moreover, both the linear and σ^+ laser pulses lead to a complete demagnetization. Case 4 shows that for an even larger fluence, independent of polarization, the laser pulses only induce a full demagnetization. According to the state diagram shown in Fig. 6-5, the complete reversal takes place between 2.4 mJ/cm^2 and 2.6 mJ/cm^2. Thus, we focus on the magnetic response in case 1 and case 2 in the following part.

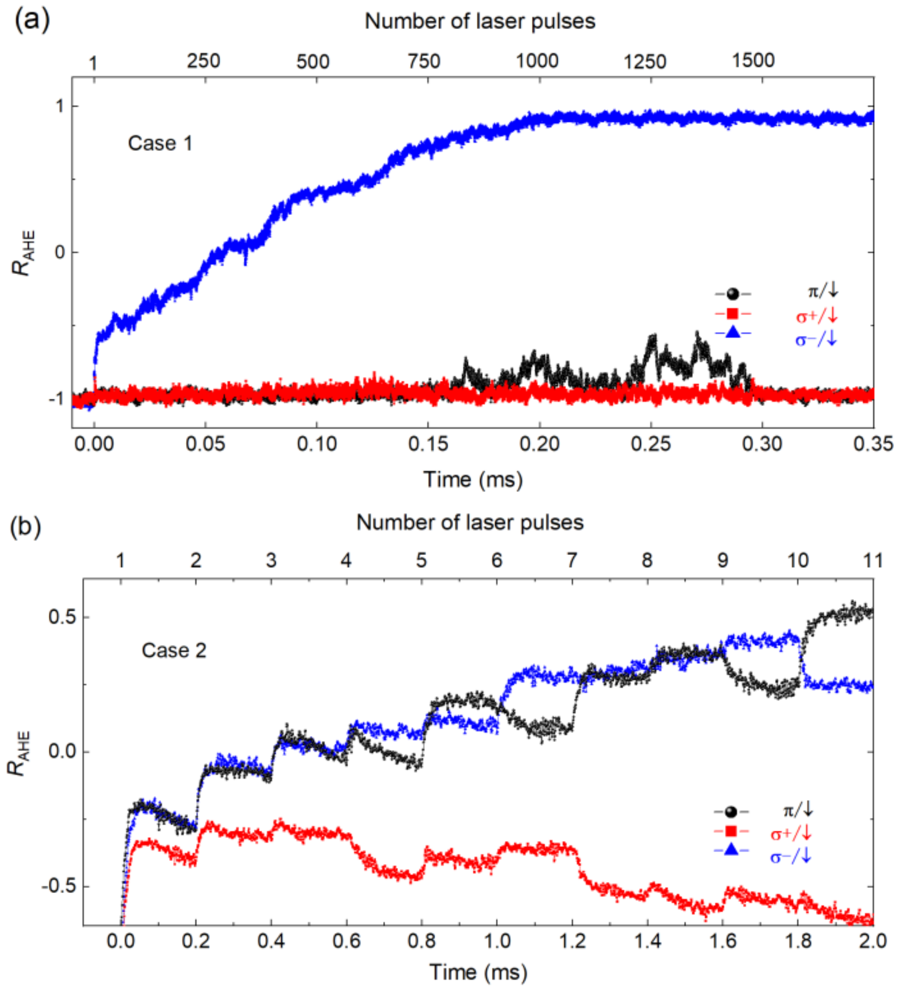

Figure 6-7 (a) The entire process of HD-AOS in Co/Pt under the action of 1500 consecutive laser pulses with a fluence of 2.4 mJ/cm^2. (b) The time-resolved magnetization dynamics in Co/Pt within the first 2 ms, under the action of 500 consecutive laser pulses with a fluence of 2.56 mJ/cm^2.

Figure 6-7 (a) represents the detailed process of multi-shot switching in case 1. It is seen that for a fluence of 2.4 mJ/cm^2, about 1000 pulses are required to reach a full reversal. Moreover, a steady switching process is exhibited, which implies a very uniform domain growth during the laser exposure. On the other hand, the linear and σ^+ light induce only small changes of Hall resistance which returns to its initial state after the laser stops. Figure 6-7 (b) presents the time evolution of R_{AHE} in case 2 within the first 2ms, it is seen that the magnetic responses for different polarizations all show a two-stages characteristic: the full demagnetization takes place within the first several pulses, followed by a slow helicity-dependent remagnetization. In contrast to case 1, linear and σ^+ light induce obvious changes of Hall resistance during the exposure.

To facilitate the observation of the entire evolution of R_{AHE} in case 2, we then performed the optical excitation using the same fluence with a low repetition rate of 500 Hz. As displayed in Figure 6-8, the final magnetization states corresponding to different polarizations are similar to those obtained at high repetition rate. In addition, it is interesting that under the action of σ^+ and σ^- pulses, large oscillations of Hall resistance are observed during the whole exposure process, which suggests that the demagnetization and remagnetization repeatedly take place. According to the state diagram shown above, the fluence used in case 2 lies near the boundary between the regions of switching and multidomain state, meaning the generation of nonnegligible heat. Therefore, we consider that, in case 2, the laser heating effect brings the spin temperature up to T_{c} (Curie temperature) within the first several pulses, leading to complete demagnetization. Afterwards, the helicity-dependent domain wall motion plays a leading role, which results in the remagnetization.

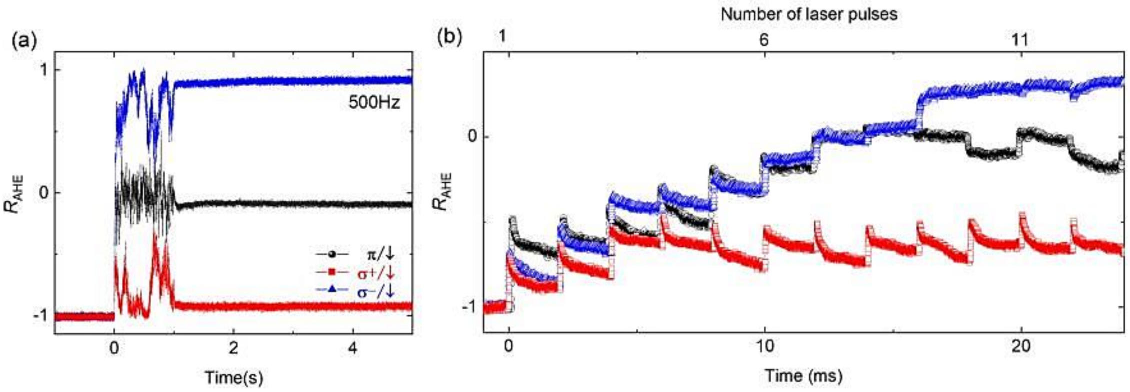

Figure 6-8 (a) Normalized Hall resistance showing the time-resolved magnetization dynamics of Co/Pt under the action of 500 consecutive laser pulses with a 500 Hz repetition rate and a fluence of 2.56 mJ/cm^2. (b) The time-resolved magnetization dynamics in Co/Pt within the first 25 ms, under the action of 500 consecutive laser pulses with a 500 Hz repetition rate and a fluence of 2.56 mJ/cm^2.

From the above results, we can conclude that AO-HDS is a cumulative process governed by domain nucleation and domain wall propagation, which is distinct from the case of AO-HIS. On the other hand, AO-HDS relies on the action of multiple laser pulses, which hinders its application in magnetic memory devices. Therefore how to realize AO-HIS with single laser pulse has attracted much attention recently. In 2018, Satoshi et al. first show that a Co layer can be switched with only one laser pulse by making use of the GdFeCo/Cu/Co/Pt structure [178]. This has been attributed to the ultrafast spin current flowing from GdFeCo to the Co. The generation of such a spin current is considered to arise from the superdiffusion of electrons induced by ultrashort laser pulses. Soon after, Quentin et al. and Junta et al. demonstrate similar results on GdFeCo/Spacer/Co [179,180]. Moreover they show that the magnetization of Co can be switched without inducing the switching of GdFeCo, which further confirm the presence of laser induced ultrafast spin current.

6.4 Summary and discussion

In this chapter, we first investigated the AO-HDS state diagrams in Co/Pt multilayers using both static and sweeping laser beam. The results show that the Co/Pt multilayers have a much wider switching window in sweeping laser configuration while a smaller one for static laser beam. Then we studied the process of AO-HDS pulse by pulse using time-resolved electrical measurement. A very uniform switching process was observed when the fluence is within the switching window; when the fluence is near the border between the regions of switching and multidomain state, a two-stage reversal can be identified. These results are remarkably different from Mohammad's work where Co/Pt demonstrates a two-stage reversal whatever the fluence is. In addition, we show that once circularly polarized laser pulses are used, demagnetization and remagnetization repeatedly take place, which is distinct from what Mohammad has shown. We attribute this to two factors. First, a specially designed Hall cross was used in this study. Only material in the center of Hall cross has Co layer. For conventional Hall cross, the domain walls which are located away from laser spot can possibly move towards the center of device, inducing unwanted variations of Hall resistance. Second, according to the state diagram presented above, an obvious switching window can be obtained only for a pulse duration longer than 600 fs. However, a 30 fs pulse duration was used in Mohammad's work. For such short pulses, the laser beam has to be kept away from the center of Hall cross to avoid demagnetization.

Résumé du Chapitre 6

Dans ce chapitre, nous avons d'abord étudié les diagrammes d'état RTO-IH dans des multicouches Co/Pt en utilisant à la fois un faisceau laser statique et un faisceau laser à balayage. Les résultats montrent que les multicouches Co/Pt ont une fenêtre de retournement beaucoup plus large en configuration laser à balayage tandis qu'une fenêtre plus petite pour le faisceau laser statique. Ensuite, nous avons étudié le processus d'RTO-IH impulsion par impulsion en utilisant une mesure électrique résolue en temps. Un processus de retournement très uniforme a été observé lorsque la fluence se situe dans la fenêtre de retournement ; lorsque la fluence est proche de la frontière entre les régions de retournement et d'état multidomaine, une inversion en deux étapes peut être identifiée. Ces résultats sont remarquablement différents des travaux de Mohammad où Co/Pt démontre une inversion en deux étapes quelle que soit la fluence. De plus, nous montrons qu'une fois que des impulsions laser polarisées circulairement sont utilisées, la démagnétisation et la remagnétisation ont lieu à plusieurs reprises, ce qui est distinct de ce que Mohammad a montré. Nous attribuons cela à deux facteurs. Premièrement, une croix de hall spécialement conçue a été utilisée dans cette étude. Seul le matériau au centre de la croix de Hall a une couche de Co. Pour la croix de Hall conventionnelle, les parois de domaine qui sont situées à l'écart du spot laser peuvent éventuellement se déplacer vers le centre du dispositif, induisant des variations indésirables de la résistance de Hall. Deuxièmement, selon le diagramme d'état présenté ci-dessus, une fenêtre de retournement évidente ne peut être obtenue que pour une durée d'impulsion supérieure à 600 fs. Cependant, une durée d'impulsion de 30 fs a été utilisée dans le travail de Mohammad. Pour des impulsions aussi courtes, le faisceau laser doit être éloigné du centre de la croix de hall pour éviter la démagnétisation.

CONCLUSIONS AND PERSPECTIVES

In this thesis, I present studies on the current-induced magnetization precession and laser-induced magnetization switching, which are promising to be used for wireless communication and information storage, respectively.

(1) To study the magnetization precession induced by spin current, we fabricated both in-plane and out-of-plane STNOs and then measured their microwave output under different conditions. We demonstrated that the amplitude and frequency of microwave emission can be effectively modulated by changing the injected current, showing potential of STNOs for ASK and FSK. Moreover, we show that a wider frequency tuning range is achieved under a stronger magnetic field while a higher amplitude tunability for current is obtained under a smaller magnetic field. These results provide important guidelines for application of STNOs in wireless transmission.

Then we would like to point out that, with the growing number of IoT devices, the research on p-MTJ is increasingly meaningful due to their potential of being used as a multifunctional standardized stack (MSS) that can provide three functionalities: magnetic memories devices, magnetic sensor and RF oscillator. A suitable MSS is expected to greatly reduce the cost of production. In this thesis, we studied the dynamics of p-MTJs with a doubled MgO/CoFeB interface free layer and a single atom thick W insertion. Such stacks show high a PMA, a large TMR and a low threshold current, which is an ideal candidate for MSS. Currently, the biggest problem for p-MTJs to be used for microwave generation is its low output power (~nW in most cases). In such context, mutual synchronization of STNOs attracts a lot of interest and two routes have been proposed. First, J. Grollier *et al.* demonstrated that the serially connected STNOs can be synchronized using their shared current. Later, in 2009, it was demonstrated that four vortex-based STNOs could synchronize due to the presence of long-range dipolar stray microwave fields generated during magnetization precession. Unfortunately, these methods are only capable to synchronize a few STNOs, their output power are still so small compared with conventional VCO.

Hence, how to realize synchronization of large arrays of STNOs remains a great cHallenge.

(2) To study the magnetic response to ultrafast laser pulses, we built state diagrams for GdFeCo and Co/Pt thin films, showing AO-HIS and AO-HDS respectively. Concerning AO-HIS in GdFeCo, we showed that the switching windows strongly depend on pulse duration. Moreover, the Gd concentration has a significant influence on switching fluence threshold while the demagnetizing fluence threshold remains almost constant. Using atomistic spin model, we showed that the electron temperature and lattice temperature have different pulse duration dependence, which well explain the AO-HIS state diagram. For Co/Pt, the state diagram is very different from that in GdFeCo. The window for AO-HDS becomes wider as the pulse duration increases. Although we cannot explain all the observed results, these findings still provide important guidelines to optimize the material properties and the laser characteristics to obtain energy-efficient switching.

AOS is promising for development of ultra-fast magnetic memory. Since AO-HDS normally requires hundreds of laser pulses to achieve a complete magnetic switching, Materials showing AO-HIS appear to be better candidates. As mentioned in this thesis, to induce ultrafast demagnetization, the pulse duration used to trigger AO-HIS should be within a certain range. Moreover, the switching window rapidly decreases as the pulse duration increases. Therefore, femtosecond laser pulses are preferred for AO-HIS. However, so far the semiconductor laser sources which are small and easily integrated are only capable of generating laser pulses with picosecond temporal width. Our work shows that, to maximize the pulse duration threshold, we should just aim for a small $F_{\mathrm{Switch}}^{\mathrm{C}}$, a large F_{Multi} and a large k. These results provide a clear route to optimize materials for picosecond AO-HIS.

CONCLUSIONS ET PERSPECTIVES

Dans ce manuscrit, je présente des études sur la précession de l'aimantation induite par courant électrique, prometteuse pour la communication sans fil, et le renversement de l'aimantation par laser, à fort potentiel dans le stockage de l'information.

(1) Pour étudier la précession de l'aimantation par courant de spin, nous avons fabriqué à la fois des NOTS dans le plan et hors du plan et avons mesuré la microonde résultante sous différente conditions. Nous avons démontré que l'amplitude et la fréquence des émissions microondes peut être efficacement modulé en faisant varier les caractéristiques du courant injecté. Cela montre le potentiel des NOTS pour la MDF et la MDA. De plus, nous avons prouvé qu'une plage de fréquence d'utilisation élargie est obtenue quand le champ magnétique est accru alors qu'un champ magnétique plus faible offre une plus large gamme d'amplitudes. Ces résultat servent de lignes directrices pour l'application des NOTS dans la transmission sans fil.

Ensuite nous voudrions insister sur le fait qu'avec le nombre croissant de dispositif pour l'IdO, la recherche sur le p-JTM gagne de plus en plus en pertinence du fait de leur utilisation potentiel en tant qu'élément multifonctionnel standardisé (EMS) pouvant remplir trois fonctions : mémoire magnétique, capteur magnétique et oscillateur RF. Un EMS idéal a un coût de production réduit. Dans ce manuscrit, nous avons étudier la dynamique des p-JTMs avec une couche libre ayant deux interfaces MgO/CoFeB et une insertion de W de la taille d'un atome. De tels empilements ont une grande PMA, une forte TMR et un faible courant seuil . Ce sont des candidats parfaits pour les EMS. Actuellement les plus gros problème des p-JTMs pour une génération de microondes est leur faible puissance de sortie (~nW dans la plupart des cas). Dans un tel contexte, la synchronisation mutuelle des NOTS a suscité beaucoup d'intérêt et deux possibilités ont émergé. Premièrement, J. Grollier *et al.* ont démontré que des NOTS connectés en série peuvent être synchronisés en utilisant leur courant partagé. Plus tard, en 2009, il a été démontré que 4 NOTS à base de vortex pourraient se synchroniser grâce aux champs dipolaires microondes à longue portée générés pendant la précession de l'aimantation. Malheureusement, ces méthodes sont seulement capable de synchroniser quelques NOTS, leur puissance de sortie reste petite comparée à l'oscillateur commandé en tension conventionnel.

Ainsi la synchronisation d'un grand nombre de NOTS reste un immense défi à relever.

(2) Pour étudier la réponse magnétique à des impulsions laser ultrarapides, nous avons construit un diagramme d'état pour le GdFeCo et le Co/Pt, respectivement pour le RTO-IH et le RTO-DH. En ce qui concerne le RTO-IH dans le GdFeCo, nous avons montré que la fenêtre de retournement dépend fortement de la durée de l'impulsion. De plus, la concentration de Gd a une influence significative sur la fluence seuil de retournement alors que la fluence seuil de désaimantation reste quasiment inchangée. En utilisant un modèle de spin atomistique, nous avons montré que la température électronique et la température du réseau évoluent différemment selon la durée d'impulsion, ce qui explique le diagramme d'état de RTO-IH. Pour le Co/Pt, le diagramme d'état est très différent de celui du GdFeCo. La fenêtre de fluence pour le RTO-DH s'élargit à mesure que la durée d'impulsion augmente. Bien que nous ne puissions pas expliquer tous les résultats observés, ces trouvailles sont primordiales pour optimiser les propriétés du matériau et du laser afin de réduire la consommation énergétique.

Le RTO est prometteur pour le développement de mémoires magnétiques ultrarapides. Puisque le RTO-DH requiert en principe des centaines d'impulsions laser pour obtenir un retournement complet, les matériaux sujets au RTO-IH apparaissent comme des meilleurs candidats. Comme nous l'avons mentionné dans cet ouvrage, afin d'obtenir le RTO-IH, la durée d'impulsion déclenchant la désaimantation ultrarapide doit être comprise dans un certain intervalle. De plus, la fenêtre de fluence de retournement se rétrécit rapidement quand la durée d'impulsion augmente. Il est donc préférable d'appliquer des impulsions de laser femtoseconde pour obtenir le RTO-IH. Cependant les source laser semi-conductrices sont à ce jour seulement capable de générer des impulsions durant au minimum quelques picosecondes. Notre travail montre que pour maximiser la durée d’impulsion seuil, il faut chercher à obtenir un petit $F_{\mathrm{Switch}}^{\mathrm{C}}$, un large F_{Multi} et un large k. Ces résultats nous fournissent une feuille de route claire pour l’optimisation des matériaux pour le RTO-IH picoseconde.

References

[1] Kumar, A., Shwe, H.U., Wong, K.J. and Chong, P.H.J, “Location-Based Routing Protocols for Wireless Sensor Networks: A Survey,” Wireless Sensor Network, 9, 25-72 (2017). http://dx.doi.org/10.4236/wsn.2017.91003

[2] D. Estrin and R. Govindan, “Next century cHallenges: scalable coordination in sensor networks”. MobiCom, Seattle, WA, pp. 263-270 (1999).

[3] Svetoslav Atanasov, “An overview of wireless communication technologies used in wireless sensor networks,” International Scientific Conference eRA-8, September 2009. DOI: 10.13140/2.1.4440.6720

[4] Team L, Alstrin L, Goker T, et al. 2.0 TECHNOLOGY ROADMAP 2.0 PARTICIPANTS [C]. Information Storage Industry Consortium （INSI）, 2015.

[5] Kiselev, S. I., Sankey, J. C., Krivorotov, I. N., Emley, N. C., Schoelkopf, R. J., Buhrman, R. A., & Ralph, D. C. (2003). Microwave oscillations of a nanomagnet driven by a spin-polarized current. *nature*, *425*(6956), 380-383.

[6] Rippard, W. H., Pufall, M. R., Kaka, S., Russek, S. E., & Silva, T. J. (2004). Direct-current induced dynamics in C o 90 F e 10/N i 80 F e 20 point contacts. *Physical review letters*, *92*(2), 027201.

[7] Maehara, H., Kubota, H., Suzuki, Y., Seki, T., Nishimura, K., Nagamine, Y., ... & Yuasa, S. (2013). Large emission power over 2 μW with high Q factor obtained from nanocontact magnetic-tunnel-junction-based spin torque oscillator. *Applied Physics Express*, *6*(11), 113005.

[8] Stanciu, C. D. et al. All-Optical Magnetic Recording with Circularly Polarized Light. Physical Review Letters **99,** 047601 (July 2007)

[9] A. Purbawati *et al*., Appl. Phys. Lett. 108, 122402 (2016)

[10] Radu, I. *et al.* Transient ferromagnetic-like state mediating ultrafast reversal of

antiferromagnetically coupled spins. *Nature* 472, 205 (2011).

[11] Ostler, T. A. et al. *Nat. Commun.* 3, 666 (2012).

[12] Gorchon, J. *et al.* Role of electron and phonon temperatures in the helicity-independent all-optical switching of GdFeCo. *Physical Review B* 94, 184406 (2016).

[13] Zhang, B. *et al.* Energy-Efficient Domain-Wall Motion Governed by the Interplay of Helicity-Dependent Optical Effect and Spin-Orbit Torque. *Phys. Rev. Appl.* 11, 1 (2019).

[14] Zhang, B. *et al.* Domain-wall motion induced by spin transfer torque delivered by helicity-dependent femtosecond laser. *Phys. Rev. B* 99, 1–6 (2019).

[15] Mangin, S. *et al.* Engineered materials for all-optical helicity-dependent magnetic switching. *Nature Materials* 13, 286–292 (2014).

[16] Thomson, W. (1857). XIX. On the electro-dynamic qualities of metals:—Effects of magnetization on the electric conductivity of nickel and of iron. *Proceedings of the Royal Society of London*, (8), 546-550.

[17] McGuire, T., & Potter, R. L. (1975). Anisotropic magnetoresistance in ferromagnetic 3d alloys. *IEEE Transactions on Magnetics*, *11*(4), 1018-1038.

[18] Campbell, I. A. (1970). Hall effect and resistivity anisotropy in ni alloys. *Physical Review Letters*, *24*(6), 269.

[19] De Ranieri, E., Rushforth, A. W., Výborný, K., Rana, U., Ahmad, E., Campion, R. P., ... & Jungwirth, T. (2008). Lithographically and electrically controlled strain effects on anisotropic magnetoresistance in (Ga, Mn) As. *New Journal of Physics*, *10*(6), 065003.

[20] E. Grochowski and R. E. Fontana Jr, "Future technology cHallenges for nand flash and hdd products," Flash Memory Summit, 2012.

[21] Grünberg, P. E. T. E. R., Schreiber, R., Pang, Y., Brodsky, M. B., & Sowers, H. (1986). Layered magnetic structures: Evidence for antiferromagnetic coupling of

Fe layers across Cr interlayers. *Physical review letters*, *57*(19), 2442.

[22] Binasch, G., Grünberg, P., Saurenbach, F., & Zinn, W. (1989). Enhanced magnetoresistance in layered magnetic structures with antiferromagnetic interlayer exchange. *Physical review B*, *39*(7), 4828.

[23] Baibich, M. N., Broto, J. M., Fert, A., Van Dau, F. N., Petroff, F., Etienne, P., ... & Chazelas, J. (1988). Giant magnetoresistance of (001) Fe/(001) Cr magnetic superlattices. *Physical review letters*, *61*(21), 2472.

[24] Parkin, S. S. P., More, N., & Roche, K. P. (1990). Oscillations in exchange coupling and magnetoresistance in metallic superlattice structures: Co/Ru, Co/Cr, and Fe/Cr. *Physical review letters*, *64*(19), 2304.

[25] Dieny, B., Speriosu, V. S., Parkin, S. S., Gurney, B. A., Wilhoit, D. R., & Mauri, D. (1991). Giant magnetoresistive in soft ferromagnetic multilayers. *Physical Review B*, *43*(1), 1297.

[26] Berkowitz, A. E., Mitchell, J. R., Carey, M. J., Young, A. P., Zhang, S., Spada, F. E., ... & Thomas, G. (1992). Giant magnetoresistance in heterogeneous Cu-Co alloys. *Physical Review Letters*, *68*(25), 3745.

[27] Xiao, J. Q., Jiang, J. S., & Chien, C. L. (1992). Giant magnetoresistance in nonmultilayer magnetic systems. *Physical Review Letters*, *68*(25), 3749.

[28] Pratt Jr, W. P., Lee, S. F., Slaughter, J. M., Loloee, R., Schroeder, P. A., & Bass, J. (1991). Perpendicular giant magnetoresistances of Ag/Co multilayers. *Physical review letters*, *66*(23), 3060.

[29] Parkin, S. S. P., Li, Z. G., & Smith, D. J. (1991). Giant magnetoresistance in antiferromagnetic Co/Cu multilayers. *Applied Physics Letters*, *58*(23), 2710-2712.

[30] Piraux, L., George, J. M., Despres, J. F., Leroy, C., Ferain, E., Legras, R., ... & Fert, A. (1994). Giant magnetoresistance in magnetic multilayered

nanowires. *Applied Physics Letters*, *65*(19), 2484-2486.

[31] Dinia, A., & Ounadjela, K. (1995). Temperature dependence of the magnetoresistance in Co/Ru sandwich and superlattice structures. *Journal of magnetism and magnetic materials*, *146*(1-2), 66-76.

[32] Dieny, B., Speriosu, V. S., Metin, S., Parkin, S. S., Gurney, B. A., Baumgart, P., & Wilhoit, D. R. (1991). Magnetotransport properties of magnetically soft spin-valve structures. *Journal of Applied Physics*, *69*(8), 4774-4779.

[33] Kowalska, E. (2018). *Current-induced dynamics in hybrid geometry MgO-based spin-torque nano-oscillators* (Doctoral dissertation, Technische Universität Dresden).

[34] Valet T, Fert A. Theory of the perpendicular magnetoresistance in magnetic multilayers[J]. Physical Review B, 1993, 48(10): 7099.

[35] Julliere, M. (1975). Tunneling between ferromagnetic films. *Physics letters A*, *54*(3), 225-226.

[36] Miyazaki, T., & Tezuka, N. (1995). Giant magnetic tunneling effect in Fe/Al2O3/Fe junction. *Journal of magnetism and magnetic materials*, *139*(3), L231-L234.

[37] Mathon, J., & Umerski, A. (2001). Theory of tunneling magnetoresistance of an epitaxial Fe/MgO/Fe (001) junction. *Physical Review B*, *63*(22), 220403.

[38] Butler, W. H., Zhang, X. G., Schulthess, T. C., & MacLaren, J. M. (2001). Spin-dependent tunneling conductance of Fe| MgO| Fe sandwiches. *Physical Review B*, *63*(5), 054416.

[39] Yuasa, S., Nagahama, T., Fukushima, A., Suzuki, Y., & Ando, K. (2004). Giant room-temperature magnetoresistance in single-crystal Fe/MgO/Fe magnetic tunnel junctions. *Nature materials*, *3*(12), 868-871.

[40] Parkin, S. S., Kaiser, C., Panchula, A., Rice, P. M., Hughes, B., Samant, M., & Yang, S. H. (2004). Giant tunnelling magnetoresistance at room temperature with

MgO (100) tunnel barriers. *Nature materials*, *3*(12), 862-867.

[41] Ikeda, S., Hayakawa, J., Ashizawa, Y., Lee, Y. M., Miura, K., Hasegawa, H., ... & Ohno, H. (2008). Tunnel magnetoresistance of 604% at 300 K by suppression of Ta diffusion in Co Fe B∕ Mg O∕ Co Fe B pseudo-spin-valves annealed at high temperature. *Applied Physics Letters*, *93*(8), 082508.

[42] Slonczewski, J. C. (1996). Current-driven excitation of magnetic multilayers. *Journal of Magnetism and Magnetic Materials*, *159*(1-2), L1-L7.

[43] Berger, L. (1996). Emission of spin waves by a magnetic multilayer traversed by a current. *Physical Review B*, *54*(13), 9353.

[44] Gilbert, T. L. (2004). A phenomenological theory of damping in ferromagnetic materials. *IEEE transactions on magnetics*, *40*(6), 3443-3449.

[45] Landau, L. A. L. E., & Lifshitz, E. (1992). On the theory of the dispersion of magnetic permeability in ferromagnetic bodies. In *Perspectives in Theoretical Physics* (pp. 51-65). Pergamon.

[46] Slonczewski, J. C. (1999). Excitation of spin waves by an electric current. *Journal of Magnetism and Magnetic Materials*, *195*(2), L261-L268.

[47] Slonczewski, J. C. (2002). Currents and torques in metallic magnetic multilayers. *Journal of magnetism and magnetic materials*, *247*(3), 324-338.

[48] Ralph, D. C., & Stiles, M. D. (2008). Spin transfer torques. *Journal of Magnetism and Magnetic Materials*, *320*(7), 1190-1216.

[49] Houssameddine, D., Ebels, U., Delaët, B., Rodmacq, B., Firastrau, I., Ponthenier, F., ... & Dieny, B. (2007). Spin-torque oscillator using a perpendicular polarizer and a planar free layer. *Nature materials*, *6*(6), 447-453.

[50] Bai, X. (2018). *Micromagnetic Modeling of Thin Film Segmented Medium for Microwave-Assisted Magnetic Recording* (Doctoral dissertation, Carnegie Mellon University).

[51] Motti, F., Vinai, G., Petrov, A., Davidson, B. A., Gobaut, B., Filippetti, A., ... & Torelli, P. (2018). Strain-induced magnetization control in an oxide multiferroic heterostructure. *Physical Review B*, *97*(9), 094423.

[52] O. Kovalenko, T. Pezeril, and V. V. Temnov, New concept for magnetization switching by ultrafast acoustic pulses, *Phys. Rev. Lett.* 110, 266602 (2013).

[53] S. H. Chun, Y. S. Chai, B. Jeon, H. J. Kim, Y. S. Oh, I. Kim, H. Kim, B. J. Jeon, S. Y. Haam, J. Park, S. H. Lee, J. Chung, J. Park, and K. H. Kim, Electric field control of nonvolatile four-state magnetization at room temperature, *Phys. Rev. Lett.* 108, 177201 (2012).

[54] R. O. Cherifi, V. Ivanovskaya, L. C. Phillips, A. Zobelli, I. C. Infante, E. Jacquet, V. Garcia, S. Fusil, P. R. Briddon, N. Guiblin, A. Mougin, A. A. Ünal, F. Kronast, S. Valencia, B. Dkhil, A. Barthélémy, and M. Bibes, Electric-field control of magnetic order above room temperature, *Nat. Mater.* 13, 345–351 (2014).

[55] Z. Li and S. Zhang, Thermally assisted magnetization reversal in the presence of a spin-transfer torque, *Phys. Rev. B* 69, 134416 (2004).

[56] S. Wienholdt, D. Hinzke, K. Carva, P. M. Oppeneer, and U. Nowak, Orbital-resolved spin model for thermal magnetization switching in rare-earth-based ferrimagnets, *Phys. Rev. B* 88, 020406 (2013)

[57] Yu, H., Granville, S., Yu, D. P., & Ansermet, J. P. (2010). Evidence for thermal spin-transfer torque. *Physical review letters*, *104*(14), 146601.

[58] Hatami, M., Bauer, G. E., Zhang, Q., & Kelly, P. J. (2007). Thermal spin-transfer torque in magnetoelectronic devices. *Physical review letters*, *99*(6), 066603.

[59] Bauer, G. E., Saitoh, E., & Van Wees, B. J. (2012). Spin caloritronics. *Nature materials*, *11*(5), 391-399.

[60] Yang, Y. , Wilson, R. B. , Gorchon, J. , Lambert, C. H. , Salahuddin, S. , & Bokor, J. . (2017). Ultrafast magnetization reversal by picosecond electrical pulses. Science Advances, 3(11), e1603117.

[61] Rezende, S. M., Rodríguez-Suárez, R. L., Cunha, R. O., Rodrigues, A. R., Machado, F. L. A., Guerra, G. F., ... & Azevedo, A. (2014). Magnon spin-current theory for the longitudinal spin-Seebeck effect. *Physical Review B*, *89*(1), 014416.

[62] Slonczewski, J. C. (2010). Initiation of spin-transfer torque by thermal transport from magnons. *Physical Review B*, *82*(5), 054403.

[63] S. Mangin, D. Ravelosona, J. A. Katine, E. E. Fullerton, Current-induced magnetization reversal in nanopillars with perpendicular anisotropy, *Nat. Mater.* 5, 210–215 (2006).

[64] M. Wang, W. Cai, K. Cao, J. Zhou, J. Wrona, S. Peng, H. Yang, J. Wei, W. Kang, Y. Zhang, J. Langer, B. Ocker, A. Fert, W Zhao, Current-induced magnetization switching in atom-thick tungsten engineered perpendicular magnetic tunnel junctions with large tunnel magnetoresistance, *Nature Commun*. 9, 671 (2018).

[65] Diao, Z., Li, Z., Wang, S., Ding, Y., Panchula, A., Chen, E., ... & Huai, Y. (2007). Spin-transfer torque switching in magnetic tunnel junctions and spin-transfer torque random access memory. *Journal of Physics: Condensed Matter*, *19*(16), 165209.

[66] Li, Z., & Zhang, S. (2003). Magnetization dynamics with a spin-transfer torque. *Physical Review B*, *68*(2), 024404.

[67] Chen, E., Apalkov, D., Diao, Z., Driskill-Smith, A., Druist, D., Lottis, D., ... & Visscher, P. B. (2010). Advances and future prospects of spin-transfer torque random access memory. *IEEE Transactions on Magnetics*, *46*(6), 1873-1878.

[68] Kishi, T., Yoda, H., Kai, T., Nagase, T., Kitagawa, E., Yoshikawa, M., ... & Ando, K. (2008, December). Lower-current and fast switching of a perpendicular TMR for high speed and high density spin-transfer-torque MRAM. In *2008 IEEE International Electron Devices Meeting* (pp. 1-4). IEEE.

[69] Kent, A. D., Özyilmaz, B., & Del Barco, E. (2004). Spin-transfer-induced precessional magnetization reversal. *Applied Physics Letters*, *84*(19), 3897-3899.

[70] Wang, M., Cai, W., Zhu, D., Wang, Z., Kan, J., Zhao, Z., ... & Zhao, W. (2018). Field-free switching of a perpendicular magnetic tunnel junction through the interplay of spin–orbit and spin-transfer torques. *Nature electronics*, *1*(11), 582-588.

[71] Hao, Q., & Xiao, G. (2015). Giant spin Hall effect and switching induced by spin-transfer torque in a W/Co 40 Fe 40 B 20/MgO structure with perpendicular magnetic anisotropy. *Physical Review Applied*, *3*(3), 034009.

[72] Diao, Z., Panchula, A., Ding, Y., Pakala, M., Wang, S., Li, Z., ... & Huai, Y. (2007). Spin transfer switching in dual MgO magnetic tunnel junctions. *Applied Physics Letters*, *90*(13), 132508.

[73] Huai, Y., Albert, F., Nguyen, P., Pakala, M., & Valet, T. (2004). Observation of spin-transfer switching in deep submicron-sized and low-resistance magnetic tunnel junctions. *Applied Physics Letters*, *84*(16), 3118-3120.

[74] Diao, Z., Apalkov, D., Pakala, M., Ding, Y., Panchula, A., & Huai, Y. (2005). Spin transfer switching and spin polarization in magnetic tunnel junctions with MgO and AlO x barriers. *Applied Physics Letters*, *87*(23), 232502.

[75] Liu, H., Bedau, D., Backes, D., Katine, J. A., Langer, J., & Kent, A. D. (2010). Ultrafast switching in magnetic tunnel junction based orthogonal spin transfer devices. *Applied Physics Letters*, *97*(24), 242510.

[76] Lou, X., Gao, Z., Dimitrov, D. V., & Tang, M. X. (2008). Demonstration of multilevel cell spin transfer switching in MgO magnetic tunnel junctions. *Applied*

Physics Letters, *93*(24), 242502.

[77] Yakata, S., Kubota, H., Suzuki, Y., Yakushiji, K., Fukushima, A., Yuasa, S., & Ando, K. (2009). Influence of perpendicular magnetic anisotropy on spin-transfer switching current in Co Fe B∕ Mg O∕ Co Fe B magnetic tunnel junctions. *Journal of Applied Physics*, *105*(7), 07D131.

[78] Agranat, M.B., S.I. Ashitkov, A.B. Granovskii, and G.I. Rukman, Interaction of picosecond laser pulses with the electron, spin, and phonon subsystems of nickel Sov. Phys. JETP, 1984. 59(4): p. 804-806,

[79] A. Vaterlaus, T. Beutler, and F. Meier, spin-lattice relaxation time of ferromagnetic gadolinium determined with time-resolved spin-polarized photoemission. Phys. Rev. Lett. 67, 3314-3317 (1991).

[80] Beaurepaire, E., Merle, J. C., Daunois, A., & Bigot, J. Y. (1996). Ultrafast spin dynamics in ferromagnetic nickel. Physical review letters, 76(22), 4250.

[81] Xu, Y., Deb, M., Malinowski, G., Hehn, M. & Zhao, W. Ultrafast Magnetization Manipulation Using Single Femtosecond Light and Hot-Electron Pulses. *Adv.Mater.* 29, 1703474 (2017).

[82] Xu, Y. *et al.* From single to multiple pulse all-optical switching in GdFeCo thin films. *Phys. Rev. B* 100, 064424 (2019).

[83] Avilés-Félix, L. *et al.* Single-shot all-optical switching of magnetization in Tb/Co multilayer-based electrodes. *Sci. Rep.* 10, 1–8 (2020).

[84] Banerjee, C. *et al.* Single pulse all-optical toggle switching of magnetization without Gd: The example of Mn2RuxGa. *arXiv*:1909.05809.

[85] Kichin, G. *et al.* From Multiple- to Single-Pulse All-Optical Helicity-Dependent Switching in Ferromagnetic Co / Pt Multilayers. *Phys. Rev. Appl.* 12, 024019 (2019).

[86] Lambert, C.-H. et al. All-optical control of ferromagnetic thin films and nanostructures. Science 345, 1337 (Sept. 2014).

[87] Medapalli, R. *et al.* Multiscale dynamics of helicity-dependent all-optical

magnetization reversal in ferromagnetic Co / Pt multilayers. *Phys. Rev. B* 96, 22421 (2017).

[88] M. S. El Hadri, M. Hehn, G. Malinowski, and S. M. Materials and devices for all-optical helicity-dependent switching. *J. Phys. D Appl. Phys.* 50, 133002 (2017).

[89] Quessab, Y. (2018). *Mechanism and size effects of helicity-dependent all-optical magnetization switching in ferromagnetic thin films* (Doctoral dissertation, Université de Lorraine).

[90] Dill, F. H., Hornberger, W. P., Hauge, P. S., & Shaw, J. M. (1975). Characterization of positive photoresist. *IEEE Transactions on electron devices*, *22*(7), 445-452.

[91] Lee, L. L., Schaper, C. D., & Ho, W. K. (2002). Real-time predictive control of photoresist film thickness uniformity. *IEEE Transactions on Semiconductor Manufacturing*, *15*(1), 51-59.

[92] Widmann, D. W., & Binder, H. A. N. S. (1975). Linewidth variations in photoresist patterns on profiled surfaces. *IEEE Transactions on Electron Devices*, *22*(7), 467-471.

[93] Pham, N. P., Burghartz, J. N., & Sarro, P. M. (2005). Spray coating of photoresist for pattern transfer on high topography surfaces. *Journal of Micromechanics and Microengineering*, *15*(4), 691.

[94] Lee, H. S., & Yoon, J. B. (2005). A simple and effective lift-off with positive photoresist. *Journal of Micromechanics and Microengineering*, *15*(11), 2136.

[95] Flack, W. W., Fan, W. P., & White, S. (1998, June). Optimization and characterization of ultrathick photoresist films. In *Advances in Resist Technology and Processing XV* (Vol. 3333, pp. 1288-1303). International Society for Optics and Photonics.

[96] Brunet, M., O'Donnell, T., O'Brien, J., McCloskey, P., & Mathuna, S. C. O.

(2002). Thick photoresist development for the fabrication of high aspect ratio magnetic coils. *Journal of Micromechanics and Microengineering*, *12*(4), 444.

[97] Palmer, E., Pen, W., & Spanos, C. J. (1996). Control of photoresist properties: A Kalman filter based approach. *IEEE Transactions on Semiconductor Manufacturing*, *9*(2), 208-214.

[98] Dentinger, P. M., Cardinale, G. F., Henderson, C. C., Fisher, A., & Ray-Chaudhuri, A. K. (2000, July). Photoresist film thickness for extreme ultraviolet lithography. In *Emerging Lithographic Technologies IV* (Vol. 3997, pp. 588-599). International Society for Optics and Photonics.

[99] Garza, M. (1994). *U.S. Patent No. 5,330,883*. Washington, DC: U.S. Patent and Trademark Office.

[100] Kim, J. Y., Bak, H., Sohn, Y. S., An, I., Bang, K. Y., Oh, H. K., & Han, W. S. (2001, September). Photoresist thickness variation due to local and global topography. In *Optical Microlithography XIV* (Vol. 4346, pp. 982-993). International Society for Optics and Photonics.

[101] Dill, F. H. (1975). Optical lithography. *IEEE transactions on electron devices*, *22*(7), 440-444.

[102] Shaw, J. M., Gelorme, J. D., LaBianca, N. C., Conley, W. E., & Holmes, S. J. (1997). Negative photoresists for optical lithography. *IBM journal of Research and Development*, *41*(1.2), 81-94.

[103] Hirai, Y., Inamoto, Y., Sugano, K., Tsuchiya, T., & Tabata, O. (2006). Moving mask UV lithography for three-dimensional structuring. *Journal of Micromechanics and Microengineering*, *17*(2), 199.

[104] Anderson, E. H., Horwitz, C. M., & Smith, H. I. (1983). Holographic lithography with thick photoresist. *Applied Physics Letters*, *43*(9), 874-875.

[105] French, R. H., & Tran, H. V. (2009). Immersion lithography: photomask and

wafer-level materials. *Annual Review of Materials Research*, *39*.

[106] Mojarad, N., Gobrecht, J., & Ekinci, Y. (2015). Beyond EUV lithography: a comparative study of efficient photoresists' performance. *Scientific reports*, *5*(1), 1-7.

[107] http://henderson.chbe.gatech.edu/

[108] https://plasma.oxinst.com/campaigns/technology/ion-beam-etching/

[109] Wei, J., Cao, K., Cui, H., Shi, K., Cai, W., Li, H., ... & Zhao, W. (2019, September). All Perpendicular Spin Nano-Oscillators with Composite Free Layer. In *Spin* (Vol. 9, No. 03, p. 1940010). World Scientific Publishing Company.

[110] Kirilyuk A, Kimel A V, Rasing T. Ultrafast optical manipulation of magnetic order. Reviews of Modern Physics, 82(3): 2731 (2010)

[111] Evans R F L, Fan W J, Chureemart P, et al. Atomistic spin model simulations of magnetic nanomaterials. Journal of Physics: Condensed Matter, 26(10): 103202 (2014)

[112] Dobin, A. Y., & Victora, R. H. Surface roughness induced extrinsic damping in thin magnetic films. *Physical review letters*, *92*(25), 257204 (2004)

[113] Ellis, M. O. A., Ostler, T. A., & Chantrell, R. W. Classical spin model of the relaxation dynamics of rare-earth doped permalloy. *Physical Review B*, *86*(17), 174418 (2012)

[114] Garanin, D. A. (1997). Fokker-Planck and Landau-Lifshitz-Bloch equations for classical ferromagnets. *Physical Review B*, *55*(5), 3050.

[115] Anisimov, S. I., Kapeliovich, B. L., & Perelman, T. L. (1974). Electron emission from metal surfaces exposed to ultrashort laser pulses. Zh. Eksp. Teor. Fiz, 66(2), 375-377.

[116] Pufall, M. R., Rippard, W. H., Kaka, S., Silva, T. J. & Russek, S. E. Frequency modulation of spin-transfer oscillators. *Appl. Phys. Lett.* 86, 082506 (2005).

[117] Zeng, Z. M. *et al.* Enhancement of microwave emission in magnetic tunnel junction oscillators through in-plane field orientation. *Appl. Phys. Lett.* 99, 032503 (2011).

[118] Carpentieri, M. & Finocchio, G. *Spintronic Oscillators Based on Spin-Transfer Torque and Spin-Orbit Torque. Handbook of Surface Science* 5, (Elsevier B.V., 2016).

[119] Zeng, Z., Finocchio, G. & Jiang, H. Spin transfer nano-oscillators. *Nanoscale* 5, 2219 (2013).

[120] Chen, T. *et al.* Spin-Torque and Spin-Hall Nano-Oscillators. *Proc. IEEE* 104, 1919–1945 (2016).

[121] Silva, T. J. & Rippard, W. H. Developments in nano-oscillators based upon spin-transfer point-contact devices. *J. Magn. Magn. Mater.* 320, 1260–1271 (2008).

[122] Slavin, A. & Tiberkevich, V. Auto-Oscillator Theory of Microwave Generation by Spin-Polarized Current. *IEEE Trans. Magn.* 45, 1875–1918 (2009).

[123] Zeng, Z. *et al.* Ultralow-current-density and bias-field-free spin-transfer nano-oscillator. *Sci. Rep.* 3, 01426 (2013).

[124] Wei, J., Fang, B., Wu, W., Cao, K., Chen, H. H., Zhang, Y., ... & Zhao, W. Amplitude and frequency modulation based on memristor-controlled spin nano-oscillators. *Nanotechnology*, *31*(4), 045202 (2019)

[125] Suh, Y. H., & Chang, K. A wideband coplanar stripline to microstrip transition. *IEEE Microwave and wireless components letters*, *11*(1), 28-29 (2001)

[126] Tu, W. H., & Chang, K.. Wide-band microstrip-to-coplanar stripline/slotline transitions. *IEEE Transactions on Microwave Theory and Techniques*, *54*(3), 1084-1089 (2006)

[127] Jokela, K. T. Narrow-band stripline or microstrip filters with transmission zeros at real and imaginary frequencies. *IEEE Transactions on Microwave Theory and Techniques*, *28*(6), 542-547 (1980)

[128] Nghiem, D., Williams, J. T., & Jackson, D. R. A general analysis of propagation along multiple-layer superconducting stripline and microstrip transmission lines. *IEEE transactions on microwave theory and techniques*, *39*(9), 1553-1565 (1991)

[129] Greiser, J. W. Coplanar stripline antenna. *Microwave Journal*, *19*, 47-49 (1976)

[130] Maloratsky, L. G., & Lines, M. Reviewing the basics of microstrip. *Microwaves RF*, *39*(March), 79-88 (2000)

[131] Pues, H. F., & Van De Capelle, A. R An impedance-matching technique for increasing the bandwidth of microstrip antennas. *IEEE transactions on antennas and propagation*, *37*(11), 1345-1354 (1989).

[132] March, S. L. (1982, June). Phase velocity compensation in parallel-coupled microstrip. In *1982 IEEE MTT-S International Microwave Symposium Digest* (pp. 410-412). IEEE.

[133] Huang X, Wu H, Sekar D C, Nguyen S N, Wang K and Qian H 2015 Optimization of TiN/TaOx/HfO2/TiN RRAM arrays for improved switching and data retention. In 2015 IEEE

[134] Wang, L., Yang, C., Wen, J., Gai, S., & Peng, Y. Overview of emerging memristor families from resistive memristor to spintronic memristor. *Journal of Materials Science: Materials in Electronics*, *26*(7), 4618-4628 (2015)

[135] Ielmini, D., & Wong, H. S. P. In-memory computing with resistive switching devices. *Nature Electronics*, *1*(6), 333-343 (2018)

[136] Vieira, M.A.M., Coelho, C.N., Da Silva, D.C. and da Mata, J.M., 2003, September. Survey on wireless sensor network devices. In EFTA 2003. *2003*

IEEE Conference on Emerging Technologies and Factory Automation. Proceedings (Cat. No. 03TH8696) (Vol. 1, pp. 537-544). IEEE.

[137] Pedram, Massoud,Rabaey, Jan M. Power Aware Design Methododgies, Springer,2002

[138] A. Purbawati, F. Garcia-Sanchez, L.D. Buda-Prejbeanu, U. Ebels, *Enhanced modulation rates via field modulation in spin torque nano-oscillators*, Appl. Phys. Lett. 108, 122402 (2016)

[139] A. Ruiz-Calaforra, A. Purbawati, T. Brächer, J. Hem, C. Murapaka*,* E. Jiménez*,* D. Mauri*,* A.Zeltser*,* J. A. Katine*,*M.-C. Cyrille*,* L. D. Buda-Prejbeanu*, and* U. Ebels, *Frequency shift keying by current modulation in a MTJ-based STNO with high data rate,* Appl. Phys.Lett. 111, 082401 (2017)

[140] Ma, R., Purbawati, A., Kreißig, M., Protze, F., Ruiz-Calaforra, A., Hem, J., ... & Ellinger, F. (2017, June). Spin torque oscillator based BFSK modulation. In *2017 13th Conference on Ph. D. Research in Microelectronics and Electronics (PRIME)* (pp. 1-4). IEEE.

[141] Choi, H. S., Kang, S. Y., Cho, S. J., Oh, I. Y., Shin, M., Park, H., ... & Park, C. S. Spin nano–oscillator–based wireless communication. Scientific reports, 4(1), 1-7. (2014)

[142] Hallstein, S., Berger, J. D., Hilpert, M., Schneider, H. C., Rühle, W. W., Jahnke, F., ... & Oestreich, M.. Manifestation of coherent spin precession in stimulated semiconductor emission dynamics. *Physical Review B*, *56*(12), R7076. (1997)

[143] Lv, G., Zhang, H., Cao, X., Liu, Y., Hou, Z., Qin, Y., ... & Wang, L. Modeling of magnetization precession in spin-torque nano-oscillators with a tilted polarizer. *AIP Advances*, *5*(7), 077171. (2015).

[144] Prokopenko, O., Bankowski, E., Meitzler, T., Tiberkevich, V., & Slavin, A.. Spin-torque nano-oscillator as a microwave signal source. *IEEE Magnetics Letters*, *2*, 3000104-3000104. (2011)

[145] Kowalska, E., Sluka, V., Fowley, C., Kakay, A., Aleksandrov, Y., Lindner, J., ... & Deac, A. (2015, May). Spin-transfer effects in MgO-based tunnel junctions with an out-of-plane free layer and an in-plane polarizer: Static states and steady-state precession. In *2015 IEEE International Magnetics Conference (INTERMAG)* (pp. 1-1). IEEE.

[146] Demidov, V. E., Urazhdin, S., Zholud, A., Sadovnikov, A. V., Slavin, A. N., & Demokritov, S. O. (2015). Spin-current nano-oscillator based on nonlocal spin injection. *Scientific reports*, *5*(1), 1-5.

[147] Duan, Z., Smith, A., Yang, L., Youngblood, B., Lindner, J., Demidov, V. E., ... & Krivorotov, I. N. (2014). Nanowire spin torque oscillator driven by spin orbit torques. *Nature communications*, *5*(1), 1-7.

[148] Bonetti, S., Muduli, P., Mancoff, F., & Åkerman, J. (2009). Spin torque oscillator frequency versus magnetic field angle: The prospect of operation beyond 65 GHz. *Applied Physics Letters*, *94*(10), 102507.

[149] Tarequzzaman, M., Böhnert, T., Decker, M., Costa, J. D., Borme, J., Lacoste, B., ... & Freitas, P. P. (2019). Spin torque nano-oscillator driven by combined spin injection from tunneling and spin Hall current. *Communications Physics*, *2*(1), 1-8.

[150] C. Zhang, B. Fang, B. Wang, and Z. Zeng, *J. Magn. Magn. Mater*. 452, 188 (2018)

[151] Keller, M. W., Kos, A. B., Silva, T. J., Rippard, W. H., & Pufall, M. R. (2009). Time domain measurement of phase noise in a spin torque oscillator. *Applied Physics Letters*, *94*(19), 193105.

[152] Zhou, Y., Zha, C. L., Bonetti, S., Persson, J., & Åkerman, J. (2008). Spin-torque oscillator with tilted fixed layer magnetization. *Applied Physics Letters*, *92*(26), 262508.

[153] Muduli, P. K., Pogoryelov, Y., Bonetti, S., Consolo, G., Mancoff, F., & Åkerman,

J. (2010). Nonlinear frequency and amplitude modulation of a nanocontact-based spin-torque oscillator. *Physical Review B*, *81*(14), 140408.

[154] Tiberkevich, V., Slavin, A., & Kim, J. V. (2007). Microwave power generated by a spin-torque oscillator in the presence of noise. *Applied Physics Letters*, *91*(19), 192506.

[155] Boone, C., Katine, J. A., Childress, J. R., Zhu, J., Cheng, X., & Krivorotov, I. N. (2009). Experimental test of an analytical theory of spin-torque-oscillator dynamics. *Physical Review B*, *79*(14), 140404.

[156] Zhou, Y., Persson, J., Bonetti, S., & Åkerman, J. (2008). Tunable intrinsic phase of a spin torque oscillator. *Applied Physics Letters*, *92*(9), 092505.

[157] Pogoryelov, Y., Muduli, P. K., Bonetti, S., Iacocca, E., Mancoff, F., & Åkerman, J. (2011). Frequency modulation of spin torque oscillator pairs. *Applied Physics Letters*, *98*(19), 192501.

[158] Taniguchi, T., Arai, H., Tsunegi, S., Tamaru, S., Kubota, H., & Imamura, H. (2013). Critical field of spin torque oscillator with perpendicularly magnetized free layer. *Applied Physics Express*, *6*(12), 123003.

[159] Kubota, H., Yakushiji, K., Fukushima, A., Tamaru, S., Konoto, M., Nozaki, T., ... & Imamura, H. (2013). Spin-torque oscillator based on magnetic tunnel junction with a perpendicularly magnetized free layer and in-plane magnetized polarizer. *Applied Physics Express*, *6*(10), 103003.

[160] Rowlands, G. E., & Krivorotov, I. N. (2012). Magnetization dynamics in a dual free-layer spin-torque nano-oscillator. *Physical Review B*, *86*(9), 094425.

[161] Muduli, P. K., Heinonen, O. G., & Åkerman, J. (2012). Decoherence and mode hopping in a magnetic tunnel junction based spin torque oscillator. *Physical review letters*, *108*(20), 207203.

[162] Gerhart, G., Bankowski, E., Melkov, G. A., Tiberkevich, V. S., & Slavin, A. N.

(2007). Angular dependence of the microwave-generation threshold in a nanoscale spin-torque oscillator. *Physical Review B*, *76*(2), 024437.

[163] Tsunegi, S., Kubota, H., Yakushiji, K., Konoto, M., Tamaru, S., Fukushima, A., ... & Yuasa, S. (2014). High emission power and Q factor in spin torque vortex oscillator consisting of FeB free layer. *Applied Physics Express*, *7*(6), 063009.

[164] Pogoryelov, Y., Muduli, P. K., Bonetti, S., Mancoff, F., & Åkerman, J. (2011). Spin-torque oscillator linewidth narrowing under current modulation. *Applied Physics Letters*, *98*(19), 192506.

[165] Tsunegi, S., Yakushiji, K., Fukushima, A., Yuasa, S., & Kubota, H. (2016). Microwave emission power exceeding 10 μ W in spin torque vortex oscillator. *Applied Physics Letters*, *109*(25), 252402.

[166] Haidar, M., Awad, A. A., Dvornik, M., Khymyn, R., Houshang, A., & Åkerman, J. (2019). A single layer spin-orbit torque nano-oscillator. *Nature communications*, *10*(1), 1-6.

[167] Sani, S. R., Dürrenfeld, P., Mohseni, S. M., Chung, S., & Åkerman, J. (2013). Microwave signal generation in single-layer nano-contact spin torque oscillators. *IEEE transactions on magnetics*, *49*(7), 4331-4334.

[168] Dumas, R. K., J. (2014) Recent advances in nanocontact spin-torque oscillators. *IEEE transactions on magnetics*, *50*(6), 1-7.

[169] Davies, C. S. *et al.* Pathways for Single-Shot All-Optical Switching of Magnetization in Ferrimagnets. *Phys. Rev. Appl.* 13, 024064 (2020).

[170] J. M. Liu, Simple technique for measurements of pulsed Gaussian-beam spot sizes, *Opt. Lett.* **7**, 196 (1982).

[171] J. Barker, U. Atxitia, T. A. Ostler, O. Hovorka, O. Chubykalo-Fesenko and R. W. Chantrell, Two-magnon bound state causes ultrafast thermally induced magnetisation switching, *Sci. Rep.* **3**, 03262 (2013).

[172] T. A. Ostler, R. F. L. Evans, R. W. Chantrell, U. Atxitia, O. Chubykalo-Fesenko, I. Radu, R. Abrudan, F. Radu, A. Tsukamoto, A. Itoh, A. Kirilyuk, Th. Rasing and A. Kimel, Crystallographically amorphous ferrimagnetic alloys: Comparing a localized atomistic spin model with experiments, *Phys. Rev. B* 84, 024407 (2011).

[173] Moreno, R., Ostler, T. A., Chantrell, R. W., & Chubykalo-Fesenko, O. (2017). Conditions for thermally induced all-optical switching in ferrimagnetic alloys: Modeling of TbCo. *Physical Review B*, *96*(1), 014409.

[174] C. D. Stanciu, A. Tsukamoto, A. V. Kimel, F. Hansteen, A. Kirilyuk, A. Itoh, and Th. Rasing, Subpicosecond magnetization reversal across ferrimagnetic compensation points, *Phys. Rev. Lett.* **99**, 047601 (2007).

[175] A. Hassdenteufel, J. Schmidt, C. Schubert, B. Hebler, M. Helm, M. Albrecht, and R. Bratschitsch, Low-remanence criterion for helicity-dependent all-optical magnetic switching in ferrimagnets, *Physical Review B* 91, 104431 (2015).

[176] U. Atxitia, T. A. Ostler, R. W. Chantrell, and O. Chubykalo-Fesenko, Optimal electron, phonon, and magnetic characteristics for low energy thermally induced magnetization switching, *Appl. Phys. Lett.* 107, 192402 (2015).

[177] Y. Xu, M. Hehn, W. Zhao, X. Lin, G. Malinowski, and S. Mangin, From single to multiple pulse all-optical switching in GdFeCo thin films, *Phys. Rev. B* 100, 0644024 (2019).

[178] Satoshi, Iihama, Yong, Xu, Marwan, & Deb, et al. (2018). Single-shot multi-level all-optical magnetization switching mediated by spin transport. *Adv. Mater.* 30, 1804004 (2020).

[179] Remy, Q., Igarashi, J., Iihama, S., Malinowski, G., Hehn, M., Gorchon, J., ... & Mangin, S. (2020). Energy Efficient Control of Ultrafast Spin Current to Induce Single Femtosecond Pulse Switching of a Ferromagnet. Advanced Science, 7, 2001996 (2020).

[180] Igarashi, J., Remy, Q., Iihama, S., Malinowski, G., Hehn, M., Gorchon, J., ... & Mangin, S. Engineering Single-Shot All-Optical Switching of Ferromagnetic Materials. Nano Letters, 20, 12 (2020).

LIST OF ABBREVATIONS

GMR	giant magnetoresistance
IBE	ion beam etching
3TM	magnetic three-temperature model
MCD	magnetic circular dichroism
MOKE	magneto-optic Kerr effect
MRAM	magnetic random-access memory
MTJ	magnetic tunneling junction
PMA	perpendicular magnetic anisotropy
PVD	physical vapor deposition
CVD	chemical vapor deposition
RF	radio frequency
TMR	tunnel magnetoresistance
UV	ultraviolet
ICP	Inductive coupling plasma
IFE	inverse faraday effect
FWHM	full width at half maximum
AMR	anisotropy magnetoresistance
LLG	Landau-Lifshitz-Gilbert
AO-HIS	all-optical helicity-independent switching
AO-HDS	all-optical helicity-dependent switching
FSK	frequency shift keying
ASK	amplitude shift keying
STNO	spin transfer torque nano-oscillator
CPP	current perpendicular to plane
CIP	current in plane
fs	femtosecond
RKKY	Ruderman–Kittel–Kasuya–Yosida

DC	direct current
AHE	anomalous Hall effect

LIST OF PUBLICATIONS

[1] **Wei J**, Chang L, Wang Z, et al. Ultrafast spintronic integrated circuits, 2017, IEEE ASICON.

[2] **Wei J**, Cao K, Cui H, et al. All Perpendicular Spin Nano-Oscillators with Composite Free Layer, Spin, 9(03): 1940010 (2019)

[3] **Wei J**, Fang B, Wu W, et al. Amplitude and frequency modulation based on memristor-controlled spin nano-oscillators, Nanotechnology, 31(4): 045202 (2019)

[4] **Wei J**, Zhang B, M. Hehn, et al. All-optical helicity-independent switching state diagram in GdFeCo, Phy. Rev. Applied (Accepted)

[5] Cabero Zabalaga M A, **Wei J**, Yang H, et al. Unraveling the characterristic shape for magnetic field effects in polymer–fullerene solar cells, ACS Omega, 2(11): 7777-7783 (2017)

In preparation

[1] **Wei J** et al. Different types of optical response of Co/Pt multilayers.

Poster

All Perpendicular Spin Nano-Oscillators with Composite Free Layer, IEEE Magnetic Society Summer School, Richmond, America, June 1-6, 2019.